7. 051

PN-ABD-198

Asian Institute of Technology
Bangkok Thailand

WELDED WIRE WALL AND EMBANKMENT SYSTEM WITH COHESIVE BACKFILL ON SOFT CLAY

Third Progress Report for the
Period Ending June 30, 1989

Submitted to: U.S. Agency for International Development
Science and Technology Division
Office of Technical Resources
USAID Thailand, 37 Soi Somprasong
Petchburi Road, Bangkok

Submitted by

Dr. Dennes T. Bergado, Principal Investigator
Mr. Casan L. Sampaco, Research Associate
Mr. Marolo C. Alfaro, Research Associate
Mr. R. Sivashankar, Doctoral Student
and
Prof. A.S. Balasubramaniam, Co-Principal Investigator

Division of Geotechnical and Transportation Engineering
Asian Institute of Technology
G.P.O. Box 2754,
Bangkok, Thailand

July, 1989

WELDED WIRE WALL AND EMBANKMENT SYSTEM WITH COHESIVE BACKFILL ON SOFT CLAY

Third Progress Report for the

Period Ending June 30, 1989

Submitted by

Dr. Dennes T. Bergado, Principal Investigator

Mr. Casan L. Sampaco, Research Associate

Mr. Marolo C. Alfaro, Research Associate

Mr. R. Sivashankar, Doctoral Student

and

Prof. A. S. Balasubramaniam, Co-Principal Investigator

Division of Geotechnical and Transportation Engineering

Asian Institute of Technology

G.P.O. Box 2754

Bangkok, Thailand

July, 1989

TABLE OF CONTENTS

		Page No.
	SUMMARY	1
I.	RESEARCH PERSONNEL	3
II.	RESEARCH COLLABORATION	3
III.	PUBLICATIONS	4
IV.	PLANS FOR THE NEXT REPORTING PERIOD	4
V.	ADDITIONAL EQUIPMENTS ACQUIRED BY THE PROJECT	5
VI.	TENSILE STRENGTH TESTS OF STEEL REINFORCEMENTS	9
VII.	LABORATORY TESTS ON BACKFILL MATERIALS	9
VIII.	FIELD TESTS AT THE WELDED WIRE WALL EXPERIMENTAL SITE	10
IX.	LABORATORY PULLOUT TESTS	12
	Theoretical Background	12
	Fundamentals of Strain Determination Using Strain Gages	19
	Basic Principles of LVDT	23
	Methodology	24
X.	DISCUSSION AND PRELIMINARY ANALYSIS	26
	Weathered Clay Backfill	26
	Lateritic Residual Soil	28
XI.	ANALYSIS AND DESIGN CONSIDERATION OF WELDED WIRE WALLS	32
XII.	CONSTRUCTION PROCEDURE, INSTRUMENTATION, AND MONITORING PROGRAMS FOR THE WELDED WIRE EXPERIMENTAL WALL	34
	Construction Procedure	34
	Purpose of Instrumenting the Wall	35
	Scope of the Instrumentation Program	36
	Description of the Instrumentation Program	36
XIII.	REFERENCES	44
	TABLES	47
	FIGURES	51

WELDED WIRE WALL AND EMBANKMENT SYSTEM WITH COHESIVE BACKFILL ON SOFT CLAY

SUMMARY

Much work has been accomplished for the past six months since the last report and the detailed description of the results are presented herein. Outlined in this progress report are the pullout testing made in the laboratory, with typical results presented and analyzed, and the programs done in the field where actual construction, instrumentation and monitoring procedures of the welded wire wall are described in full detail. The report still retains, as usual, the fundamental manner of presenting minor details such as the additional equipments acquired by the project, research collaboration, project personnel, and future plans.

Pullout tests on welded wire grid reinforcements of varying bar diameter and aperture sizes, were conducted at the pullout testing laboratory of the Asian Institute of Technology (AIT) using the reddish-brown weathered Bangkok clay and clayey-gravelly, lateritic residual soil as backfill materials. A total of eighty-seven pullout tests were carried out using weathered clay backfill compacted at 95% standard Proctor density and at 2 different compaction moisture contents (dry and wet sides of optimum). The tests were conducted with normal pressures ranging from 1 to 13 tsm. The reinforcing mats consisted of 1/4" and 3/8" diameter steel bars welded together to form a 6" x 9", 6" x 12", and 6" x 18" aperture sizes. Likewise, forty seven pullout tests were conducted using lateritic residual soil at 3 different moisture contents (dry, optimum, and wet) with varying compaction densities of 95% and 100%. The tests were conducted at lower pressures ranging from 0.2 to 1.8 tsm. The reinforcing mats used were 1/4" and 1/2" diameter bars in a 6"x6" and 6"x9" grid sizes. In all tests conducted, the soil-reinforcement interaction shows the dominant role of the passive resistance contributed by the transverse members to the total pullout resistance. The friction resistance of the longitudinal members was found to range from 3 to 5% of the total pullout resistance of the mat. Furthermore, the yield strengths of the reinforcement occurred at low strains in the order of 1 to 4 mm of displacement only due to the inextensible nature of steel. It was also found that the smaller diameter bars were effective in enhancing the full mobilization of passive resistance by yielding higher pullout capacities. The 6"x9" mesh geometry seems to be the most efficient of all the grid sizes that were used.

Last April, 1989, the 5.5 m high, welded wire wall/embankment system utilizing poor quality backfills, was constructed in the area north of ET Building inside the AIT campus. The construction of the wall lasted for about a month. It consists of 3 different sections along its length, with a reinforced vertical front face and an unreinforced back slope of 1 horizontal to 1 vertical. The reinforcement consists of 8' wide by 18'9" long welded wire mats made up of W4.5 x W3.5 diameter galvanized steel bars forming a 6" x 9" grid. Section I was constructed using silty, clayey sand backfill from Ayutthaya. The middle section was constructed using the clayey, gravelly lateritic residual soil from Saraburi while the third section was constructed using the locally available weathered Bangkok clay which was excavated from the top 2 m of the subsoil. The wall was provided with an extensive instrumentation and monitoring program which covers tension measurement in the reinforcing mats both during and after construction, settlement monitoring of the soft clay foundation, lateral movement monitoring of the wall and its foundation, evaluation of the total base pressure of the wall, and measurements of the excess pore pressures generated in the soft clay. The settlements measured at several sections of the wall reached up to 60 cm after 2 months. Due to the flexibility of the soft clay foundation, the total measured base pressure establishes no definite pattern as it continues to readjust itself to the applied load. This causes the maximum tension line in the reinforcing wires to shift with time. Preliminary analyses of the tension distribution back from the face of the wall during the construction stage, indicated that the location of the maximum tension line occurs at a distance within 2 to 6 ft from the face of the wall. The measured value of the lateral earth pressure coefficient (K) during construction, ranged from the active value to the at-rest (K_o) value throughout the wall height. The maximum lateral movement measured by inclinometers amounted to 12 cm at the top of the wall in the vertical face and about 11 cm at 3 m depth in the soft clay subsoil.

I. RESEARCH PERSONNEL

At the end of April, 1989, two master's students who were working on the USAID Project have finished their thesis work and have graduated from AIT. Presently, the USAID project have 3 semi-permanent staff consisting of 2 Research Associates and 1 Research Assistant. One doctoral student is also working on his dissertation about the project. In addition, 2 temporary workers are retained for physical assistance in the laboratory pullout test and in the field monitoring. For the next academic year, it is planned to increase the number of doctoral students to two. Also, a new group of two master's students will be working on the project. At present, the entire project staff are monitoring the behavior of the test embankment and its foundation. Modification of the pullout test machine to incorporate the new load cell is also presently being worked out. The doctoral student will soon start his pullout test program using clayey sand backfill.

II. RESEARCH COLLABORATION

Last April 21, 1989, Prof. Loren R. Anderson together with Mr. Rene Winward came to Bangkok from Utah State University, Logan, Utah, U.S.A. in connection with the USAID welded wire wall research collaboration. They went back to Logan on May 2, 1989. The main purpose of their trip was to assist in the initial construction of the test embankment, especially in the layout of the steel geogrid reinforcement. The other important task was in terms of providing training to the research team in the attachment of strain gages to the reinforcements and in the installation of electrical wires for automatic data acquisition in the field. Their assistance was very valuable to the research team especially at the initial stage of embankment construction. The embankment was constructed for one month from April 24, 1989 to May 24, 1989.

Prof. Anderson also was the invited speaker together with Dr. Bergado during the seminar on earth reinforcement at Chulalongkorn University that was held last April 25, 1989. The seminar was sponsored by the Engineering Institute of Thailand. Dr. Pichai of USAID Thailand attended the one-day seminar. In the afternoon, the participants were invited to witness the pullout test and the embankment construction in the campus of the Asian Institute of Technology.

Prof. Anderson and Dr. Bergado also made a presentation last April 26, 1989 to the Director General of Highway Department and their Senior Staff regarding the use of steel geogrids earth reinforcements on highway infrastructures.

III. PUBLICATIONS

The following publications on the results and analyses of this research project has been made:

(a) Amin, N.U. (1989). "Direct Shear and Pullout Tests on Lateritic Soil at Low Pressures," M. Eng. Thesis No. GT-88-4, AIT, Bangkok, Thailand.

(b) Cisneros, C.B. (1989). "Pullout Resistance of Steel Grids with Weathered Clay as Backfill Materials," M. Eng. Thesis No. GT-88-7, AIT, Bangkok, Thailand.

(c) Bergado, D.T., Cisneros, C.B., Sivashankar, R., Sampaco, C.L. and Alfaro, M.C. (1989). "Pullout Resistance of Steel Grids with Weathered Clay Backfill," Proc. Symp. on Application of Geosynthetic and Geofibre in Southeast Asia, 1-2 August 1989, Kuala Lumpur, Malaysia.

IV. PLANS FOR THE NEXT REPORTING PERIOD

For the next succeeding months, laboratory pullout tests on clayey sand backfill will be carried out using different backfill conditions and varying reinforcing mat geometry. Pullout tests on lateritic residual soil will also be conducted for higher normal pressures while additional effects of different backfill conditions and other mesh sizes will be investigated using weathered clay backfill. It is also planned to carry out numerical modelling of the soil-reinforcement interaction for comparison to the laboratory and field pullout test results.

Field pullout tests will soon be conducted at different periods of time to compare the actual field behaviour with that obtained in the laboratory. The monitoring program for the welded wire wall will still be continued as the settlement goes on, and will be done periodically twice a week. Detailed analysis of the wall performance during and after construction will be presented in the next progress report. Likewise, all the possible data gathered in the laboratory will be investigated and used efficiently for more detailed analysis and interpretation.

V. ADDITIONAL EQUIPMENTS ACQUIRED BY THE PROJECT

This section presents the equipments acquired by the project that were not included in the second progress report.

(1) Electric Control Components

The electric control components are used to build electro-hydraulic control systems. It consist of a power supply and an amplifier module, providing a convenient and economical means of supplying the proper input to various servo valves, control pumps, pressure control valves, and flow control valves. In addition, the electronic control components may be interfaced with a variety of input signal sources such as potentiometers, transducers, programmable controllers, and computers.

(a) Power Supply (Model EMRS-A-11)

The power supply provides the means for mounting one module, supplying it with the proper excitation voltages, and connecting it to external circuit components through a terminal strip. In addition, a highly regulated 12-Volt power supply circuit is included for excitation of command and feedback circuit components. Typical circuit diagram and plan section of the unit is shown in Fig. 1.

(b) Amplifier Module (Model EM-D-20)

The amplifier module is designed to control servo valves, electrohydraulic control pumps, pressure control valves in closed loop pressure control circuits, and flow control valves in closed loop flow or speed control circuits. It consists of a power output stage and a general purpose voltage amplifier. The voltage amplifier may be used independently or in conjunction with the power output stage. Adjustments of current limiters and bias in the output stage permits the unit to drive single polarity servo valves, bipolar servo valves and other electrically modulated values.

The voltage amplifier stage may be set up as either a linear or an integrating amplifier, depending on the setting of internal switches. Other switches allow selection of a low or high gain range and selection of input error limiting for velocity systems. Figure 2 shows the EM-D-20 amplifier module with its block diagram and potentiometer adjustments.

(2) Hydraulic Flushing Valve (Model SM4FV)

Flushing valve allows simulation of the servo valve by rotation of the flushing valve handle. This causes the linear actuator to stroke back and forth or the motor to operate clockwise and counterclockwise. This action loosens built-in system contaminants such as weld scale that otherwise could remain in place until the system was operated. The amount of contaminant removed during flushing depends on the velocity of the fluid. Unless high velocities are attained, much of the contaminant wil not be dislodged until the system is in operation, with component failure the almost certain result.

(3) Electro-Hydraulic Servo Valve (Model SM4-20/Flapper Nozzle Piloted)

The flapper nozzle piloted servo valve provides the flow modulation, reversibility and fast response required in high performance, closed loop control systems. It is ideally suited for applications needing precise control of position, velocity, acceleration, or force. The details of the valve are shown in Fig. 3 together with the typical flow/current relationship.

(4) Power Package (Model T20 with Piston Pumps)

The integral power packages include motor, pump, valving, reservoir and oil filter. These units are self-contained power sources for use as main hydraulic systems or for other auxiliary applications.

(a) Variable Displacement In-line Type Piston Pump (Model PVB5/6)

This model is of the axial piston, variable displacement, inline design. Displacement is varied by means of either a pressure compensation, handwheel, or level control, thus, allowing the machine operator to easily and smoothly control operations under load by varying the pump's oil flow.

(b) Dual Voltage Lincoln Motor (Model 230/460)

This dual voltage Lincoln motor is suitable for 208 Volt operation on the low voltage connection up to the maximum current rating at 208 Volts. It is of aluminum frame type with a capacity of 7.5 HP.

(c) Hydraulic Oil Tank (Model T20VB5C)

(d) Return Line Filter (Model OFRS-15)

Return line filters are designed for use in the return lines of hydraulic systems to remove particulate contaminants from the fluid, thus improving performance and reliability of the system components while extending their service life. It has an integral by-pass valve option which prevents excessive pressure drop, and prevents the element from collapsing and releasing retained contaminants back into the hydraulic system. The valve starts to open when pressure drop across the element exceeds value setting due to flow surges, high viscosity oil, a clogged element, or a combination of these.

(e) High Pressure Filter (Model NF30 (20 GPM/3000psi))

High pressure filter is usually used to provide the lowest system contamination levels and provide clean fluid for sensitive pressure line components and servo-stroke control mechanism. Thus, in this multiple filtration system, the high pressure filter provides the overall system dirt level control and removes much of the dirt generated by the motor before it gets to other systems while the return line filter prevents excessive pressure drop and prevents releasing retained contaminants back into the hydraulic system.

(5) <u>AM416 Relay Multiplexer</u>

The primary function of the AM416 Relay Multiplexer is to increase the number of sensors that may be scanned by the 21x datalogger. It is positioned between the sensors and the datalogger with mechanical relays used to switch the desired sensor signal(s) through the system. There are four lines which can be switched simultaneously while a maximum of sixteen sets of (four) lines may be scanned. This gives a total of 64 lines being multiplexed.

The number of sensors that can be multiplexed through one AM416 however, depends primarily upon the type(s) of sensors to be scanned. For example, there are up to 48 single-ended sensors that require excitation may be multiplexed (as in a half bridge), or up to 16 single-ended or differential sensors that require excitation may be multiplexed (as in full bridge).

Thus, the AM416 is intended for use in applications where the number of required sensors exceeds the number of datalogger input channels. Most commonly, the AM416 is used to multiplex analog sensor signals, although it may be used to multiplex switched excitations, continuous analog outputs, or certain pulse counting measurements. The

multiplexer plays a major role in the strain monitoring stages of the welded wire wall where in this case, simultaneous switching of 32 channels to read the strains in the wires is required.

(6) SR-4 Load Cell (Baldwin Lima Hamilton Corp)

The load cell translates changes in force or weight into changes in voltage. The sensitive element of the cell is a high-strength metal column, to which are bonded special strain gages. The gages are electrically connected to form a balanced Wheatstone bridge. A constant voltage is then applied across the opposite corners of the bridge so that a change in force of the cell, changing the resistance of the gage, will produce a change in the output voltage. The change in output voltage is then measured by an indicator or recorder which may be calibrated in units of force or weight. The schematic diagram of the load cell is shown in Fig. 4.

(7) Air Bag (Signode Corporation, Lake Ave., Glenview, Il.)

The type 800 expendable air bag used for pneumatic load control systems has a maximum inflating pressure of 8 psi. Since the maximum pressure expected in a 6 m high embankment far exceeds the allowable pressure and that the air bags cannot be deflated except by puncturing, some slight modifications were made at the entry tubes to facilitate two-way passage of air provided by the air compressor.

(8) Electrical Resistant Strain Gages and Accessories

The tension along the welded wire mats were monitored by reading the strains induced in the attached strain gages. The gages used were self-temperature compensating and were attached at various points of both the laboratory and welded wire wall mats. The following lists the accessories needed in attaching the strain gages.

(a) Conditioner A (water-based acidic surface cleaner)

(b) Neutralizer 5 (water-based alkaline surface cleaner)

(c) FTF-1 Degreaser

(d) M-Bond AE-10/15 and M-Bond GA-2 Adhesive Systems

(e) M-line Rosin Solvent

(f) M-Coat D (air-drying acrylic coating)

(g) M-Coat J3 (Polysulfide Protective Coating System) or Rubber Putty

(h) Aluminum Foil Tape

(i) M-Coat B (Nitrite Rubber Coating)

(9) ARC IBM Compatible Micro-computer (Model Proturbo 88) with Epson LQ-500 Dot Matrix Printer

The computer plays a very important role in the retrieval of data stored in the SM192 Storage Module when provided by an SC232 interface connnected at one of its COM ports. Direct programming of the 21x datalogger through the computer keyboard can also be enabled through the PC208 support software supplied by the Campbell Scientific, Inc. Direct printout of the retrieved data is facilitated by the Epson LQ-500 dot matrix printer.

(10) Air Compressor

The 1/4 HP rated capacity air compressor provides the means of maintaining a constant supply of air pressure to the air bag which applies the desired normal load during the pullout test.

VI. TENSILE STRENGTH TESTS OF STEEL REINFORCEMENTS

Tensile strength tests were performed on two sizes of steel bars, namely: 3/8" and 1/4". The strain gages were attached at mid-length where the cros-section was slightly reduced, to obtain uniform stress distribution and to localize the zone of fracture. The results are tabulated in Tables 1 and 2. The yield stress occurred at very low strains in the order of 0.4% to 0.5%. The modulus of elasticity of 194,737 MPa was obtained at 0.7 of yield strength.

VII. LABORATORY TESTS ON BACKFILL MATERIALS: ADDITIONAL RESULTS

Laboratory test results on backfill materials (weathered clay, lateritic residual soil, and clayey sand) not included in the Second Progress Report are discussed and presented in this section. These include the complete direct shear test results on the three types of backfill materials each having three compaction densities (85%, 90%, and 95% of standard Proctor compaction) with water contents within 1 to 2% dry of optimum. The Isotropically Consolidated Undrained (CIU) triaxial test results for clayey sand on three different compaction densities are also presented. Tables 3 and 4 show the complete summary of the shear strength parameters determined by direct shear test and CIU triaxial test, respectively.

VIII. FIELD TESTS AT THE WELDED WIRE WALL EXPERIMENTAL SITE

The field tests performed prior to the installation of any instrumentation (and subsequent construction of the embankment) in this period consisted of pressuremeter tests, vane shear tests, Dutch cone tests and screw plate load tests. Initial results of the vane shear and Dutch cone tests were presented in the Second Progress Report while the complete procedure and results are given in the subsequent discussions.

Pressuremeter Tests

The results of the pressuremeter tests are shown in Fig. 5. Pressuremeter tests were performed at the location of the main embankment at 2, 4, 6, 8 and 10 m depths. The apparatus used was $\frac{1}{3}$LLT Type M' (Lateral Load Tester) Model 4165 of the OYO Corporation of Japan. This apparatus is used to obtain the deformation characteristics of the ground from the relation between the pressure then given, and the corresponding expansion value of the rubber tube (sonde) in the borehole. The value of elastic moduli obtained at the various depths assuming plane strain condition and Poisson's ratio of 0.3 are 38.9, 42.4, 7.65, 25.72, 176.72 Kg/cm^2, respectively. From Fig. 5 it can be seen that the minimum value of net yield pressure and limit pressure occurs at a depth of about 6m and from then on increases with depth.

Vane Shear Tests

One vane shear test was performed at location of main embankment and the other, at the location of the control embankment. The results of these tests are shown in Figs. 6 and 7. The results obtained are similar to those of the previous tests. The maximum undrained shear strength in the undisturbed state at the location of the main embankment was of the order of about 3.25 t/m^2 at a depth of about 6 m. The minimum value, however, can be taken as about 2 t/m^2. In the remoulded state, the average undrained shear strength is of the order of about 0.5 to 0.6 t/m^2.

Dutch Cone Test

The results of the Dutch cone test are shown in Figs. 8 to 11. The Dutch cone apparatus consists of a 60 degree cone with a base area of 10 m^2, attached to the bottom of a rod protected by a casing. The tube, pressure rod and sounding cone assembly is driven into the soil (e.g. to 20 cm depth). Next, the rod extending from the tube is pushed down another 5 cm with the aid of a measuring unit. The cone is pushed by the rod at a

rate of 1 cm/sec. The force required to overcome the resistance encountered by the sounding cone is read on the gage and recorded and this is repeated every 20 cm. Cone resistance is the force required to advance the cone divided by the base area. Thus, it is possible to separate the point resistance and the friction on the outside of the casing.

The cone resistance and local friction in the weathered clay in the top 1 m is somewhat higher than in the soft clay below. The average value of cone resistance (Q_c) in the soft clay up to 8 m depth is about 60 t/m^2 and further below it, it increases rapidly. The average value of the local friction up to 8 m depth is about 1.5 t/m^2, generally increasing further below. The total friction increases with depth as seen in Fig. 10.

Screw Plate Load Test

The screw plate test involves carrying out load-deformation measurements without causing serious disturbance to the soil to be tested. Its behaviour being dependent on the vertical modulus is more appropriate in the present context, than the pressuremeter tests which measures the horizontal modulus. This test can be used to measure the undrained modulus, coefficient of consolidation and the ultimate bearing capacity. The apparatus used was designed and made in AIT based on the Australian design. It consists of a single cycle of helical auger with a diameter of 25.4 cm, thickness of 6 mm and pitch of 3 cm. The load is applied through a steel rod of 3.12 cm diameter. A 10-ton capacity hydraulic jack and a 10-ton capacity proving ring are used for applying and measuring the load. Time control tests were performed at 3 m and 6 m depths. The load was applied rapidly and then kept constant and the deflections were recorded on two dial gages placed diametrically opposite of each other. A time interval of 8 minutes was used and deflection readings recorded at 1, 2, 4, and 8 minutes for each load increment. The test was continued till failure, i.e., until when excessive settlements occurred with no further increase in the load.

Figures 12 and 13 show the plots of average stress and settlement which is expressed as a percentage of the radius. The ultimate bearing capacity is taken as the peak value of this load-settlement curve. Furthermore, the undrained modulus is calculated from the formula $E_{usp} = KP_a/w$, where K is the undrained modulus factor taken as 0.61 for the soft Bangkok clay, P is the applied stress, a is the radius of the screw plate and w is the plate settlement. The values of the ultimate bearing capacities obtained at 3 and 6 m depths are 18.66 t/m^2 and 16.74 t/m^2, respectively. The values of the undrained moduli at 3 m and 6 m depths have been found to vary between 350 to about 500 t/m^2.

Subsoil sampling

Subsoil samples were obtained at the location of the main embankment by using 10" diameter sampler and at the location of the control embankment by using a 3" diameter shelby tube sampler. However, at the location of the main embankment, 10" diameter samples could be obtained only up to 5.5 m depth. The recovery ratio of the 10" diameter samples further below being very low, only 3" diameter shelby tube samplers were used. The type of soil as could be seen visually from a sample at 5.5 m depth was sandy. Samples were obtained up to a depth of about 9 m at both locations.

IX. LABORATORY PULLOUT TESTS

Theoretical Background

General

As in conventional reinforced earth structures, the internal stability of the welded wire reinforced system consists of two basic components. The first component is the tension failure of the wires and the second is the pullout failure of the reinforcement. The first component can easily be verified for adequacy on the basis of the actual lateral stress imposed on the reinforcement of known cross-sectional area and allowable tensile stress. However, for the latter component, the mechanism of failure has not been fully understood yet. This is especially true for the case of the welded wire reinforcement where there are two components contributing to the pullout resistance compared to a single component of the strips used in conventional earth reinforcement.

The first component of the pullout resistance is that of friction between the reinforcement and the soil which is basically the only source of resistance for strip reinforcements. This frictional component of the pullout resistance is quite easily understood and determined theoretically.

The second component of the pullout resistance of welded wire mesh is the anchorage resistance offered by the transverse member. Unlike the first, the soil mechanism responsible for providing pullout resistance to the transverse member is not well understood and has been determined only empirically from laboratory pullout tests (Bishop and Anderson, 1978; Peterson and Anderson, 1980; Nielsen and Anderson, 1984).

Jewell (1984) viewed the interaction between the soil and reinforcement to be composed of three main mechanisms, namely: (a) soil shearing over plane reinforcement surface areas, (b) soil bearing on grid reinforcement bearing surfaces, and (c) soil

shearing over soil through grid apertures. Mechanisms (a) and (c) govern the resistance to direct sliding of soil over grid reinforcement, while the bond strength is governed by mechanisms (a) and (b).

Frictional Resistance of Longitudinal Bars

The frictional resistance developed along the longitudinal members of the welded wire mat as suggested by Peterson and Anderson (1980) for granular soils is a function of the overburden pressure, the coefficient of friction between reinforcement and the soil, and the surface area of the reinforcement. Thus, the frictional resistance F_f developed per unit length of a single longitudinal wire in a welded wire mat is

$$\frac{F_f}{L} = \sigma \pi d \tan \delta \tag{1}$$

where σ is the average overburden pressure computed from

$$\sigma = \frac{\sigma_v + \sigma_h}{2} = \frac{\sigma_v + 0.5\sigma_v}{2} = 0.75\sigma_v \tag{2}$$

d is the diameter of the wire, and

δ is the friction angle between reinforcement and the soil.

Jewell et al (1984) suggested a theoretical expression for direct sliding resistance of the geogrid. The loading condition is assumed to be characterized by the gross outward shearing force tending to cause a block of soil overlying a plane of reinforcement and the underlying soil. Thus, the direct sliding resistance arises from two contributions, namely: (1) the shear between soil and the plane surface areas of the grid, and (2) the soil shearing over itself in the grid apertures as mentioned earlier. Hence, neglecting any contribution due to the bearing in the transverse members, the direct sliding resistance can be determined using the following:

$$f_{ds} \tan \phi_{ds} = \alpha_{ds} \tan \delta + (1 - \alpha_{ds}) \tan \phi_{ds} \tag{3}$$

where: f_{ds} is the coefficient of resistance to direct sliding,
ϕ_{ds} is the angle of friction for soil in direct sliding,
δ is the angle of skin friction for soil on plane reinforcement, and
α_{ds} is the fraction of grid surface area that resists direct shear with the soil.

For design cases with reinforcement grids providing stability in embankments or retaining walls where the soil fill particles penetrate the grid apertures, a suitable value of maximum direct sliding resistance can be obtained by adopting a value $\alpha_{ds} = \alpha_s$, where α_s is the fraction of solid surface area in a grid (Jewell et al, 1984).

Bergado et al (1987) successfully predicted the pullout resistance of geogrids in the short term, undrained condition using cohesive frictional backfills. The adhesion resistance, F_f, was evaluated as

$$F_f = 2\mu A_f C_u \tag{4}$$

where μ is the adhesion factor between the soil and reinforcement, A_f is the total plan area of the geogrid, and C_u is the undrained cohesive strength of the soil defined by Ingold (1983) as

$$C_u = C + \sigma_v \tan \phi \tag{5}$$

where σ_v is the normal pressure at the level of the reinforcement in consideration which is equal to the overburden pressure. The upper limit of the adhesion factor, μ (=1) was used in the solution because of the larger values obtained from direct shear tests on reinforced soil.

The value of the frictional resistance is commonly determined in the laboratory by running pullout tests on mats with their transverse members removed such that only the contribution of the longitudinal bars to the total pullout capacity can be measured. Alternatively, the frictional resistance can also be estimated from different methods and published values of frictional coefficient (Bacot et al, 1978; NAVFAC DM-7, 1971; Schlosser and Elias, 1978) and employing any of those expressions given previously to determine the frictional resistance. It was found that the frictional resistance determined experimentally yielded higher values than those predicted theoretically (Peterson and Anderson, 1980; Chang et al, 1977).

Pullout Resistance of Transverse Wires

Most of the pullout tests conducted on reinforcements which employ the use of transverse wires confirm the idea that the bulk of the resistance to pullout is due to the anchoring effect of the transverse members. Chang et al (1977) were the first to recognize that the pullout resistance of a bar mesh made of 3/8" diameter smooth bars welded into a 4" x 8" grid, was approximately six times greater than for strip reinforcement embedded in the same soil with the same surface area and the same overburden. It was observed that the same bar mesh embedded in a

rather dense, silty-clay exhibited higher pullout resistance than when embedded in a gravelly-sand and was attributed to the effect of cohesion on the transverse bars. This phenomenon gave rise to the potential use of cohesive backfill in reinforced earth structures.

Bishop and Anderson (1979) obtained similar results when a 9 gauge wire, welded into a 2" x 6" mesh was used as reinforcement. The pullout resistance was estimated to be 5.5 times greater than when using strip reinforcement. Nielsen and Anderson (1984) concluded that the pullout resistance of welded wire mats is definitely a function of the number of embedded tranverse wires. The pullout resistance was observed to increase with the number of transverse bars embedded in the soil. Furthermore, it was found that the total pullout resistance can be related to the diameter of the wire and the friction angle and cohesion intercept of the soil.

Failure Mechanism for Transverse Members

The bar mesh in the pullout tests conducted by Chang et al (1977) developed a cone-shaped soil wedge at failure while the pullout tests with only longitudinal reinforcements failed by slippage of the bars through the soil. The failure mode seems to represent the full mobilization of the soil resistance which is the passive resistance developed in the soil. Because of this failure mode, it was concluded that the soil and reinforcement failed as a unit, and not individually, as did the strip reinforcement.

The bearing capacity mechanism is a form of passive resistance with a limited failure plane. Since the failure mode of each individual transverse wire was not observed by Chang et al (1977) except for the whole unit failure visibly seen on top of the soil, the failure mode for the entire mat acting as a unit may not necessarily hold true for each individual tranverse wire (Peterson and Anderson, 1980; Nielsen and Anderson, 1984). Thus, it was suggested that the transverse member can be thought of as a strip footing with conventional stress characteristic field for a footing rotated to the horizontal (Fig. 14). The relationship between the grid bearing stress (σ_b') and the overall normal effective stress in the soil (σ_v') as derived by Prandtl (1921) and Reissner (1923) is given by the following classical expression:

$$\frac{\sigma_b'}{\sigma_v'} = N_q = e^{(\pi \tan\phi)} \tan^2(45^o + \phi/2) \qquad (6)$$

This value of N_q can then be substituted to the Terzaghi-Buissman bearing capacity equation (Dunn et al, 1980) given as:

$$Q_{ult} = BcN_c + 1/2\gamma D_f B^2 N_\gamma + \gamma D_f N_q B \quad (7)$$

where Q_{ult} is the force per unit length of the strip footing. For welded wire reinforcement, the force per unit length of one transverse wire (F_p/Nw) can be equated to the above expression to obtain the theoretical estimate of the transverse resistance, hence:

$$\frac{F_p}{Nw} = Q_{ult} = BcN_c + 1/2\gamma D_f B^2 N_\gamma + \gamma D_f B N_q \quad (8)$$

For a welded wire transverse member of diameter d, with a corresponding overburden pressure σ_v, we can write

$$\frac{F_p}{Nw} = cdN_c + 0.5\sigma_v d^2 N_\gamma + \sigma_v d N_q \quad (9)$$

Since d is quite small, we can obtain the following general equations:

(a) <u>Cohesive-Frictional (c-ϕ) Soil</u>

$$\frac{F_p}{Nwd} = cN_c + \sigma_v N_q \quad (10)$$

b) Frictional Soil (c=0)

$$\frac{F_p}{Nwd} = \sigma_v N_q \quad (11)$$

where N is the number of transverse wires embedded in the soil, w is the width of the mat, and $N_c=(N_q-1)\cot\phi$. The assumption of a bearing capacity failure as the mechanism governing the passive resistance of the soil gives an upper estimate of the grid bearing stresses (Jewell et al, 1984).

Bergado et al (1987) closely predicted the bearing resistance of the transverse members in undrained condition using the following expression:

$$F_p = mA_b N_c C_u \quad (12)$$

where m is the total number of transverse members, N_c is the bearing capacity factor for a strip footing embedded in the soil as given by Skempton (1951) which is equal to 7.5 according to Ingold (1983), A_b is the cross-sectional area perpendicular to

the direction of pull of the individual transverse members, and C_u is given in Eq. 5. The total pullout resistance was obtained by combining Eqs. 4 and 12 to yield:

$$F_t = F_f + F_p = (2\mu A_f + mA_b N_c)C_u \tag{13}$$

The bearing stresses on vertical surfaces loaded horizontally have been studied for the case of anchor plates embedded in sand and in saturated clay (Rowe and Davis, 1982). The study reported extensive numerical investigations based on the finite element method, giving results which compared well with available data from anchor tests. Soil dilatancy, anchor roughness and initial stress state were considered in the theoretical formulation. It was reported that collapse load increased sensibly with embedment. It was also collated that for deep anchors, more extensive contained plastic deformation (local yield) occurs before collapse such that practical failure maybe deemed to have occurred at a load less than the true collapse load. For a cohesive-frictional soil, the anchor capacity q_u may be represented in the form:

$$q_u = c^* F_c' + \gamma h F_\gamma' \tag{14}$$

where c^* is the soil adhesion, F_c' is the factor to account for the effect of cohesion on anchor behavior and is a function of the embedment ratio, friction angle and surcharge pressure, and F_γ' is the factor for the effect of soil weight and is defined as

$$F_\gamma' = F_\gamma R_\psi R_r R_k \tag{15}$$

where F_γ is the anchor capacity factor for a smooth anchor resting in a soil which deforms plastically at a constant volume and $K_o = 1$. The factors R_ψ, R_r and R_k are the correction factors for the effect of soil dilatancy, anchor roughness, and initial stress state, respectively.

The value of c^* in Eq. 14 is computed to include the effect of the surcharge q, such that for soil with cohesion c and angle of friction ϕ:

$$c^* = c + q\tan\phi \tag{16}$$

Using the above equation, the factor F_c' is solved by also considering the influence of the surcharge on the breakaway of the anchor from the soil, i.e.

$$F_c' = F_c + q/c^* \tag{17}$$

where F_c is the anchor capacity factor for immediate breakaway. Charts are presented for the values of the factors F_γ, F_c, R_ψ, R_r and R_k.

The bearing stress of soil on grid members is a problem similar in kind to the base pressure on deep foundations in soil (Jewell et al, 1984). Accordingly, the bearing members of a grid, can be thought to be like a line of anchors at spacing s, with the grid diameter (d) likely small compared to the depth of soil, such that the bearing members can be considered deeply embedded, i.e., high value of h/d ratio.

For deep footings embedded in medium dense and loose sand models, the low bearing pressure observed have been associated with the punching failure mode in the soil (Vesic, 1963). The resulting stress characteristics and boundary conditions depicted in Fig. 15(a), can be used to obtain the value of N_q as:

$$N_q = e^{(90^\circ + \phi)\tan\phi} \tan(45^\circ + \phi/2) \tag{18}$$

Using the value of N_q given above to solve Eqs. 10 and 11, a lower estimate of the grid bearing stresses can be obtained as illustrated in Fig. 15(b).

A theoretical expression for the coefficient of bond strength (f_b) was formulated by Jewell (1980) and yielded a value of N_q intermediate to the values given by Eqs. 6 and 18. The general form of the equation is given as:

$$f_b = \alpha_s \frac{\tan\delta}{\tan\phi} + N_q \frac{d}{S} \frac{\alpha_b}{2\tan\phi} < 1 \tag{19}$$

where:

- α_s is the fraction of solid surface area in a grid,
- δ is the angle of skin friction for soil on plane reinforcement surfaces (δ/ϕ = 0.50 to 0.80 for sands and silts as given by Potyondy (1961)), and
- α_b is the fraction of grid width available for bearing and has a value of unity for welded grid.

The value of N_q can be measured directly in the pullout test to yield the coefficient of bond strength, f_b.

An analytical method for geogrid-reinforced soil structure was proposed by Ochiai and Sakai (1987) which considers the property of displacement dependence of the pullout resistance. The method assumes that when the geogrid laid in a soil is subjected to a pullout force, the resistance effect of the ribs at right angles with the direction of pulling is transferred to the grid junctions in a concentrated manner. The pullout resistance is therefore considered to concentrate and act on each of the grid junctions as shown in Fig. 16. It was concluded that the distribution of the pullout resistance acting on the geogrid is not always uniform even at the same level of vertical stress but varies with the displacement of the grid junctions in the soil. The strain (ε_{ij}) resulting from the displacement, X_i, of

each grid junction produced by the applied pullout force, F_t, in front of the geogrid can then be calculated by:

$$\varepsilon_{ij} = (X_i - X_j) / a \tag{20}$$

where a is the distance between each grid junction.

Fundamentals of Strain Determination Using Strain Gages

Basic Principles

From the basic mechanics of materials, the uniaxial strain (ε) of a homogeneous material with a constant cross-sectional area can be obtained as:

$$\varepsilon = \Delta L/L \tag{21}$$

where ΔL is the change in length and L is the original length. The unit of strain is thus dimensionless (length/length). In strain gage terminology, the units of strain are usually expressed in terms of micro-strain or micro-inches per inch.

Determination of strains using a strain gage is based on the principle that a wire produces an electrical resistance to the current flowing through it. This resistance will change as the length of the wire is changed. Thus, if the wire with an initial resistance (R_o) is stretched, the resistance will increase to some value (R_f) an amount which is equal to ΔR (= $R_f - R_o$). By dividing this change in resistance by the initial resistance, we can obtain a dimensionless number in units of resistance/resistance. This principle helps us to obtain a relationship between the strain induced in the wire and the change in the resistance normalized by the initial resistance. This relationship is normally expressed in terms of a factor called the gage factor (GF), which is a measure of the sensitivity of the strain sensitive alloy used in a strain gage. For commercial strain gages, the gage factor is a measured quantity which is determined by mounting several gages of a given type in a special calibration apparatus and measuring $\Delta R/R_o$ for a known value of strain (ε) in the calibration bar. The ratio of these quantities is then averaged to obtain the nominal value of the gage factor (GF) for that particular gage type. Thus, the gage factor, can be defined by the following equation:

$$GF = \frac{\Delta R/R_o}{\varepsilon} \tag{22}$$

For a specified value of the gage factor, the uniaxial strain can then be obtained for a given change in the gage resistance obtained from datalogger readings.

Determination of the Gage Resistance

To determine the unit resistance change $\Delta R/R_o$, both the potentiometer and bridge circuits as shown in Fig. 17 are used.

(1) Potentiometer Circuits

Figure 17(a), illustrates a basic circuit with two resistors. The voltage V_o can be calculated by using a voltage divider, such that

$$V_o = \frac{V_x * R_g}{R_g + R_1} \tag{23}$$

where V_o is the output voltage, i.e., the voltage across the resistor R_g, V_x is the excitation voltage supplied to the circuit, R_g is the resistor where the change in resistance is desired (e.g. strain gage), and R_1 is the resistor with the known value of resistance in the circuit.

Rearranging the above equation, we can obtain an expression for the strain gage resistance in terms of the input and output voltages and the known resistance R_1, i.e.

$$R_g = \frac{R_1 * V_o}{(V_x - V_o)} \tag{24}$$

Thus, the strain can be obtained using Eq. 22, for a gage with known gage factor as follows:

$$\varepsilon = \frac{\Delta R/R_o}{(GF)} = \frac{(R_g - R_o)}{GF * R_o} \tag{25}$$

Although the process of calculating strain from a strain gage using the above method is straightforward, there is one complication in that the measured change in the output voltage is usually very small. It can be verified that the output voltage can only change 0.001696 Volts from zero load to a 16,000 lbs load (Bourne, 1989). Thus, if the output voltage measurement system has only three decimal places of accuracy, it is not possible to detect the minute changes in output voltage necessary to predict the strain. Such a problem can be overcome using the Wheatstone bridge circuit and a differential voltage measurement system as discussed in the next section.

(2) Wheatstone Bridge Circuit

Figure 17(b) shows the schematic of a Wheatstone bridge circuit. It consists of two resistors in each of the two legs for a total of four resistors. The differential voltage measurement supplies an output signal, V_o, which is taken as the difference in the voltages at the center of each leg (i.e. $V_o=V_A-V_B$). Thus, with a measuring system that only handles three significant digits, it would be possible to measure the change in voltage necessary to calculate the strain.

The great utility of the Wheatstone bridge derives from its ability to "divide" the voltage (V_x) imposed across its power corners and supply an output signal (V_o) across its signal corners that is a function of V_x and the instantaneous arm resistances. The voltages V_A and V_B can be calculated as

$$V_A = V_x * \left[\frac{R_2}{R_1 + R_2}\right]; \quad V_B = V_x * \left[\frac{R_4}{R_3 + R_4}\right] \tag{26}$$

and V_o can then be expressed as:

$$V_o = (V_A - V_B) = V_x * \left[\frac{R_2}{R_1 + R_2} - \frac{R_4}{R_3 + R_4}\right] \tag{27}$$

Dividing both sides by the input voltage, V_x:

$$\frac{V_o}{V_x} = \left[\frac{R_2}{R_1 + R_2} - \frac{R_4}{R_3 + R_4}\right] \tag{28}$$

The ratio (V_o/V_x) is the output measured by the 21x datalogger using the full bridge measurement (Instruction £6). Thus, given the fixed values of the 3 instantaneous arm resistances, we can obtain the resistance of the strain gage which represents one arm resistance of the Wheatstone bridge. However, it would be convenient if the strains are computed using the differential voltage output (V_o) rather than the change in resistance of the gage (ΔR). If we denote R_2 to be the active strain gage element and R_1, R_3 and R_4 to be fixed resistors, the change in voltage ΔV_o will be due only to the change at V_A. Thus, straining the active gage element an amount of ΔR will give an expression for V_A as:

$$V_A = V_x * \left[\frac{R_2 + \Delta R}{R_1 + R_2 + \Delta R}\right] \tag{29}$$

Expressing in terms of the change in differential voltage ΔV_o, we obtain

$$\Delta V_o = V_x * \left[\frac{R_1 * \Delta R}{(R_1 + R_2) * (R_1 + R_2 + \Delta R)} \right] \tag{30}$$

For simplification, it is a common practice to have the same resistance of both resistors in the same leg of the Wheatstone bridge. For this reason, Eq. 30 then reduces to

$$\Delta V_o = V_x * \left[\frac{\Delta R}{2*(2R + \Delta R)} \right] \qquad \text{(Exact)} \tag{31}$$

Since 2R is generally much greater than ΔR, we can approximate the above equation to yield

$$\Delta V_o = V_x * \left(\frac{\Delta R}{4R} \right) \qquad \text{(Approximate)} \tag{32}$$

The strain can be solved in terms of the change in differential voltage ΔV_o by solving for ΔR in the exact solution and substituting into Eq. 22,

$$\varepsilon = \frac{4*\Delta V_o}{GF*(V_x - 2\Delta V_o)} = \frac{4*\Delta V_o/V_x}{GF*(1-2*\Delta V_o/V_x)} \qquad \text{(Exact)} \tag{33}$$

Similarly, for the approximate solution,

$$\varepsilon = \frac{4*\Delta V_o}{GF*V_x} = \frac{4*\Delta V_o/V_x}{GF} \qquad \text{(Approximate)} \tag{34}$$

From the above equations, it can be seen that the strain can be computed directly from the value of $(\Delta V_o/V_x)$ measured by the 21x datalogger. Also, the percent error of using the approximate solution is dependent on the gage factor but will not change significantly if it is close to two (Bourne, 1989).

Basic Principles of LVDT

The linear variable differential transformer (LVDT) can be used to measure displacement, linear velocity, fluid pressure and force. In the laboratory, the LVDT plays an important role in monitoring the displacement of the reinforcing mat as the pullout test progresses. With the data acquisition provided by the 21x datalogger, the LVDT provides an automatic monitoring system for the mat displacement, thereby minimizing the manpower needs during the test and increasing the accuracy which is inherent to automatic data acquisition.

As described in the 2nd Progress Report, the LVDT used for this project is a DC-DC model with a solid state oscillator and a phase-sensitive demodulator. Physically, it consists of two parts, the housing and the core. The housing contains three coils, one primary and two secondaries as shown in Fig. 18. The primary coil is placed in the center of the housing and the two secondaries are placed at equal distances on both sides of the primary.

The LVDT operates on the principle of mutual inductance. The displacement of the core changes the coefficient of mutual inductance between the primary and secondary coils, such that the coefficient of mutual inductance can be expressed as a function of the core displacement. Since the mutual inductance (MI) is related to the voltage (E) induced in the coil from the relation $E = -(MI)*(di/dt)$, where di/dt is the time rate of change of the current in the primary coil, the core position can also be related to the output voltage. This output voltage is a differential voltage between the two secondary coils and can be measured using the differential voltage measurement instruction of the 21x datalogger (Instruction £2). For an input voltage within the range specified by the supplier, the core displacement varies linearly with the output voltage.

The calibration data for the two models of the LVDT used in this project is given in Fig. 19 for a 12-Volt DC input. From the calibration curve, the core displacement (x) in cm can be obtained from the following equations:

$$x = 1.7036\ V_o + 8.3509 \qquad \text{(Long LVDT)} \qquad (35)$$

$$x = 0.6231\ V_o + 2.9969 \qquad \text{(Short LVDT)} \qquad (36)$$

where V_o is the output voltage measured by the 21x datalogger (in Volts). The long LVDT has a maximum displacement of $\pm$ 3 inches while the short LVDT has a maximum displacement of $\pm$ 1.5 inches.

Methodology

Instrumentation

As was discussed in the Second Progress Report, the pullout test was conducted using a 50"x 30"x 20" test cell made up of steel plates and steel channels. The normal pressure was supplied by an inflated air bag positioned between two flexible metal plates. The constant pressure maintained throughout the test was made possible through the use of a pressure regulator valve connected between the air compressor and the air bag.

The pullout force was applied to the test specimen using a hydraulic jack mounted against the supporting frame of the pullout cell (Fig. 20). The hydraulic jack was used due to some operational problems encountered in the servo-controlled hydraulic cylinder. The reinforcing mat was attached to the ram using a pullout clamp made up of two steel plates bolted together to enclose the protruding part of the mat. The grooved portion of the plates allow the gripping of longitudinal members to make a four-point contact surface with the clamp. Slippage of the clamp was further prevented using contraction joints gripped through the longitudinal wires (Fig. 21). The horizontal displacement of the mat was monitored using LVDT and a dial gauge positioned in front of the box and the mat specimen (Fig. 22). The horizontal displacement of the embedded portion of the mat was recorded using inextensible wires attached to the transverse nodes and connected to the dial gauges attached in the rear portion of the pullout box (Fig. 23). The inextensible wires are encased in stiff tubing to allow free movement in spite of the applied normal load. This procedure is a means of checking the relative movement of the transverse members during the loading process.

The strains along the longitudinal members including the bending of the transverse wire during the pullout was monitored by strain gages attached to some desired locations in the mat. The gages along the longitudinal members were attached diametrically opposite each other (top and bottom) and wired in series to cancel the bending stress such that only axial tension in the rod is recorded. On the other hand, those installed in the transverse members were also mounted diametrically opposite each other (front and back) and were wired independently of each other to measure bending during the pullout test. The typical schematic diagram of instrumented mats adopted in the laboratory pullout test is given in Fig. 24. The signals generated by the strain gages and LVDT are measured and recorded by the 21x micrologger and then stored in the SM192 storage module for later retrieval (Fig. 25).

Test Set-Up

In setting up the test, the pullout box was first assembled with only the bottom front cover plate in place. The soil specimen, which was cured to the desired moisture content, was then placed in three successive lifts. Each lift of about 8" was first compacted by tamping using concrete or wooden blocks, and then using a hand operated tamping machine up to a maximum compacted lift of 6" and to the required density of 95% standard Proctor. Control of density and moisture content was done by using the Troxler Nuclear Gage and alternately by the sand cone method. After the required density and moisture content is achieved, the surface of the first lift was levelled by slight tamping and the instrumented mat specimen was positioned in place. To ensure that the reinforcement is exactly in the middle of the slot after compacting the next successive lifts, the first lift height was adjusted to project about 1/2-3/4" higher than the top edge of the lower front plate. The wire extensometers were then installed at the desired locations in the mat. A capenter's level was used to ensure that the mat was horizontal. Horizontal 6" long metal plates were positioned across the width of the box near the slot, above and below the reinforcement to decrease the horizontal stress near the door face as well as to eliminate arching effect during pullout. This procedure also keeps the normal load off the front 6" of the specimen.

The upper front plate is then set in place and the mat is covered with soil in lifts as done in the previous step. A 1/4" thick "flexible" metal plate was then placed on the compacted soil with the air bag laid on top of it and the 5/8" thick cover plate was finally set in place. Three reaction beams, running across the length of the plates, were then bolted at the top flange of the pullout box.

Running the Test

After setting the apparatus, the desired normal stress was applied through the air bag and allowed to come to equilibrium for about 10 to 20 minutes. A seating load of 500 lbs. was applied to the loading ram to eliminate the slack in the whole system. The pullout rate was kept constant at 1 mm/min and was read through the dial gage mounted in front of the box. Readings of the load and displacements were periodically taken every 20 seconds until the mat was pulled to a maximum displacement of 2 to 2.5 cm. The normal pressure was then increased, necessary adjustments made, and the whole system was allowed to come to equilibrium by looking at the vertical dial gages. When no further vertical movements were detected, the load was again applied and subsequent readings taken. The normal pressure ranges from 1 to 13 t/m^2 for weathered clay and from 0.2 to 7 t/m^2 for the lateritic residual soil. After each set-up, the mat was removed by digging out the soil and the soil below the mat was then checked for compaction. The soil was removed and replaced by

fresh sample if the applied normal load compacted the soil to a great extent. However, to verify and to account for the strain dependency of the soil sample, further tests were made to duplicate the previous test but this time, with normal pressures overlapping that of the previous test.

X. DISCUSSION AND PRELIMINARY ANALYSIS

In this section, the discussion and preliminary analysis are separately made for the two backfill materials being tested so far, namely: weathered clay and lateritic soil.

Weathered Clay Backfill

Basic Properties

The soil specimen used is a reddish, inorganic weathered clay of low plasticity in the CL group. It has a plasticity index of about 24% and about 83% of which passes the U.S. standard sieve No. 200. The optimum moisture content is 22% at a maximum dry density of 1.60 t/m^3. The detailed summary of the basic soil properties is given by Bergado et al (1988b). In addition, the shear strength parameters obtained from direct shear and triaxial (UU and CIU) tests are tabulated in Tables 3 to 5 for different compaction densities.

Stress-Strain Relationship

A total of eighty-seven (87) pullout tests were carried out using welded steel bars of varying mesh sizes and bar diameters. The mats used consisted of 3/8" and 1/4" diameter steel bars with varying aperture sizes of 6"x9", 6"x12" and 6"x18". The backfill material was compacted at 95% standard Proctor densities at both dry and wet sides of optimum. Of these 87 tests performed, a total of 15 tests were invalidated due to weld failures. Also, several strain gages failed due to insufficient shielding and protection from excessive impact during compaction, and shearing during the test. It took several days to work out these operational problems and to get the test running smoothly.

Typical stress-strain relationships for the test performed on the dry and wet sides of optimum are given in Figs. 26 and 27, respectively. It can be observed that the pullout strength in the wet side compaction is very much lower compared to the dry side compaction. For all tests, the load-displacement curves indicated yield points where the curve seems to flatten out such that further increase in strain does not cause a significant increase in the load. The yield strength occurred at very low strains in the order of 1 to 2 mm displacements which is attributed to the low extensibility of the steel geogrids reinforcement. This can be further confirmed from the typical relationship exhibited by

the front displacement of the mat and the displacement measured by the inextensible wire extensometers attached at the grid junctions (see Fig. 28).

Some tests show indications of weld failures in the embedded mat through their load-displacement curves, where abrupt drop in the load at a rapid increase in strain is observed. This can be also depicted in the front movement of the mat in which usually the other edge of the pullout clamp moves faster. A typical photograph of the deformed mat after the test is shown in Fig. 29.

Adhesion/Friction Resistance of Longitudinal Members

Longitudinal bars in the welded mats provide pullout resistance through adhesion/friction between the soil and reinforcement. To determine the contribution of the longitudinal members to the total pullout resistance, some reinforcing mats with their transverse members removed, were pulled out at both dry and wet sides of optimum. Typical results are plotted in Figs. 30 and 31. As expected for poor quality backfills, the adhesion/friction component is quite minimal at about 3.5% of the total pullout resistance of the mat.

Effect of the Number and Diameter of Transverse Members

The magnitude of the passive resistance (F_p) contributed by the transverse members of the welded wire reinforcement was calculated from a known amount of adhesion resistance (F_f) due to the longitudinal members. Thus, for a mat with given diameter of the transverse members, a plot of the passive resistance per unit width of mat (F_p/w) against the overburden (normal) pressure is made as illustrated in Figs. 32 and 33. It can be seen that the passive resistance increased when the number of transverse wires was increased from 3 to 4, while further increase in the number of wires from 4 to 6 gave opposite results. This seems to suggest that there exist an optimum number of transverse wires (or mesh size) necessary for full mobilization of the shear strength of the compacted soil.

The plots of the passive resistance per unit width of the mat (F_p/w) as a function of the overburden pressure (σ_v) for a constant number of embedded transverse wires are shown in Figs. 34 and 35. As expected, the pullout resistance increased when using bigger diameter bars. This can be attributed to the optimal utilization of the internal friction of the soil as the failure planes around the wire increase in total length due to the increase in wire diameter (Nielsen and Anderson, 1984). This full mobilization of the bearing resistance of the transverse members are obviously seen for tests conducted at wet side of optimum.

Pullout Resistance

The maximum pullout force for a typical mesh size is plotted in Fig. 36a,b. The result showed that the pullout resistance increased with the number of embedded transverse bars and vertical stress. The higher strains measured in the dry side compacted backfill reflected the higher mobilized pullout resistances as compared to the wet side compaction. On the basis of the preliminary results presented, it seems that the 6"x9" mesh size was superior for both the dry and wet compacted densities of the soil.

Lateritic Residual Soil

Basic Properties

The soil specimen used was obtained from Saraburi, Thailand and is classified as lightly brownish, well graded clayey gravel (GC). The sample has an average specific gravity of 2.61, a plasticity index of about 16%, and about 18% fraction which passes U.S. standard sieve No. 200. The optimum moisture content averaged at about 11.5% corresponding to a maximum dry density of 1.93 t/m^3. Detailed summary of the basic properties is given by Bergado et al (1988b).

The shear strength parameters obtained from direct shear and triaxial (UU and CIU) tests for higher normal pressures (5 to 20 t/m^2) are tabulated in Tables 3 to 5. For low normal pressures (0.2 to 1.8 t/m^2), a specially-designed direct shear apparatus was fabricated by Amin (1989) to investigate the behavior of the sample. As was expected, the failure envelope of the specimen yielded higher values of friction angle (ϕ) at low pressures than at higher normal pressures. This result has been attributed to the particle breakage of residual soils when sheared under high normal pressures (Bergado et al, 1988a). The result of direct shear tests on lateritic residual soil at three different standard Proctor compaction densities (dry, optimum, wet) are depicted in in Figs. 37, 38 and 39.

Stress-Strain Relationships

A total of forty-eight (48) pullout tests on welded mild steel bar grids were performed using lateritic residual soil as backfill material. The tests were conducted at low pressures of 0.2, 0.8, 1.3 and 1.8 t/m^2. The wire mats used consisted of 1/4" and 1/2" diameter steel bars with varying aperture sizes of 6"x9" and 6"x6". The tests were also conducted at different backfill compaction densities of 95% and 100% standard Proctor compaction with moisture contents at optimum and $\pm$ 2% dry and wet sides of optimum. As in the weathered clay backfill, some of the tests required repetitions due to weld failures and operational problems. To verify the extent of strain-dependency and particle

breakage during the test, a second set of test with normal pressures of 1.3, 1.8, 3.6 and 7.2 t/m^2 was conducted.

The typical load-displacement curves for pullout tests on reinforced lateritic residual soil are plotted in Figs. 40 to 42. It can be seen that the pullout resistance increases rapidly at first and then flattens out up to a maximum of 20 mm displacement. This indicates that even at small displacements, a higher pullout force is required at the initial stages of pulling. Also, in all the tests at low normal pressures, there seemed to be no well-defined peak in the stress-strain curves, although the pullout resistance increased with increasing normal pressure. As observed for weathered clay backfill, the yield strength occurred at very low strains in the order of 1 to 4 mm displacements due to the inextensibility of the steel grids.

Variation of Strains and Mobilized Resistance with Distance

The typical strains recorded by the strain gages at various locations in the longitudinal bars of the mat are plotted in Figs. 43 and 44. It can be seen that the strains vary linearly with distance from the front face of the box, with the largest value near the face.

In most cases, the displacement of the rear end of the mat measured from the back dial gages agreed very closely with the front horizontal displacement measured by another dial gage. This implies that the mat moved more like a rigid body without undergoing unduly large strains. The large deflections of the transverse bars were observed only with smaller diameter bars. The strains measured were in the order of 0.1% to 0.5%, typical for inextensible reinforcements as reported by Yokota et al (1988).

The typical plots of mobilized passive resistance at grid junctions versus distance from the face, computed using the method suggested by Ochiai and Sakai (1987), are shown in Figs. 45 and 46. It can be observed that the mobilized resistance is larger near the face and decreases approximately linearly with distance. This variation was confirmed from several tests in which weld failure occurred at the third point (3rd or 4th transverse wire) of the mat.

Variation of the Passive Transverse Resistance with Normal Pressure

Since the frictional component of the total pullout resistance is only minimal and not as important as the passive resistance of the transverse members, the contribution from the longitudinal members were only estimated using Eq. 1 to obtain the friction/adhesion component. The maximum frictional resistance was calculated to be about 5% of the total pullout force for the lateritic soil compared to 3.5% obtained for

weathered clay from actual test. The values of the frictional resistance (F_f) were subtracted from the total pullout resistance (F_t) to obtain the passive resistance (F_p) of the transverse members. The passive resistance per unit area of the transverse bars normal to the direction of the pullout (F_p/Nwd) was plotted against the normal pressure (σ_v) as shown in Figs. 47, 48 and 49. The y-intercept can be viewed as the component cN_c while N_q represents the slope of the line. These values came out to be high enough in which N_c ranged between 15.54 and 138.5 while N_q ranged between 4 to 95 for all the 3 compaction densities. The plots also depict the influence of the mesh geometry and the size of the transverse bars to the passive resistance. In all cases, the value of F_p/Nwd definitely increases with increasing vertical normal stress. An important observation from all these tests is that the 1/4" diameter bar gives a higher value of the passive resistance than the larger 1/2" diameter bar. This can be attributed to the lower strains experienced by the larger diameter bars leading to partial mobilization of the bearing resistance. This observation is in accordance with what was observed by several other investigators (Chang et al, 1977; Hannon and Forsyth, 1984).

Another important observation from these plots is that generally, the 6"x9" mesh geometry seems to be the most efficient section for both sizes of bars and all compaction densities used in this study. This observation was also detected by earlier investigators for both granular and cohesive backfills (Mitchell and Villet, 1987; Nielsen and Anderson, 1984). Figures 47 to 49 depict the differences between the behavior at three compaction densities (dry, optimum, wet) and it is evident that the wet side compaction generally seemed to give the lowest pullout resistance.

Predicted Pullout Resistance

The experimental results obtained in the laboratory, are analyzed and compared to the various expressions proposed to predict the passive resistance as were discussed in the previous section on theoretical background. The method proposed by Bergado et al (1987) for undrained condition, closely predicted the total pullout resistance for both bar diameters (1/4" and 3/8") using weathered clay backfill compacted at the dry side of optimum (Figs. 50 and 51). For lateritic residual soil, however, best agreement with the observed data was observed for the dry side and optimum moisture contents (Figs. 52 and 53). Underestimation resulted for the wet side compaction (Fig. 54).

For the prediction of passive resistance of the transverse members, the bearing capacity failure mechanism proposed by Peterson and Anderson (1980) seems to overestimate the magnitude of the passive resistance normalized with respect to the mesh geometry of the grid (F_p/Nwd) for the dry side compacted weathered clay backfill. The model, however, yielded a good

agreement with experimental results for the wet side compaction (see Figs. 55 and 56). Similar observation was deduced for the lateritic soil compacted at both the dry side and optimum moisture in which overprediction resulted (Figs. 47 and 48). Fair agreement was obtained for the wet side compacted laterite (Fig. 49). The difference in behaviour exhibited by the two backfill types maybe due to the low pressure range adopted for the lateritic residual soil.

The close agreement observed in the wet side compaction maybe be due to the full mobilization of the passive resistance for the wet side compacted sample compared to the dry side compaction. Also, the full development of passive resistance is obvious for the smaller diameter bar (Fig. 49). This result is in accordance with the mobilization of larger strains for 6 mm (1/4") than for the 12 mm (1/2") diameter reinforcing bars.

The punching failure mode proposed by Jewell et al (1984), which can be developed for conditions of small strains, seems to closely predict the actual behaviour of the soil-grid interaction in terms of the mobilized passive resistance in the dry side for both soils (Figs. 47 and 55), and for optimum compacted laterite (Fig. 48). The model slightly underestimated the passive resistance in the wet side compaction for both soil types.

The method of Rowe and Davis (1982), which was developed for horizontal and vertical anchors using the finite element method, seems to give the best agreement for the weathered clay backfill at two compaction conditions (Figs. 55 and 56) and for the lateritic soil compacted on the dry side of optimum (Fig. 47). The method slightly underpredicted the passive resistance for both the optimum and wet side compaction (Figs. 48 and 49).

XI. ANALYSIS AND DESIGN CONSIDERATION OF WELDED WIRE WALLS

As in other types of retaining walls, the welded wire walls must be designed to meet both external and internal stability criteria. These criteria are affected by primary factors such as internal loadings, foundation conditions, backfill properties, drainage, and geometric constraints (Nelson and Selvage, 1987). For external stability, the entire mechanically stabilized mass is treated as a rigid gravity retaining wall with active soil pressures applied behind the wall (Anderson et al, 1986; Anderson et al, 1987). Thus, external stability criteria often requires the wall to have adequate safety factor against overturning, sliding, bearing capacity and overall slope stability. Bearing capacity and overall slope stability requirements may be critical for walls on soft foundation conditions.

The internal stability, on the other hand, considers the design of the reinforcing elements. This usually involves considering the adequacy of the longitudinal wires against tension failure as well as the system resistance to pullout.

Tension in the Longitudinal Wires

The tension in the longitudinal wires depends on the lateral soil pressures that are developed within the welded wire wall. The magnitude may be determined experimentally by measuring tie-rod forces in prototype walls constructed in the field or in model walls constructed in a load cell (Anderson et al, 1986).

The magnitude of the tension can be determined by assuming that each longitudinal wire provide the lateral restraint for an area that extends half the distance to the adjacent wires above, below, and on both sides, i.e.

$$T = \sigma_h(w)(d) = K\sigma_v(w)(d) \tag{37}$$

where: T = tension in the longitudinal wire,
K = lateral earth pressure coefficient,
σ_v = overburden pressure,
w = horizontal spacing of the longitudinal wires, and
d = vertical spacing of longitudinal wires.

The amount of yielding that can take place dictates the value of the coefficient, K. For welded wire walls, K is recommended to vary between the at-rest condition and the active condition and must be determined experimentally (Anderson et al, 1986, 1987; Anderson and Wong 1987). Based on results from laboratory and field performance of a 23-ft high wall, Bishop and

Anderson (1979) recommended an average value of 0.65 for design. Hannon and Forsyth (1984) measured at-rest values of K on a grid reinforcement wall. McKittrick (1978) recommended K values which vary linearly from the at-rest case at the top of the wall to the active case (K_a) at a depth of 20 feet for a Reinforced Earth wall. Below a depth of 20 ft, active values for K were recommended. All the recommendations stated above were based on walls constructed of granular backfill materials. Thus, for walls constructed of poor quality cohesive backfills, higher values of K may be expected.

Pullout Resistance of Welded Wire Mats

The mats in welded wire walls must be designed to develop sufficient pullout resistance behind the failure plane to support the tension forces induced in the longitudinal wires. Hence, the longitudinal reinforcement must extend far enough behind the potential failure surface to restrain a failure mass from sliding. The potential failure surface can then correspond to the point of maximum tension in a mat for that elevation. Measuring the tension in the longitudinal wires at a number of locations back from the face of the wall gives an understanding of the location of the potential failure surface.

The pullout resistance of welded wire mats was shown to be a function of: (1) the number of embedded transverse wires behind the failure plane, (2) the diameter of the transverse wires, (3) the overburden pressure, and (4) the number, diameter, and length of the longitudinal wires which develops frictional resistance behind the failure plane (Nielsen and Anderson, 1984). A safety factor of two against pullout is generally required for internal stability. Limiting the pullout deflection to 0.75 inches implicitly establishes a deflection criteria for the internal stability of the wall (Anderson et al, 1986).

XII CONSTRUCTION PROCEDURE, INSTRUMENTATION, AND MONITORING PROGRAMS FOR THE WELDED WIRE EXPERIMENTAL WALL

Construction Procedure

The welded wire experimental wall was divided into three sections along its length, each about 16 ft long, and utilizing three different backfill materials (Fig. 57). It consisted of a vertical welded-wire reinforced wall facing on one side, and a sloping unreinforced opposite side as shown in Fig. 58. The parts of the welded-wire wall are shown in Fig. 59. The reinforcement mats, consisting of W4.5 x W3.5 wires with 6" x 9" grid openings and each 8' wide by 18'9" long including the facing, were instrumented with strain gages in the main body of the embankment for various backfills. A typical instrumented section of the wall is shown in Fig. 58. A minimum of about 7 instrumented layers for each backfill were provided. The instrumentation points are described in detail in the instrumentation program together with the details of the dummy reinforcements for field pullout tests. The embankment construction was carried out following the Construction Guide for Welded Wire Walls presented by the Hilfiker Company (1988). It involved placement of the reinforcement with the bent-up portion of the reinforcement forming the casing. Backing mats and screen were provided along the vertical side of the wall to prevent erosion of the soil. The fill was then placed and compacted over the reinforcement at a specified compaction lift. The process was repeated until the full height was reached of about 18'6" above the ground level. The construction procedure is described in detail in the following discussions.

The first layer of reinforcement mats were laid 18" below the ground level. Correct spacing between mats were facilitated by the 6" spacers (Fig. 60). Wooden stakes were used to hold the reinforcement mats in place during backfill placement. These were subsequently removed when the mats were weighted with fill. Mats at both longitudinal ends were cut to fit the embankment dimensions. This was done by cutting only the transverse wires. Backing mats were then placed against the face of the wall and clipped with hog rings in such arrangement as shown in Fig. 61. The screen was also clipped in place with hog rings (Fig. 62). Three backfill materials were then placed at each of the different sections of the embankment. Backfill layers between reinforcement mats were placed and compacted in three equal lifts. Each lift was compacted by both roller and hand tamper to the density of about 95% standard Proctor compaction. Moisture content was maintained within 1-2% on the dry side of optimum. Moisture-density control was made using the Troxler Nuclear gauge. The completed backfill in each layer must be in the form and at the depth shown in Fig. 63. Underfilling would cause excess bulging in the face of the wall. The void between the backfill and the wall would be filled with gravel as soon as the

next reinforcement layer was installed and fixed in place. The gravel only required slight compaction effort against the wall and hence avoid possible damage in the wire or bending the mats. In addition, it would also help prevent erosion of the backfill at the face of the wall. The reinforcement mats for the next layer were then placed to match the 6" spaces between the mats in the layer below. The bottom of upper mat rested on top horizontal wire of the lower mat as illustrated in Fig. 64. Wooden stakes were used to hold the mats in place and were removed when the mats were already weighted with fill. A string line provided horizontal and vertical alignment as shown in Fig. 65. The placement of backing mats for the second layer of reinforcement and onwards were different from that of the first layer. This was done by sliding the bottom wire of backing mat down between face of wall and prong until it stopped against bent part of prong while the second wire of backing mat was kept outside of prong as illustrated in Fig. 66. Placement of screen as well as backfill materials were the same as in the preceeding layer. The procedure was repeated until the desired embankment height was reached. The final layer of reinforcement was provided by the prongless reinforcement mat. The top cap was tilt to catch the front hook under second wire of face of prongless mat as shown in Fig. 67. The final grade of the embankment was 6" over the top cap. Figures 68 and 69 show the photographs of the experimental site for different stages of the wall construction.

Purpose of Instrumenting the Wall

An instrumentation program was developed to evaluate the performance of the welded wire wall. The purpose of the instrumentation program was to determine the relationship between the tension in the longitudinal wires and the height of the wall, and to find means to relate this to the soil parameters that could be used for design. Since the wall is founded on a soft clay subsoil, several other field instruments were installed both at the subsurface and in the wall itself. Thus, an extensive monitoring program for the wall consisting of settlement measurements, pore pressure monitoring, lateral movement monitoring and measurements of the pressure at the base of the wall was carried out since the beginning of construction. These measurements are of utmost importance as the behavior of the wall is highly dependent on the response of the flexible clay foundation. The photograph of the site just after the installation of the subsoil instrumentation is given in Fig. 68(a).

Periodic monitoring of the wall is ongoing as settlement continues in order to evaluate the post construction and long term performance of both the wall and the soft subsoil. Some dummy mats instrumented with strain gages for field pullout tests were also installed at different levels to compare the results

obtained from the laboratory. Uninstrumented dummy mats for corrosion testing were also embedded at different depths for each section of the wall. These mats will be tested for strength after some period of time to evaluate the effect of corrosion in reducing the tensile strength of steel.

Scope of the Instrumentation Program

Three different sections of the wall were instrumented. Silty, clayey sand backfill with about 45% passing the No. 200 sieve was used in Section I of the wall. The middle section (Section II) used a higher quality backfill material (lateritic residual soil) with 18% passing sieve No. 200. The reddish weathered clay backfill material with 83% passing sieve No. 200 was used in Section III.

The instrumentation program involves measuring the tension in the longitudinal wires at 12 locations on each of the bottom four instrumented mats and at 10 locations on each of the top 3 instrumented layers for each of the three sections of the wall. Thus, for the entire length of the wall, a total of 21 layers are instrumented. This gives a total of 234 instrumentation points within and throughout the length of the wall. In addition to these, a total of nineteen (19) dummy mats (Fig. 70a,b) for field pullout tests were also instrumented at selected points in the mat and embedded at different locations within the height of the wall. Additional seven (7) mats for corrosion observation and testing were also embedded at different depths of the wall.

Aside from the tension measurements made in the wires, nineteen settlement plates, 10 at the subsurface and 9 at the surface, were installed at different locations along the wall length. Four pneumatic piezometers and 6 hydraulic piezometers were used in conjunction with the settlement devices to monitor the excess pore pressure developed in the soft clay subsoil. Five SINCO inclinometers (3 at the front, 1 at the middle, and 1 at the back) were installed to measure the lateral movement of the vertical and sloping faces of the wall. The base pressure distribution at the mid-length of the wall was also monitored using 3 total pressure cells. The schematic layout of the field instrumentation is given in Fig. 71.

Description of the Instrumentation Program

Tension Measurement

The tension force in the longitudinal reinforcement is measured using self-temperature compensating electrical resistant strain gages manufactured by Micro-Measurements. Two strain gages were installed at each measurement point and were attached at diametrically opposite sides of the wire and then wired in series. This configuration of wiring the gages, as previously discussed, causes bending stresses in the wire to cancel, thus only the axial tension in the wire is measured. The locations of the strain gages for the bottom four and top three instrumented layers are given in Figs. 72 and 73, respectively. A systematic way of wiring the gages was done by establishing a definite convention such as assigning the red wires at the top gages, and the black ones at the bottom. A short white wire was used to connect the legs of the top and bottom gages together. The other wire (white) was connected to the common leg of the top strain gage. Connecting the two ends of any of the three wires to a measuring device enables one to measure either axial tension (red and black) or the magnitude of bending (red-white and black-white). The wire leads from the gages were bundled into one set of 12 for each mat and were placed into a conduit that extended down the face of the wall to a monitoring station (Fig. 74a). Each bundled lead wires were connected to a 12-pin quick-connect plug (Fig. 74b) which could then be quickly plugged into the switching unit of the AM416 multiplexer for ease in making the readings.

The 21x datalogger was attached with precision, completion resistors such that activation of the AM416 multiplexer completes the full-bridge circuit measurement scheme. The measurement consists of two sets of bridge completion units. One set enables the measurement of each strain gages in series while the other was designed to measure the gage resistance independently of each other. The amount of bending in the wires can then be calculated from the knowledge of stresses at the top and bottom portions of the wire.

Initial readings were taken at the time the mats were installed to indicate the strain reading corresponding to zero tension in the wires. Subsequent readings were then taken as the wall was constructed. The difference between the initial reading and a subsequent reading is a measure of the strain induced from the backfill placed over the mat at the time of the measurement. From the measured strain, the tension in the wire can be

computed, given the modulus of elasticity and the cross-sectional area of the wire using:

$$T = \varepsilon * E * A$$

where: T = tension force in the wire,
ε = axial strain,
E = modulus of elasticity of steel, and
A = cross-sectional area of the wire.

The computed tensions are plotted for each mat as the wall height increases as typically shown in Figs. 75(a) to 77(a) for each section of the wall. Lines corresponding to different values of K are also shown to estimate the range of values during the construction stage as the wall height increases. It can be seen that the value of K ranges from the active value to the at-rest (K_o) value for cohesive backfills compacted in layers. The tension in the wires plotted with distance back from the face of the wall are also typically given in Figs. 75(b) to 77(b). The line representing maximum tension in the reinforcing mats seems to vary at a location ranging from 2 to 6 feet from the face of the wall. This preliminary behaviour during construction seems to agree with the results of Anderson et al (1987). However, detailed analyses will be made for the post-construction performance of the wall, especially for this specific case where the wall is resting on a very soft foundation.

Lateral Movements

Lateral movements of the subsoil and the embankment were measured using a Digitilt Inclinometer. Three of these (I1 to I3, in Fig. 71) plastic casings were installed vertically near the face to measure the lateral movement of the wall and the subsoil. A fourth casing (I4) was installed in the non-reinforced middle section at the point where the back slope intersects the top. The other casing (I5) was installed at the toe in the back and this measures only the subsoil lateral movements. The grooves of the casings were oriented in the directions of the principal movement, i.e., in a direction perpendicular to the face of the wall. The torpedo or the sensor is lowered into the casing with the proper polarity and the guide wheels move in the opposite grooves. The torpedo is suspended vertically by the interconnecting cable. The other end of the cable is connected to the Digitilt indicator. Inclination readings were read at every 0.5 m. Consecutive readings at the same depths, taken at periodic intervals of time, can be converted into lateral movements.

The plots of depth/height versus lateral movements for each of the five casings are shown in Figs. 78 to 82. It can be seen that in all these plots the maximum lateral movement in the subsoil occurs at a depth of about 3 m, i.e. where the soft clay exists. In 29 days of observation beginning from the day the construction ended, the lateral movement of the top of the wall is about 110 to 120 mm. The maximum lateral movement of subsoil at about 3 m depth from the beginning, is of the order of about 80 to 110 mm, as measured from I1 to I3. The subsoil lateral movement, as well as that of the face of the wall which is tilting outwards, is continuing even after the construction has ceased. It can be seen from Figs. 83 to 85, that the rate of vertical movement has slowed down enormously at both 3 m and 6 m depths near the face, but the lateral movement continues to occur at a faster rate than in the initial stages of construction, especially at 3 m depth. This indicates that the soft clay is being squeezed out from beneath the embankment, simultaneously with the dissipation of the pore pressures.

The direction of the subsoil lateral movements in I4 and I5 are opposite to that of I1 to I3 near the face and also the magnitude of the lateral movement is small in comparison. I5 records a lateral movement of about 28 mm in 29 days after construction at about the same 3 m depth (Fig. 82). Therefore it is seen that the soil is being squeezed out from beneath the embankment, both from the front and from the back, but predominantly from the front.

Casing I4 became unusable at 3 m depth and below during construction, at the joint. At the joint, the casing above/below must have moved more in excess of the other, making it difficult to insert the torpedo, and once it is inserted, the torpedo gets locked in the constriction making it much more difficult to take it out. It should be noted that each casing pipe is 10 feet in length and a coupling joins two such casings to extend it in length. Therefore, subsequent readings (and thereby the curves in the plot of Fig. 81) have been taken only from about 3 m depth and above.

The outward inclination of the wall face is a reflection of the lateral movements of the subsoil and settlements near the face. The excessive lateral movements at about 3 m depth indicates that any (rotation) failure surface that is being developed or likely to develop will pass through this soft clay layer at this depth, which offers the least resistance to the incumbent forces. However, it will need some more time of monitoring and observation to decisively conclude the exact path of the failure sufaces. In all probability, it is not likely to cut through the reinforced section and possibly might be starting somewhere on the backslope and pass below the reinforced section through the soft clay layer at about 3 m depth and emerge out in front of the face at some distance.

Settlements

Settlements are measured by levelling with reference to a bench mark. The surface settlement plates (9 of them in all, see Fig. 71, showing the instrumentation layout beneath the embankment) were placed below the bottom-most reinforcement layer at 0.45 m depth. It should be noted that the whole area of the embankment was first excavated to a depth of 0.45 m (18") before installing the instrumentation in the subsoil and at the surface. The first layer of reinforcement was placed over the surface settlement plates at -0.45 m. The surface settlement plates consist of a 16 mm dia. steel rod connected to a 0.4 m X 0.4 m base plate and protected by a 19 mm dia. casing of GI pipe. The subsurface settlement gages (10 in all) consist of a 25 cm diameter steel screw head connected to a 16 mm dia. steel rod. These are screwed into the ground by means of 19 mm inner diameter steel tube which is attached to the screw head by a keyway. After installation to the desired depth, the outer tube is lifted from the keyway by about 20 cm. The tube is left in the ground and filled with oil to eliminate the drag down forces on the inner rod caused by the compression of the clay. Settlement readings are taken at regular intervals of time both on the surface and the subsurface settlement gages. The temporary bench mark is situated in front of the embankments at the right corner in a fence, from which levels are run to the top of embankment via the ramp. The permanent bench mark (located on the top of a well, considered to be unyielding) is situated some distance from the embankment site and levels are run from this permanent bench mark to the temporary bench mark once every month to account for the effects of subsidence.

Of the 10 subsurface gages, 4 of them are installed at 6 m depth (SS1, SS3, SS5 and SS9) and the rest are installed at 3 m depth. SS1, SS3 and SS5 are at 6 m depths near face beneath each of the backfill soils, respectively, and SS9 is at 6 m depth, 3 m from face below the weathered clay.

The surface settlements at the front near the face have been identical below all the three types of backfill soils (Fig. 86). However, it is observed that the maximum surface settlement is in the very center (S5) (see Fig. 87) and the deformed shape of the surface is somewhat like a dish. Settlement of S5 shot up considerably beyond that of its counterparts S4 and S6 somewhere near the end of construction as seen in Fig. 87. The settlements are more or less symmetrical about the centre line, perpendicular to the face. The end sections (S1-S4-S7 line below clayey sand and S3-S6-S9 line below weathered clay) show larger settlements at the front and that the settlements decrease as we go towards the back. But the middle section (S2-S5-S8 line below laterite) shows maximum settlement at the center, i.e. S5, followed by the settlement near the face (S2) and the settlement at the back (S8). With all these surface settlement plates, the rate of

settlement has reduced considerably from the time that the construction has ceased (Figs. 86 to 88). SS1, SS3, and SS5 (Fig. 89) show almost identical settlements with time, but settlement of SS9 (Fig. 90) is slightly higher than near face, due to higher vertical stresses at the middle. The magnitude of the settlements recorded at 3 m depth is in between that recorded at the surface and at 6 m depth, at or near about the same area. SS2, SS4, and SS6 near the face at 3 m depth show considerable scatter (Fig. 89). SS7 and SS8 show almost similar settlement patterns (Fig. 91). SS10 is the lone settlement gage far back (5.5 m from face) in the middle section at 3 m depth, also shows similar pattern of settlements as other the gages at the same depth (Fig. 92). Again with all the subsurface gages, the rate of settlement has decreased considerably in the post construction phase.

Excess Pore Pressures

Pneumatic piezometers and hydraulic piezometers (closed type) are used to measure the pore pressures. These have been installed at various depths at different points beneath the embankment (see Fig. 71). Two pneumatic transducers are placed in the embankment backfill in the weathered clay at +[illegible] m and +4 m. The Sinco pneumatic transducers used (6 in all, 4 of them in the subsoil and 2 in the embankment backfill soil) are connected to a digital pneumatic pressure indicator and pore water pressures are read almost immediately. But the hydraulic piezometers, one end of which is connected to a mercury manometer, requires a laborious procedure of de-airing the system with the other end before readings are taken. This second line is used as a de-airing line by flushing water through the piezometer system (with the help of a pump) from one tube to the other. De-airing needs to be done frequently to obtain reliable readings. After de-airing, considerable time must be allowed for the system to stabilise, usually overnight, and then readings are noted on the mercury manometer. On the other hand, the pneumatic transducers make use of nitrogen gas to obtain pore pressure readings. A compact nitrogen tank is accommodated in the digital pneumatic pressure indicator itself.

Of the four pneumatic piezometers installed in the subsoil, three were damaged during construction, probably due to excessive settlements and only N2 is functioning. Hydraulic piezometer H1 could be activated only after construction was completed. All the piezometers show an increase in the total porewater pressure during construction and development of excess porewater pressure, which also increased during the full phase of construction. Both of these, total porewater pressure and the excess porewater pressures showed a decrease, almost immediately after the construction had ceased and continues to show a decline at a very slow rate (Figs. 93 to 101). This dissipation of excess porewater pressure indicates that the process of consolidation is

taking place in the subsoil due to the embankment loading. Also seen in these figures is the increase in vertical stress as calculated by the method suggested by Poulos and Davis (1974). In all cases, the excess porewater pressure developed is far below the consolidating pressure (increased vertical stress as calculated by the Poulos and Davis (1974) method).

The porewater pressure coefficient r_u defined as the ratio of the porewater pressure at depth Z(u) to the vertical pressure at depth Z (i.e. γZ) was found to be in the range of about 0.3 to 0.35. A value of r_u equal to unity expresses an extreme and critical condition wherein the effective stresses are zero (quick sand condition). The long term stability should only improve with the dissipation of the excess porewater pressure with time. Another important factor influencing this long term stability at the present site is the fluctuating water table, which could be very close to the ground level in the rainy season. N2 and N3 which are at relatively shallow depths, i.e. 2 m and 3 m depths, respectively, show the total porewater pressure less than the consolidating pressure and almost close to the excess porewater pressures, unlike in N1 and N4 which are at greater depths of 5 m and 6 m, respectively. A similar observation could be made with the hydraulic piezometers H3 and H6 in comparison with the other hydraulic piezometers.

Earth Pressure at the Base of Wall

To determine the vertical pressure distribution along the base of the wall, pneumatic total pressure cells of the Slope Indicator Company (Model 51482 with 514178 transducer) are being used. Three of these total pressure cells are placed along the centre line perpendicular to the face of the wall beneath the lateritic soil at distances of 0.5 m, 3 m and 5.5 m, respectively, from the face. The cell is 9-inch in diameter and 0.434 inch thick, made of stainless steel, filled with liquid (ethylene glycol), and is attached to a pneumatic transducer containing a low displacement, flexible diaphragm (of Buta-N rubber). The fluid pressure due to the major stress is converted into pneumatic pressure by force balancing the diaphragm with a continuous controlled nitrogen gas source supplied through two tube configuration from the digital pneumatic pressure indicator mentioned earlier. The cell is placed with its sensitive side down on a levelled sand pad giving sufficient slack in the connecting tubing.

The vertical pressure distribution as observed from the three cells (front, middle and back) during different stages of construction are shown in Figs. 102 and 103. Figure 102 shows the variation of earth pressure with distance from the face of the wall and Fig. 103 shows the variation of earth pressure with time. Up to the laying of the first four layers, only the front was pressurized (about 3 t/m^2) and the middle and the back cells read zero pressure. But from the fifth layer onwards up to the laying of the 9th layer, the peak pressure shifted to the middle (about 3.5 to 4 t/m^2), while the front still read about 3 t/m^2 and the back cell pressure slowly picking up. But at the tenth, eleventh and twelfth layers, the pressure distribution is more or less uniform, but increasing with each additional layer. The trend shifts back at the thirteenth layer when the peak returns to the middle and the front showing greater pressure than the back. The peak pressure at any instant is nowhere near the value of γZ, γ being the unit weight of backfill and Z is the height/thickness of the backfill over the cell.

XIII REFERENCES

Amin, N.U. (1989). "Direct shear and pullout tests on lateritic soil at low pressure," thesis submitted to the Asian Institute of Technology, Bangkok, Thailand in partial fulfillment of the requirements for the degree of Master of Engineering.

Anderson, L.R., Liu, J. and Bay, J.A. (1986). "Experimental evaluation and design recommendations for Syro anchored retaining wall system". Report Submitted to the Syro Steel Company. Utah State University, Logan, Utah.

Anderson, L.R., Sharp, K.D. and Harding, O.T. (1987). "Performance of a 50-foot high welded wire wall." Soil Improvement- A Ten Year Update, pp. 280-308.

Anderson, L.R. and Wong, W.L. (1987). "Monitoring field performance of welded wire walls." Report Submitted to the Hilfiker Company. Utah State University, Logan, Utah.

Bacot, J.M., Iltis, M., Lareal, P., Paumier, T. and Sanglerat, G. (1978). "Study of the soil reinforcement friction coefficient." ASCE Symp. on Earth Reinforcement, Pittsburgh, Pennsylvania.

Baldwin Lima Hamilton Corp. (1988). "SR-4 Load Cells Instruction Bulletin No. 4360". Waltham, Mass.

Bergado, D.T., Bukkanasuta, A. and Balasubramaniam, A.S. (1987). "Laboratory pullout tests using bamboo and polymer geogrids including a case study". Geotextiles and Geomembranes J., Vol. 5, pp. 153-189.

Bergado, D.T., Sampaco, C.L. and Lekhak, B.N. (1988a). "Welded wire reinforced earth (mechanically stabilized) embankments with cohesive backfill on soft clay". First Progress Report Submitted to the U.S. Agency for International Development, Bangkok, Thailand.

Bergado, D.T., Sampaco, C.L., Alfaro, M.C. and Balasubramaniam, A.S. (1988). "Welded wire reinforced earth (mechanically stabilized) embankment with cohesive backfill on soft clay". Second Progress Report Submitted to the U.S. Agency for International Development, Bangkok, Thailand.

Bishop, J.A. and Anderson, L.R. (1979). "Performance of a welded wire retaining wall." Report Submitted to the Hilfiker Pipe Co. Utah State University, Logan, Utah.

Bourne, K.W. (1989). "Pullout resistance of swiggle tails," thesis submitted to the Utah State University, Logan, Utah in partial fulfillment of the requirements for the degree of Master of Science.

Campbell Scientific, Inc. (1989). "AM416 Relay Multiplexer-Instruction Manual". Campbell Scientific, Inc., Logan, Utah.

Chang, J.C., Hannon, J.B. and Forsyth, R.A. (1977). "Pull resistance and interaction of earthwork reinforcement and soil. Transportation Research Board, 56th Annual Meeting.

Cisneros, C.B. (1989). "Pullout resistance of steel grids with weathered clay as backfill material," thesis submitted to the Asian Institute of Technology, Bangkok, Thailand in partial fulfillment of the requirements for the degree of Master of Engineering.

Dunn, I.S., Anderson, L.R. and Kiefer, F.W. (1980). "Fundamentals of Geotechnical Analysis." John Wiley and Sons, New York.

Hannon, J.B. and Forsyth, R.A. (1984). "Performance of an earthwork reinforcement system constructed with low quality backfill." Trans. Res. Rec. 965.

Hilfiker-Texas Corp. (1988). "Welded wire wall construction guide." Hilfiker Company, Eureka, California.

Ingold, T.S. (1983). "Laboratory pullout testing of grid reinforcement in clay." Geotechnical Testing Journal, Vol. 6, No. 3, pp. 112-119.

Jewell, R.A. (1980). "Some effects of reinforcements on soils." thesis submitted to the Cambridge University, England in partial fulfillment of the requirements for the degree of Doctor of Philosophy.

Jewell, R.A., Milligan, G.W.A., Sarsby, R.W. and Dubois, D. (1984). "Interaction between soil and geogrids." Proc. Symp. on Polymer Grid Reinforcement. Thomas Telford Ltd., London.

McKittrick, D.P. (1979). "Reinforced earth: Application of theory and research to practice." Reinforced Earth Company Technical Series, Report 79-1.

Micro-Measurements, Inc. (1988). "Strain Gages Information Catalog." Measurements Group, Inc., Raleigh, North Carolina.

Mitchell, J.K. and Villet, W.C.B. (1987). "Reinforcement of earth slopes and embankments." Transportation Research Board Report No. 290, Washington, D.C.

NAVFAC DM-7 (1971). "Department of Navy, Naval Facilities Engineering Command, Washington, D.C.

Nelson, K.J. and Selvage, J.R. (1987). "Design applications of the welded wire wall." Proc. 23rd Symp. on Eng'g. Geology and Soil Eng'g., Utah State University, Logan, Utah.

Nielsen, M.R. and Anderson, L.R. (1984). "Pullout resistance of wire mats embedded in soil." Report Submitted to the Hilfiker Co., Utah State University, Logan, Utah.

Ochiai, H. and Sakai, A. (1987). "Analytical method for geogrid-reinforced soil structures." Proc. 8th Asian Regional Conference, Tokyo, Japan, pp. 483-486.

Peterson, L.M and Anderson, L.R. (1980). "Pullout resistance of welded wire mats embedded in soil." Utah State University, Logan, Utah.

Potyondy, J.G. (1961). "Skin friction between cohesive granular and construction materials." Geotechnique, Vol. 11, No. 4, pp. 339-353.

Prandtl, L. (1921). "Uber dre eindringungsfestigkeit platisher baustoffe und die festigkeit von schneiden." Zeitschrift Fur Angewandte Mathematik und Mechanik, Vol. 1, No. 1, pp. 15-20.

Reissner, H. (1924). "Zum erddruckproblem." Proc. Ist Intl. Conf. App. Mech., Delft, pp. 295-311.

Rowe, R.K. and Davis, E.H. (1982). "The behaviour of anchor plates in sand." Geotechnique, Vol. 32, No. 1, pp. 25-41.

Schlosser, F. and Elias, V. (1978). "Friction in reinforced earth." ASCE Symp. on Earth Reinforcement, Pittsburgh, Pennsylvania.

Skempton, A.W. (1951). "The bearing capacity of clays." Building Research Congress, England.

Vesic, A.B. (1963). "Bearing capacity of deep foundations in sand." Highway Research Record No. 39, National Research Council, Washington, D.C.

Vickers, Co. (1988). "Information Catalog No. 400." The Rains Company, Salt Lake City, Utah.

Yokota, H., Nakazawa, T. and Fujimoto, H. (1988). "The earth reinforcement effects of steel bar truss in embankment." Proc. Intl. Geotech. Symp. on Theory and Practice of Earth Reinforcement, Fukuoka, Japan.

TABLES and FIGURES

Table 1 Tension Test Results for 3/8" Diameter Round Bar

Force (kg)	Stress (kg/cm^2)	Strain x 10^{-6}	Stress (MPa)
0	0.000	0.0	0.000
50	78.616	63.0	7.712
200	314.465	166.0	30.849
400	628.931	383.0	61.698
500	786.164	395.0	77.123
540	849.057	416.0	83.292
600	943.396	499.0	92.547
800	1257.862	654.0	123.396
1000	1572.327	804.5	154.245
1200	1886.792	962.0	185.094
1400	2201.258	1116.5	215.943
1600	2515.723	1264.5	246.792
1800	2830.189	1415.5	277.642
2000	3144.654	1569.0	308.491
2200	3459.119	1722.0	339.340
2400	3773.585	1889.5	370.189
2600	4088.050	25279.0 *	401.038
2700	4245.283	27000.0 *	416.462
3000	4716.981	28000.0 *	462.736
3300	5188.679	29000.0 *	509.009
3000	4716.981	32000.0 *	462.736
2400	3773.585	33000.0 *	370.189

* inaccurate values

Table 2 Tension Test Results for 1/4" Diameter Round Bar

Force (kg)	Stress (kg/cm^2)	Strain ($\times 10^{-6}$)	Stress (Mpa)
0	0.000	0.0	0.000
60	212.239	40.0	20.821
100	353.732	163.0	34.701
200	707.464	305.5	69.402
300	1061.196	475.0	104.103
400	1414.927	633.5	138.804
500	1768.659	796.0	173.505
600	2122.391	957.0	208.207
700	2476.123	1123.5	242.908
800	2829.855	1286.0	277.609
900	3183.587	1457.0	312.310
1000	3537.319	1627.0	347.011
1100	3891.051	1787.5	381.712
1140	4032.543	3797.0	395.593
1200	4244.782	3808.0	416.413
1300	4598.514	4000.0	451.114
1385	4899.136	4100.0	480.610
1250	4421.648	4300.0	433.764
1000	3537.319	4800.0	347.011

Table 3 Direct Shear Test Results on Backfill Materials

Properties	WEATHERED CLAY	CLAYEY SAND	LATERITIC RESIDUAL SOIL
a). Cohesion, c (t/m^2)			
85% Compaction	9.0	3.6	2.5
90% Compaction	12.0	3.7	2.6
95% Compaction	12.9	3.8	8.8
b). Angle of friction, o (degree)			
85% Compaction	29.1	25.8	38.0
90% Compaction	29.7	26.2	39.7
95% Compaction	30.7	26.8	40.2

Table 4 CIU Triaxial Test Results on Backfill Materials

Sample	Eff. Cons. Press. t/m^2	Water Content, %	Dry Unit Weight, t/m^3	Effective		Total	
				$\bar{\phi}$, degree	$\bar{c}$, t/m^2	ϕ, degree	c, t/m^2
WEATHERED CLAY (85%)	5 10 20	21.18	1.38	19.8	1.5	13.8	0.7
WEATHERED CLAY (90%)	5 10 20	21.50	1.47	20.4	1.6	14.0	1.1
WEATHERED CLAY (95%)	5 10 20	21.12	1.55	25.8	1.9	15.5	2.4
CLAYEY SAND (85%)	5 10 20	13.40	1.52	21.6	0.7	16.8	1.0
CLAYEY SAND (90%)	5 10 20	13.40	1.62	23.6	1.2	17.1	1.9
CLAYEY SAND (95%)	5 10 20	13.40	1.70	24.0	2.5	18.2	3.2
LATERITIC RESIDUAL SOIL (85%)	5 10 20	10.88	1.64	21.3	0.0	15.3	1.1
LATERITIC RESIDUAL SOIL (90%)	5 10 20	10.77	1.74	22.[illegible]	2.3	19.0	2.4
LATERITIC RESIDUAL SOIL (95%)	5 10 20	10.77	1.83	25.2	2.7	21.0	3.0

Table 5 UU Triaxial Test Results on Backfill Materials

Sample	Cell Pressure, t/m^2	Water Content, %	Dry Unit Weight, t/m^3	ϕ, degrees	c, t/m^2
WEATHERED CLAY (85%)	5 10 20	21.21	1.38	28.2	7.3
WEATHERED CLAY (90%)	5 10 20	21.40	1.47	29.1	8.8
WEATHERED CLAY (95%)	5 10 20	21.34	1.55	31.5	11.8
CLAYEY SAND (85%)	5 10 20	13.50	1.52	17.3	2.4
CLAYEY SAND (90%)	5 10 20	13.50	1.61	20.2	2.7
CLAYEY SAND (95%)	5 10 20	13.20	1.70	23.5	4.2
LATERITIC RESIDUAL SOIL (85%)	5 10 20	10.60	1.64	29.2	4.2
LATERITIC RESIDUAL SOIL (90%)	5 10 20	10.33	1.74	31.0	6.6
LATERITIC RESIDUAL SOIL (95%)	5 10 20	10.64	1.83	32.5	8.0

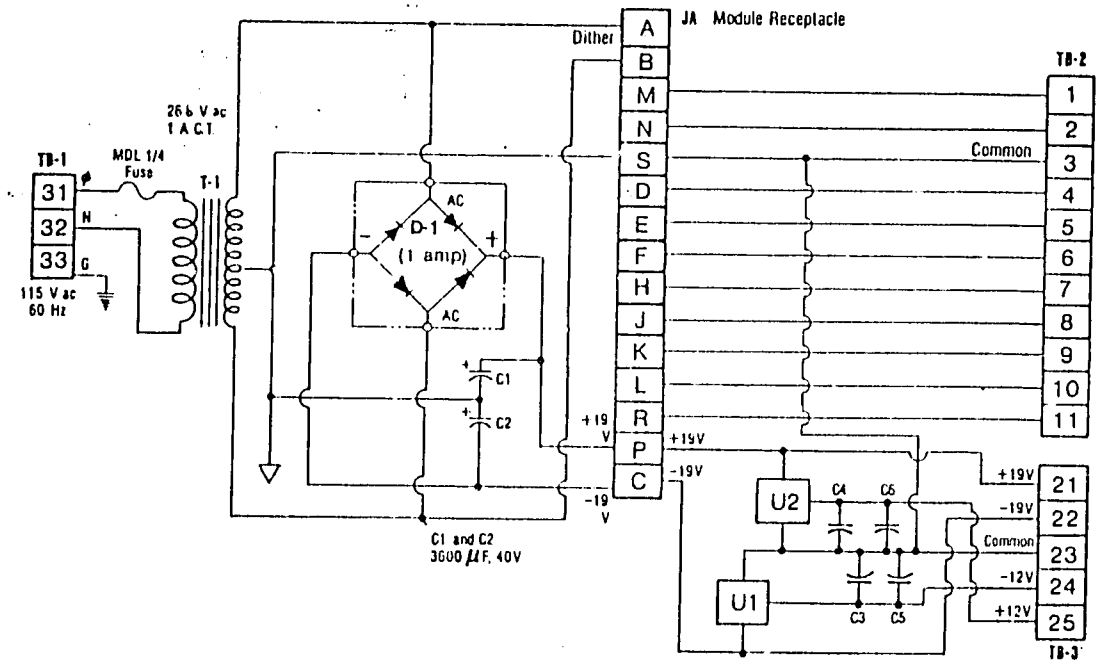

(a)

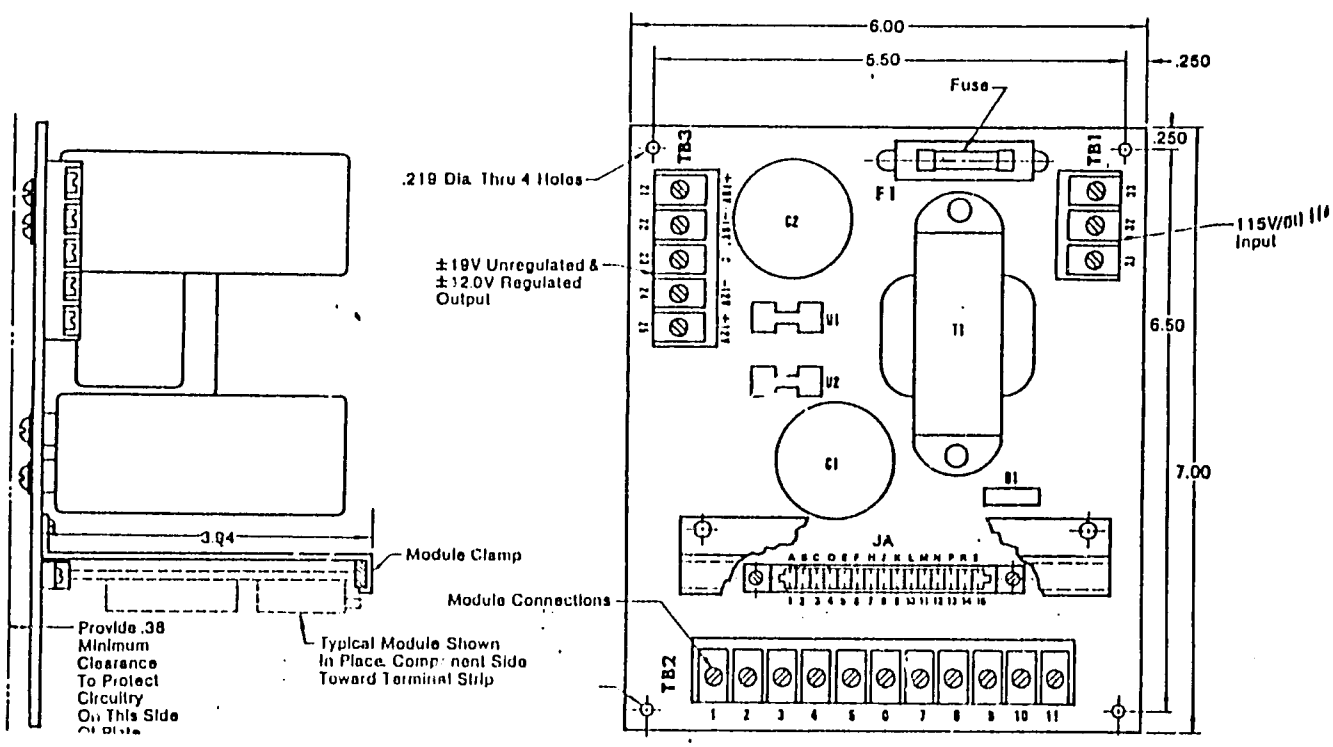

(b)

Fig. 1 a) Circuit Diagram of the EMRS-A-11 Power Supply (after Vickers, 1988)
b) Plan Section of the Power Supply Unit (after Vickers, 1988)

Potentiometer Adjustments

Dither - Adjusts dither output from 0 mA (CCW) to 40 mA RMS (CW).

Bias - Biases the power stage output with no input from −400 mA (CW), through 0 mA (center) to + 400 mA (CCW).

− Limiter - Limits output current in negative direction from 0 mA (CCW) to − maximum output capability (CW).

+ Limiter - Limits output in positive direction from 0 mA (CCW) to + maximum output capability (CW).

Gain 1 - Adjusts gain of power stage from minimum (CCW) to maximum (CW).

Gain 2 - Adjusts gain of voltage amplifier stage from minimum (CCW) to maximum (CW).

Ratio - Adjusts ratio of inputs at terminals 8 and 9. Center is for equal inputs. CW rotation increases 8/9 ratio. CCW rotation decreases 8/9 ratio.

(c)

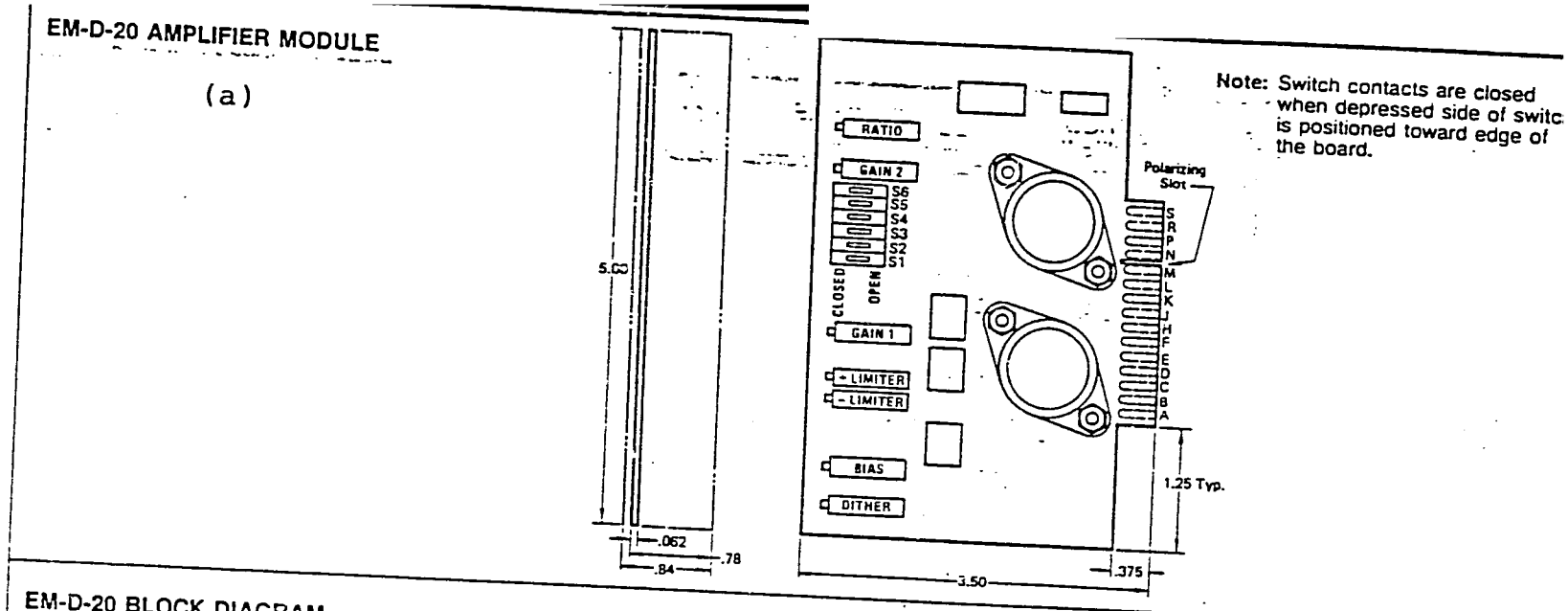

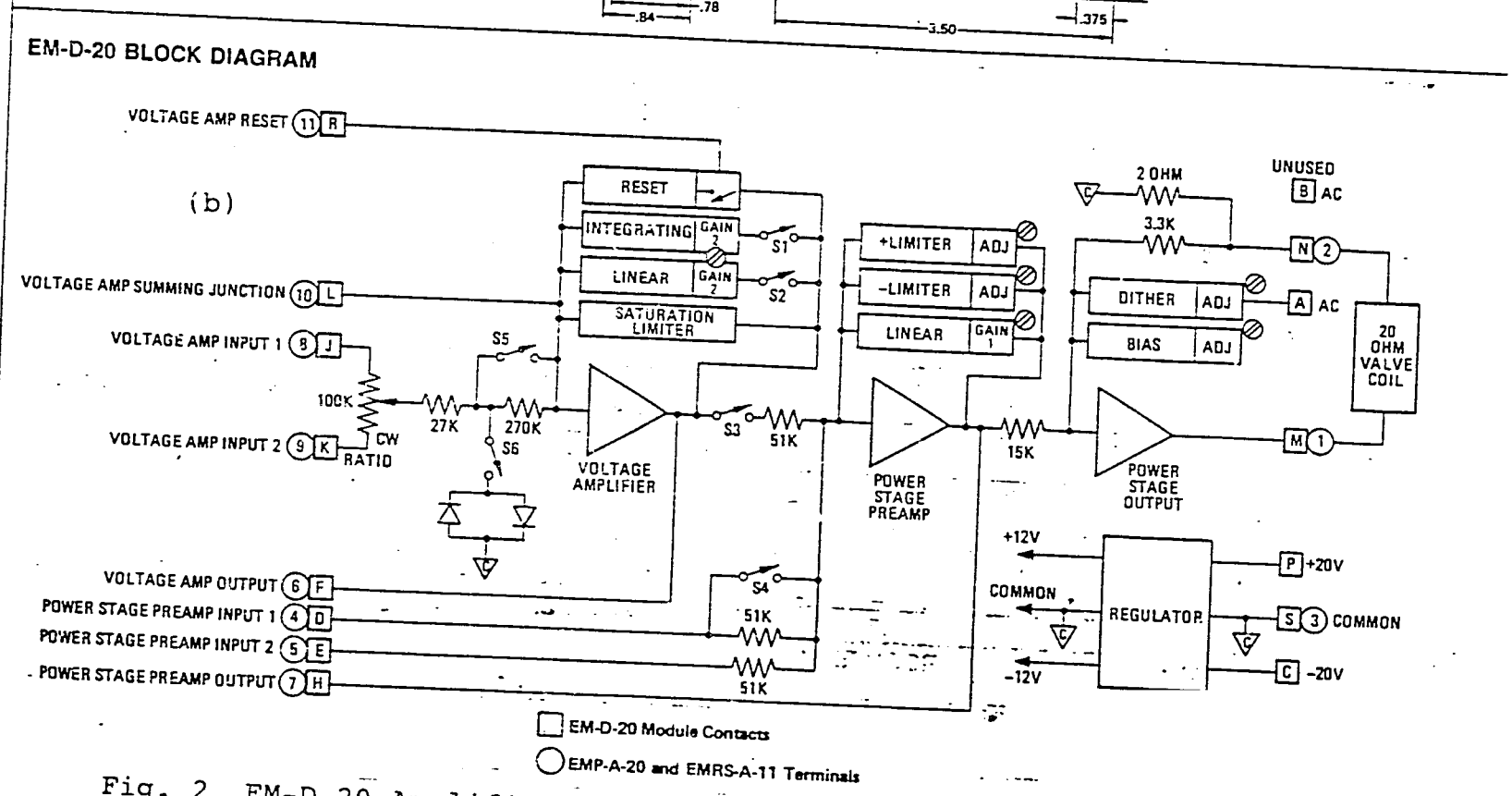

Fig. 2 EM-D-20 Amplifier Module (after Vickers, 1988)
a) Plan Section, b) Block Diagram,
c) Potentiometer Adjustments

I-519720-2

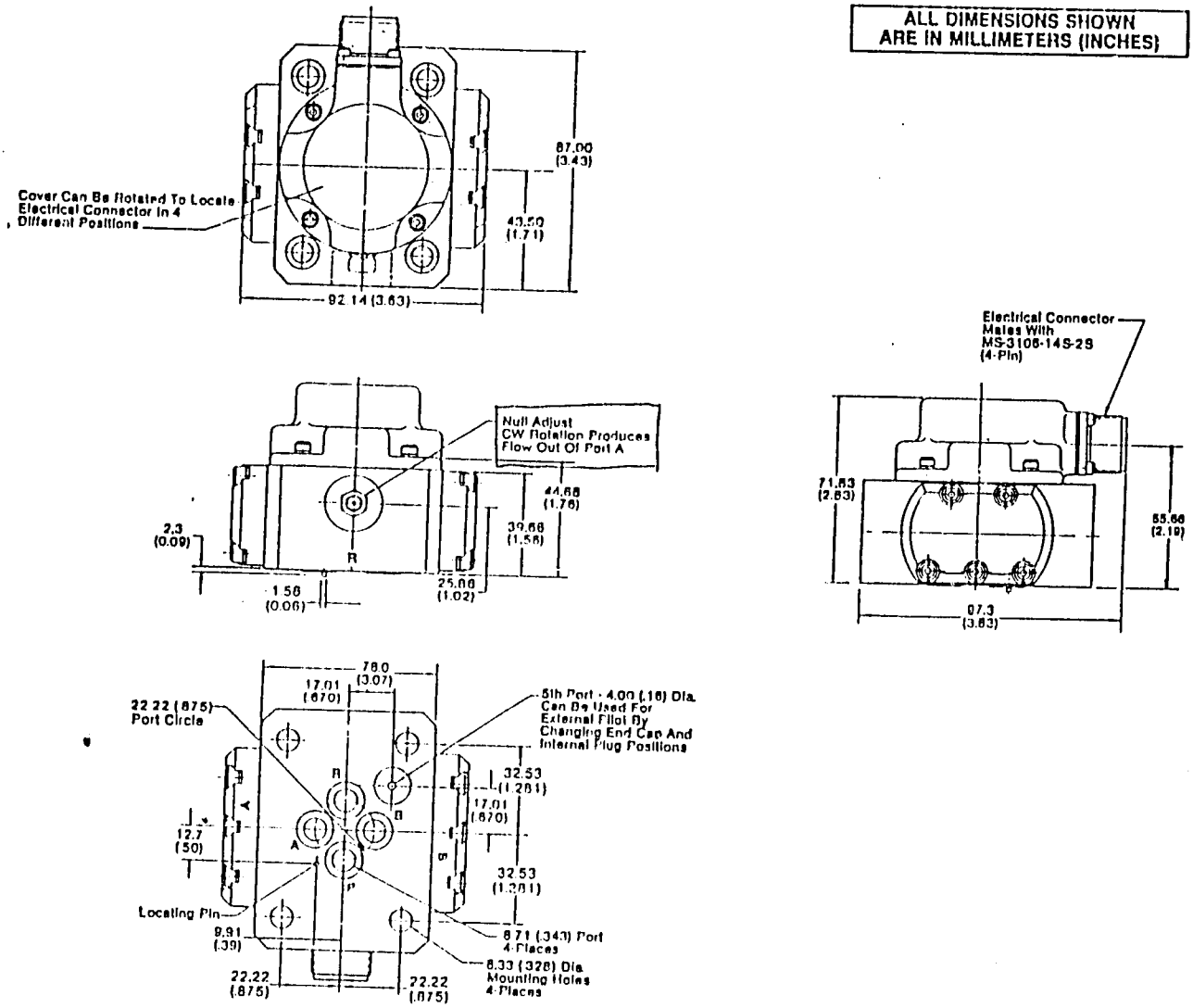

(a)

TYPICAL FLOW/CURRENT RELATIONSHIP

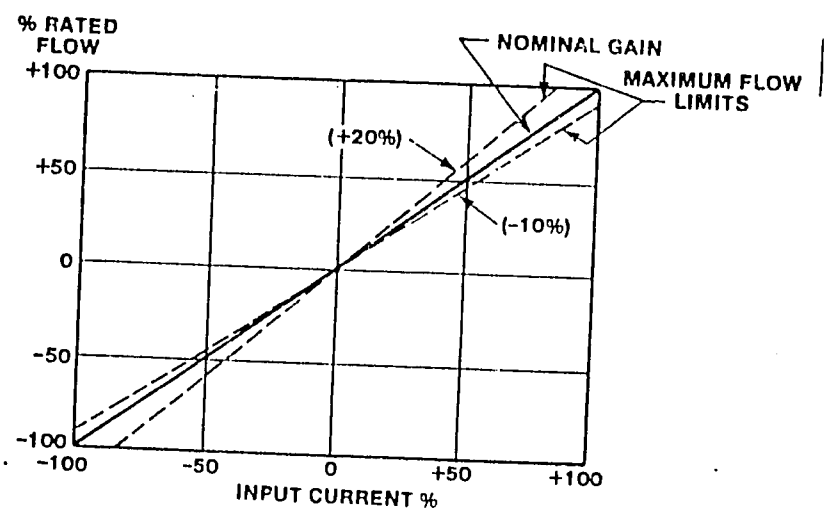

(b)

Fig. 3 Electro-Hydraulic Flopper Nozzle Piloted Servo Valve (after Vickers, 1988)
a) Details of the Valve
b) Typical Flow/Current Relationship

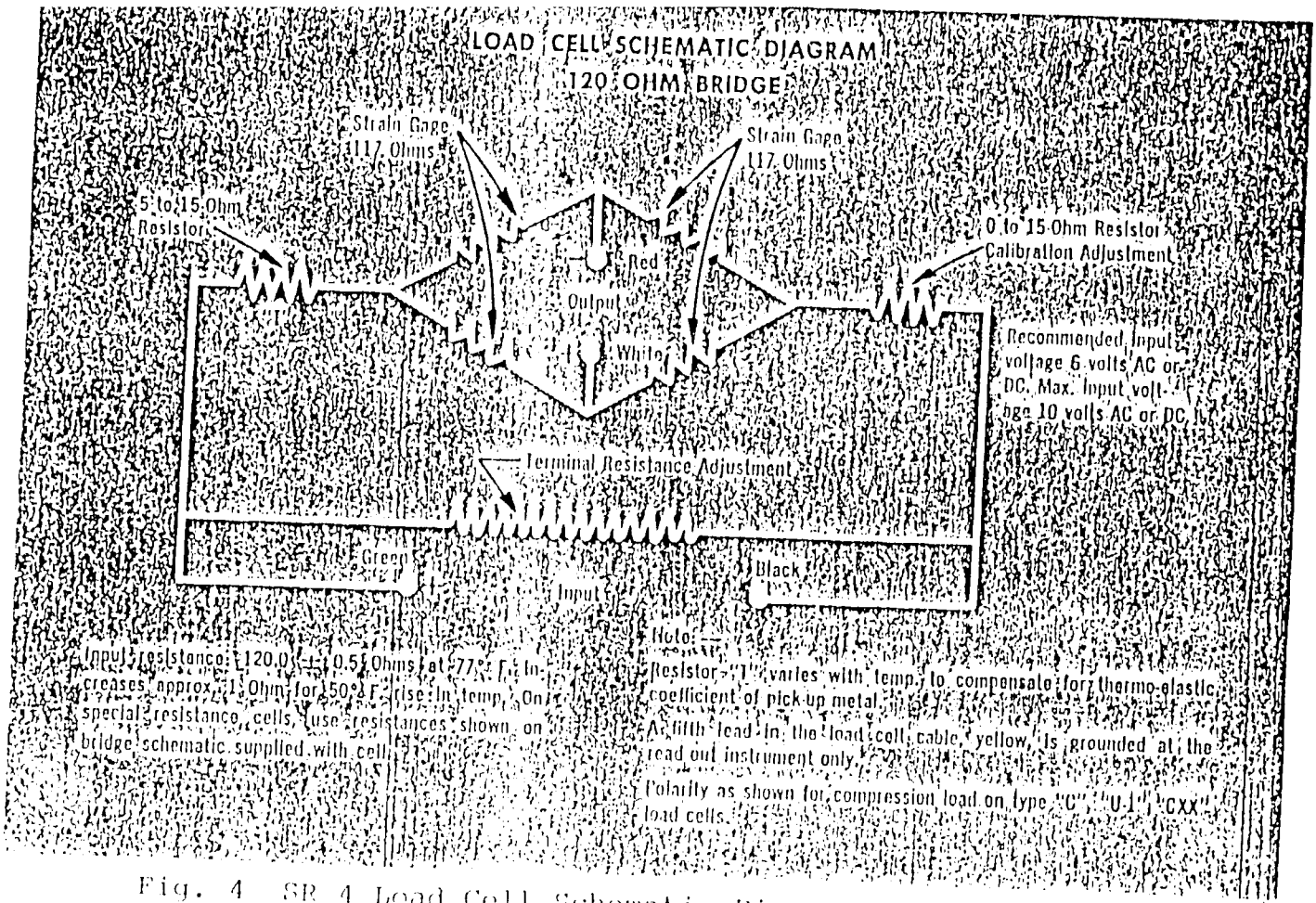

Fig. 4 SR 4 Load Cell Schematic Diagram (after Baldwin Lima Hamilton Corp., 1988)

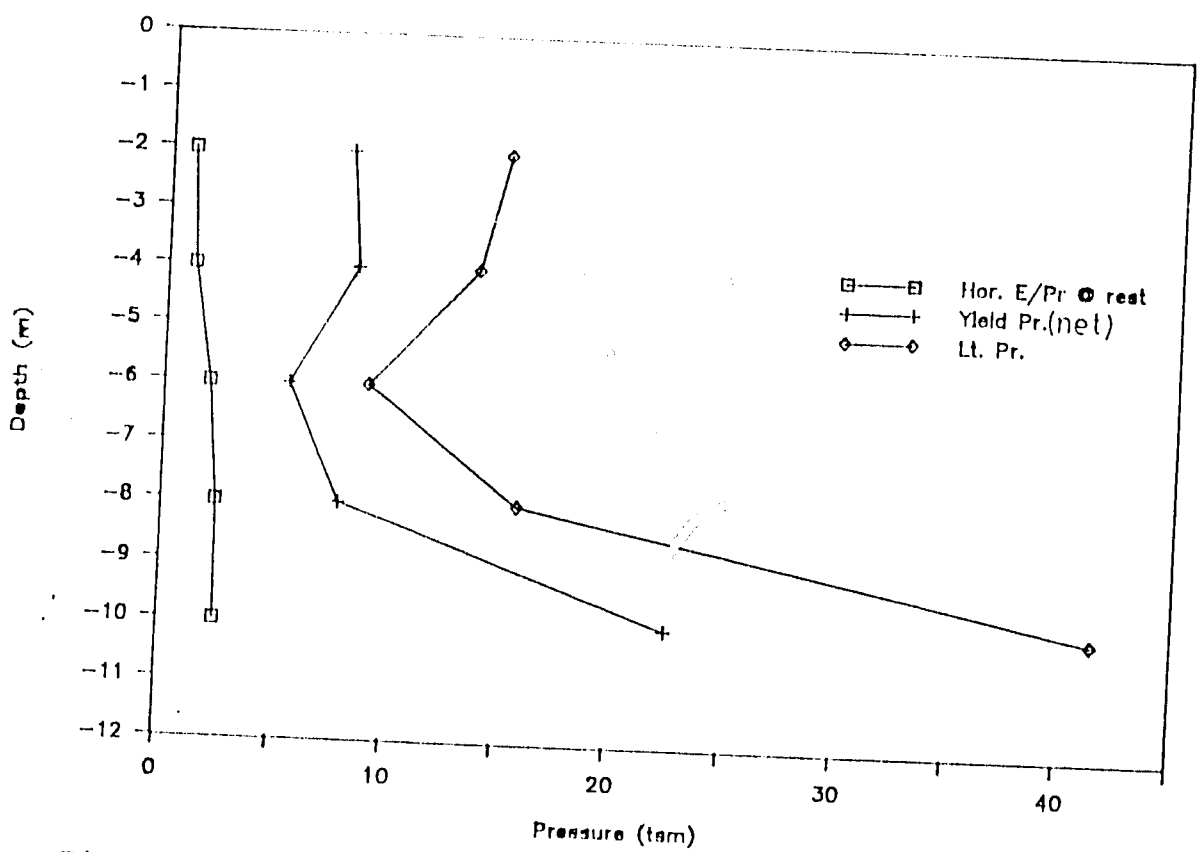

Fig. 5 Variation of the Horizontal Earth Pressure at Rest, Net Yield Pressure and Limiting Pressures with Depth, obtained from Pressuremeter Tests

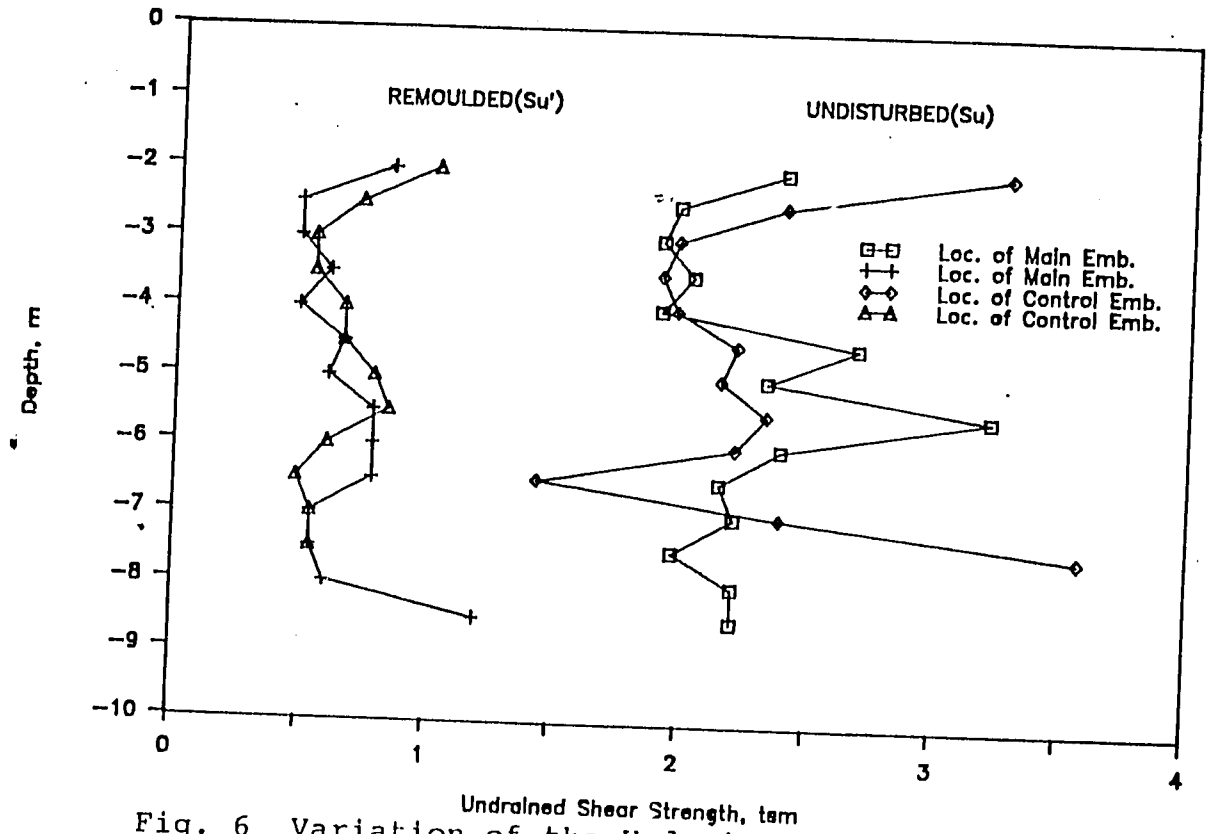

Fig. 6 Variation of the Undrained Shear Strength (Remoulded and Undisturbed) with Depth from Field Vane Shear Test

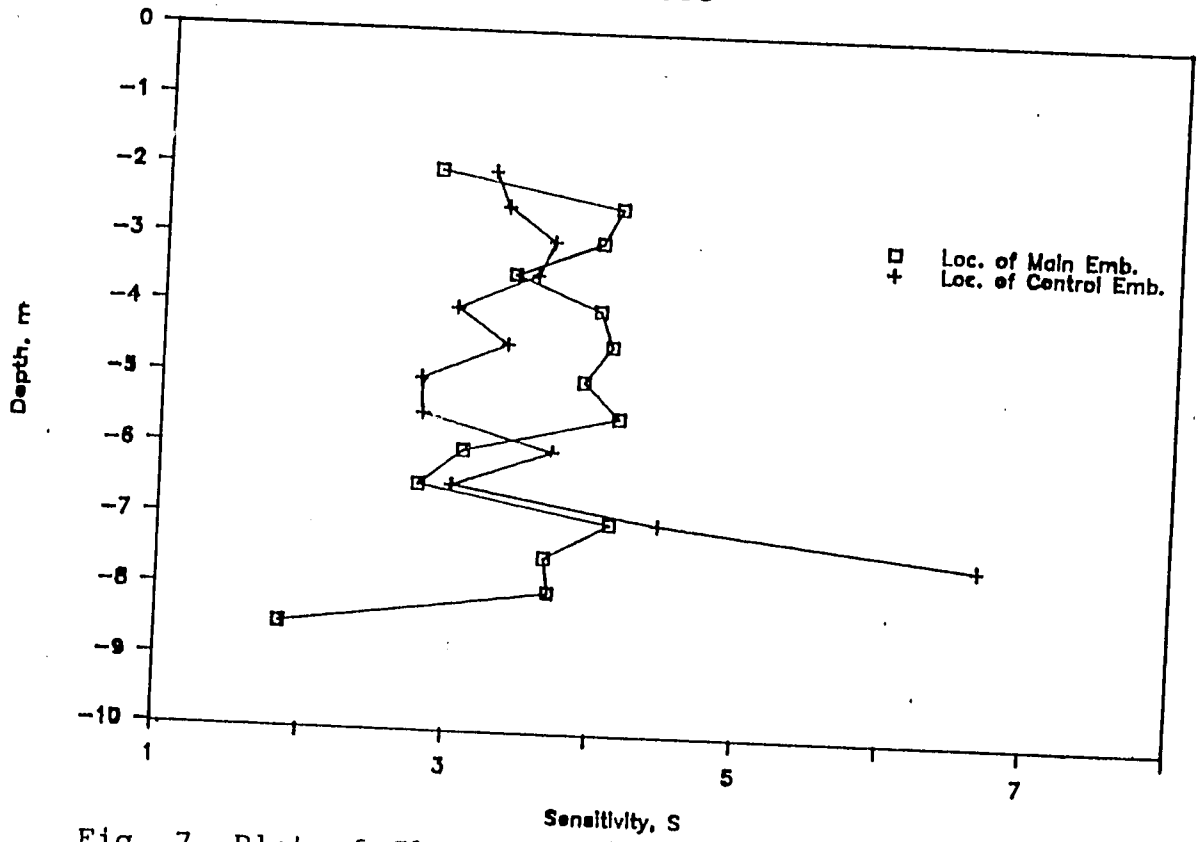

Fig. 7 Plot of Clay Sensitivity with Depth from Field Vane Shear Test

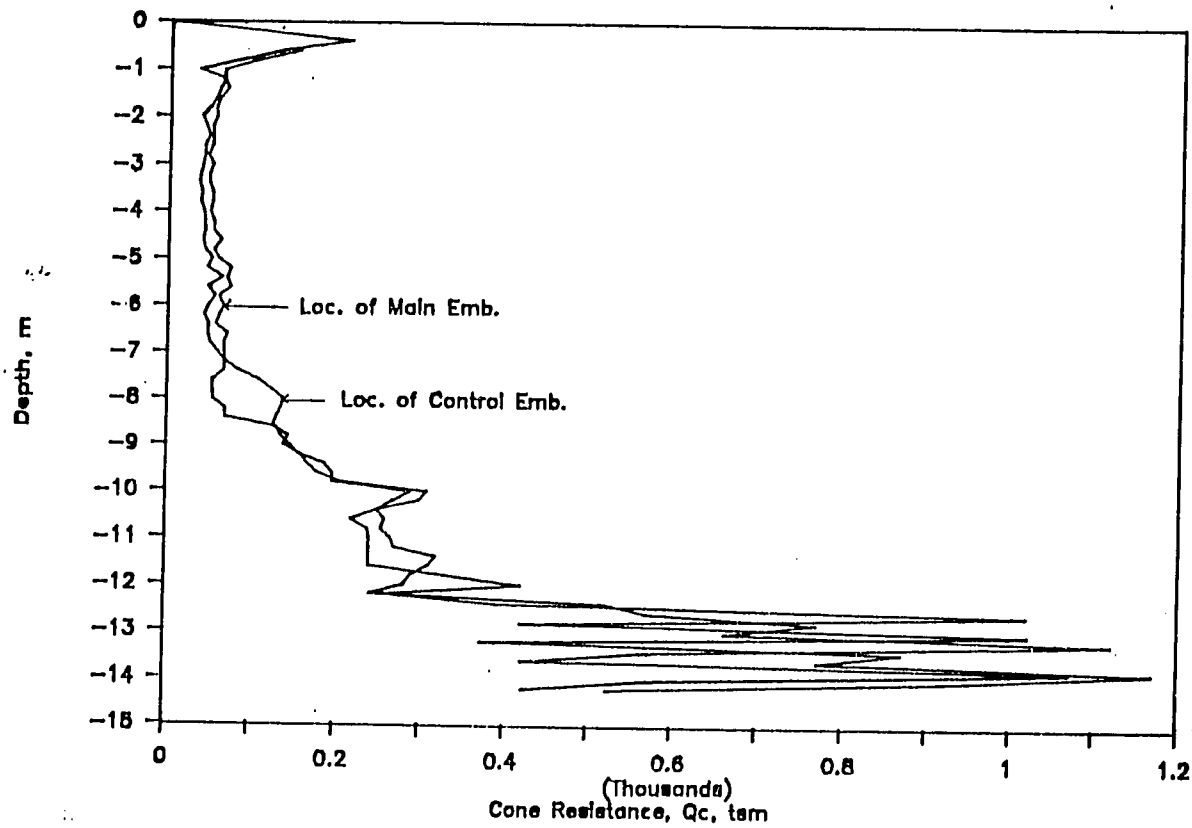

Fig. 8 Variation of the Cone Resistance with Depth from Dutch Cone Test

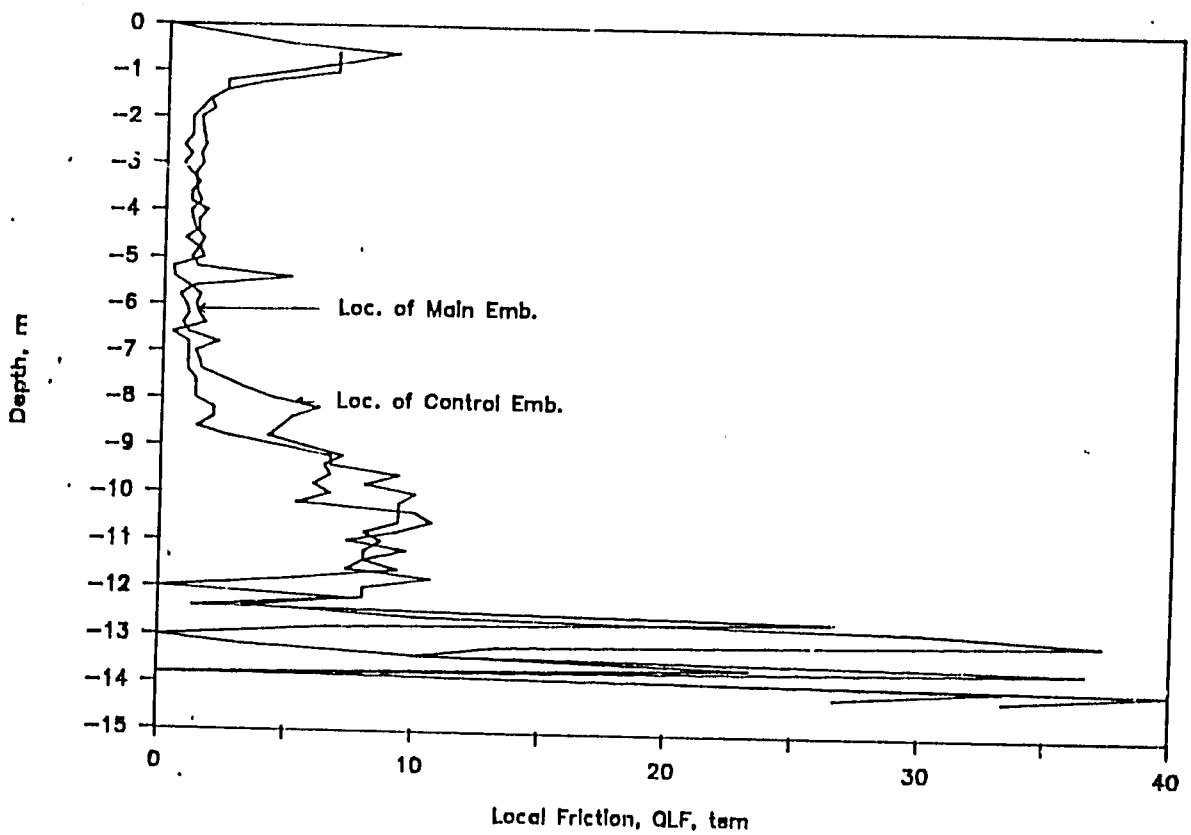

Fig. 9 Variation of Local Friction with Depth from Dutch Cone Test

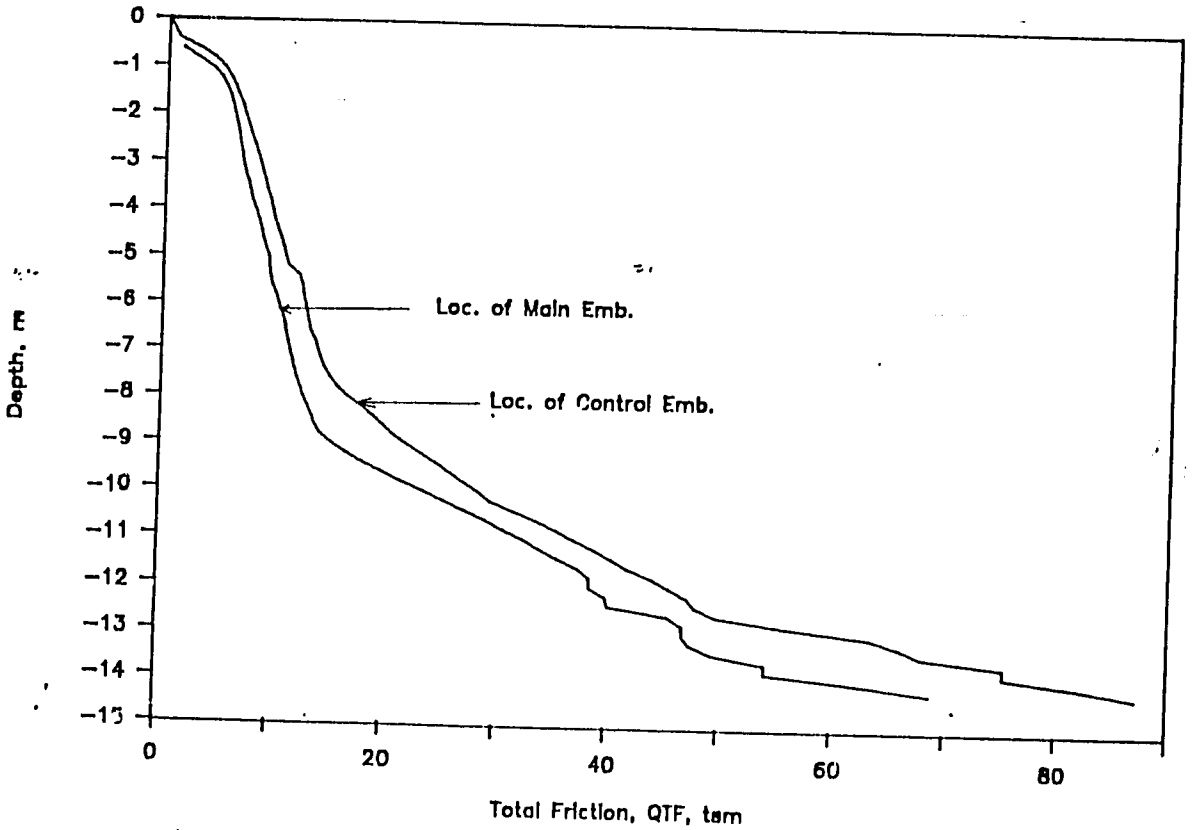

Fig. 10 Plot of Total Friction with Depth obtained from Dutch Cone Test

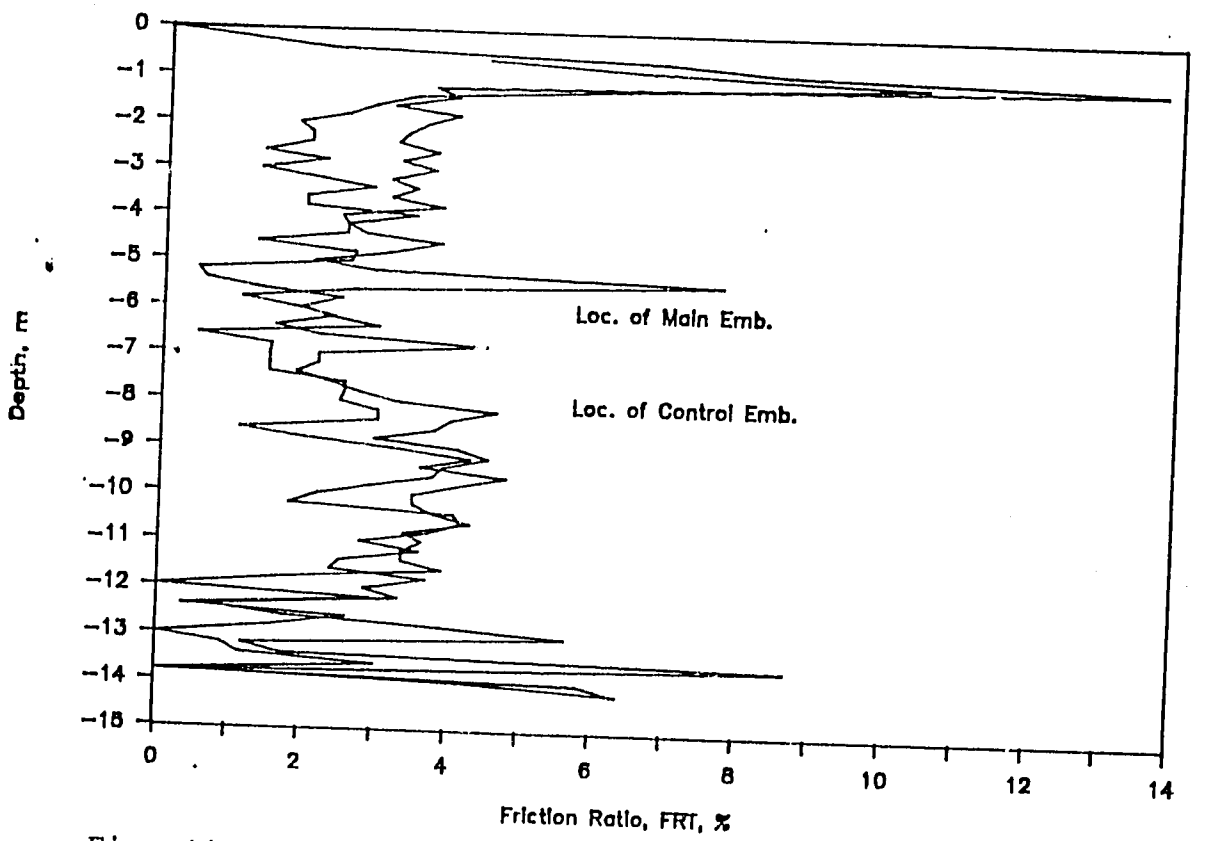

Fig. 11 Plot of Total Friction with Depth from Dutch Cone Test

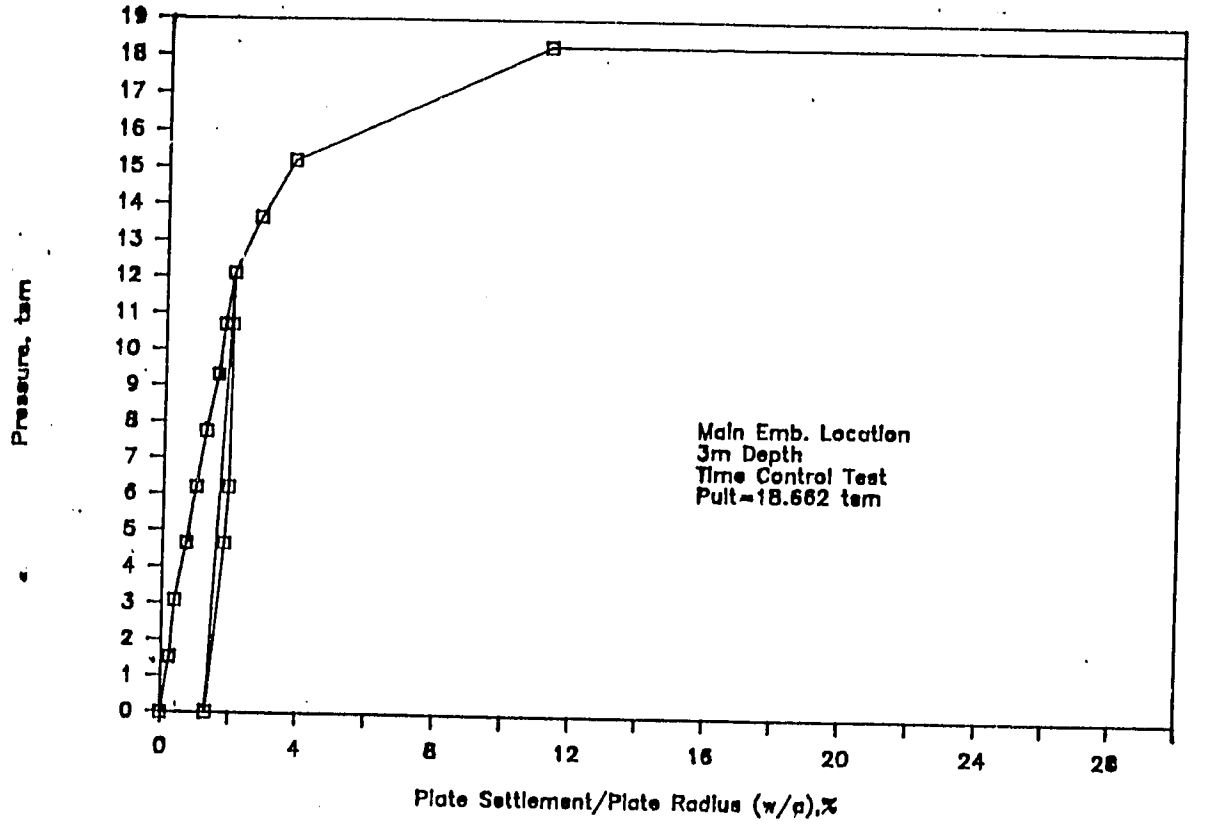

Fig. 12 Screw Plate Load Test Result at 3 m Depth

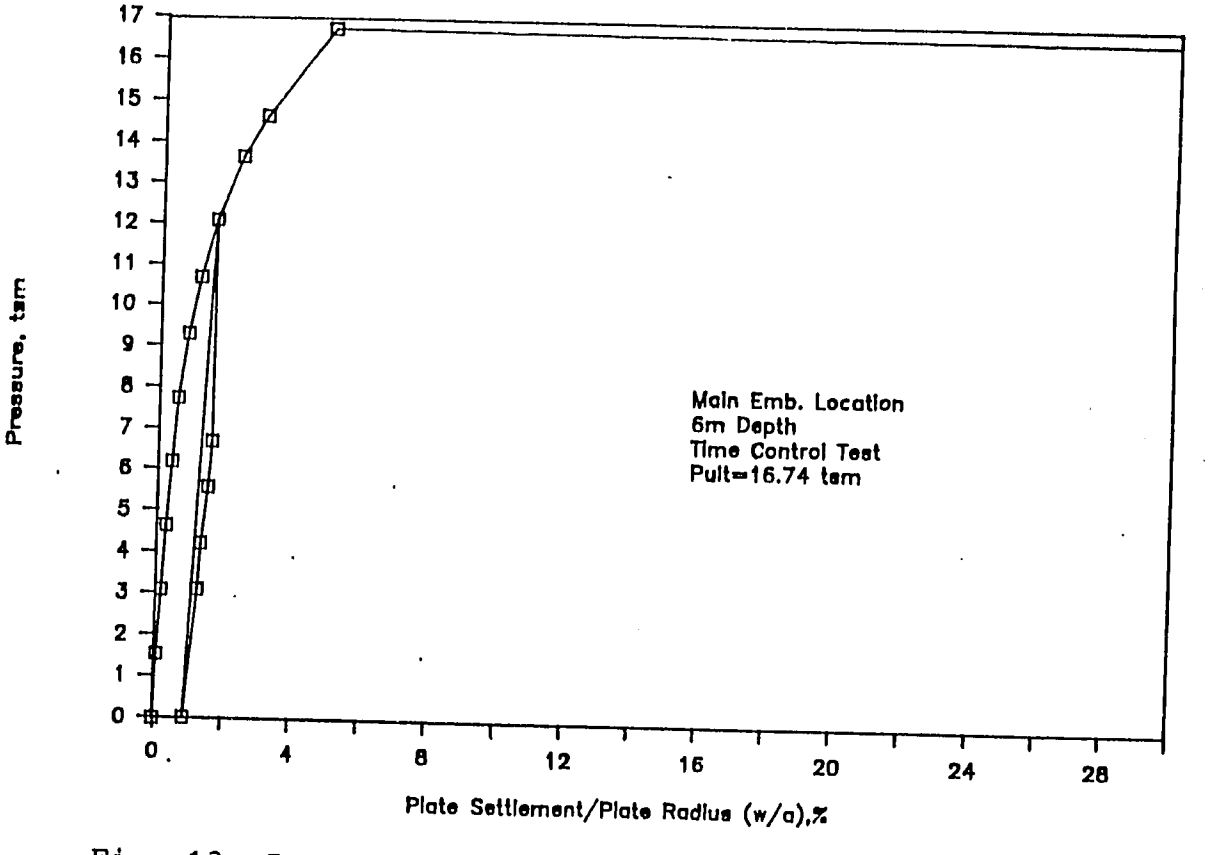

Fig. 13 Screw Plate Load test Result at 6 m Depth

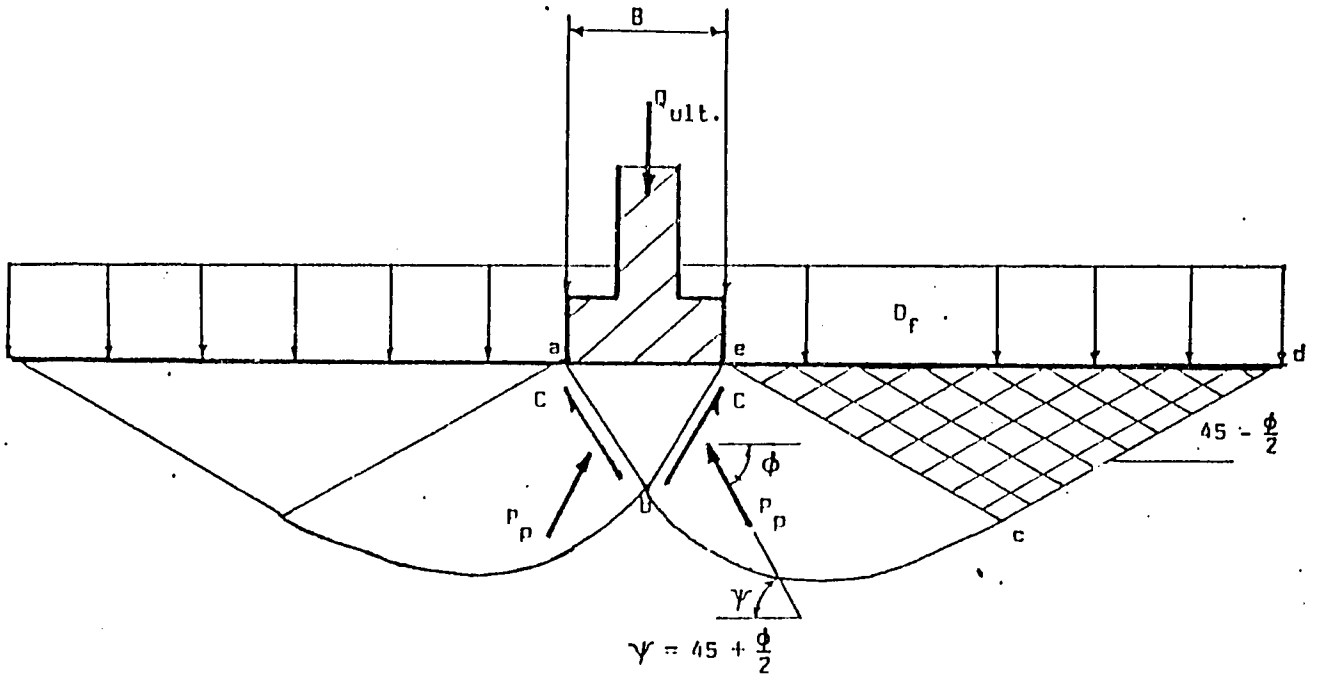

(a)

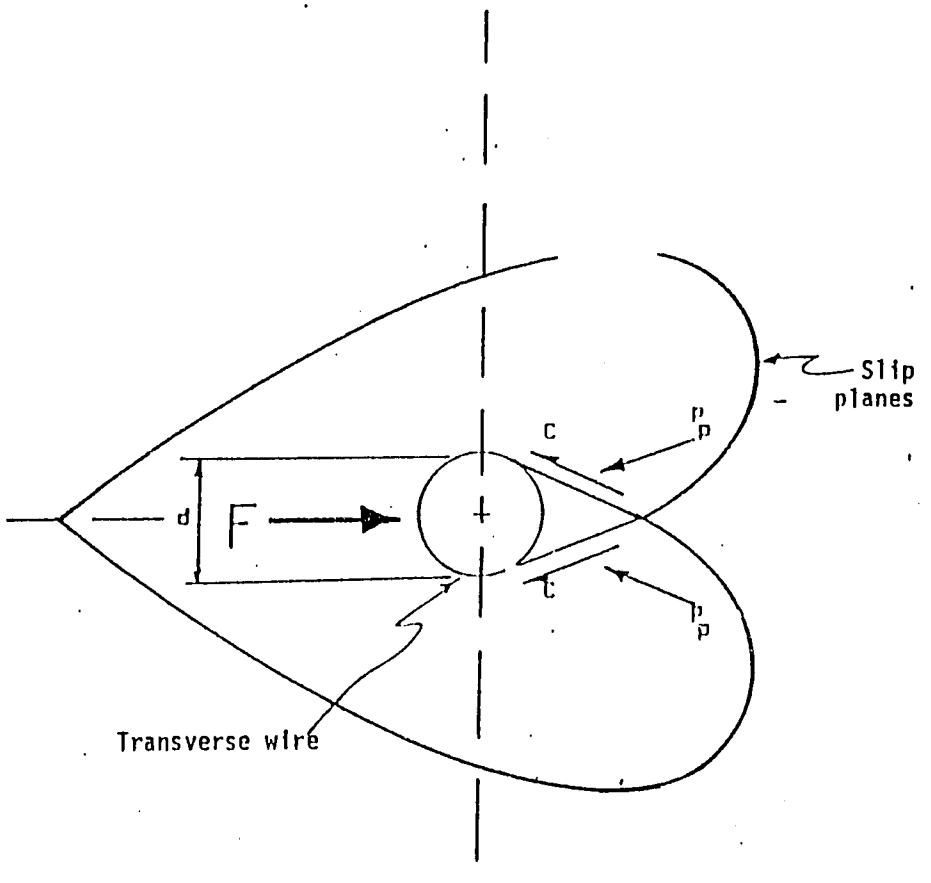

Fig. 14 a) Failure Planes for Strip Footings (Dunn et al, 1980)
b) Suggested Slip Planes for Horizontal Bearing (Peterson and Anderson, 1980)

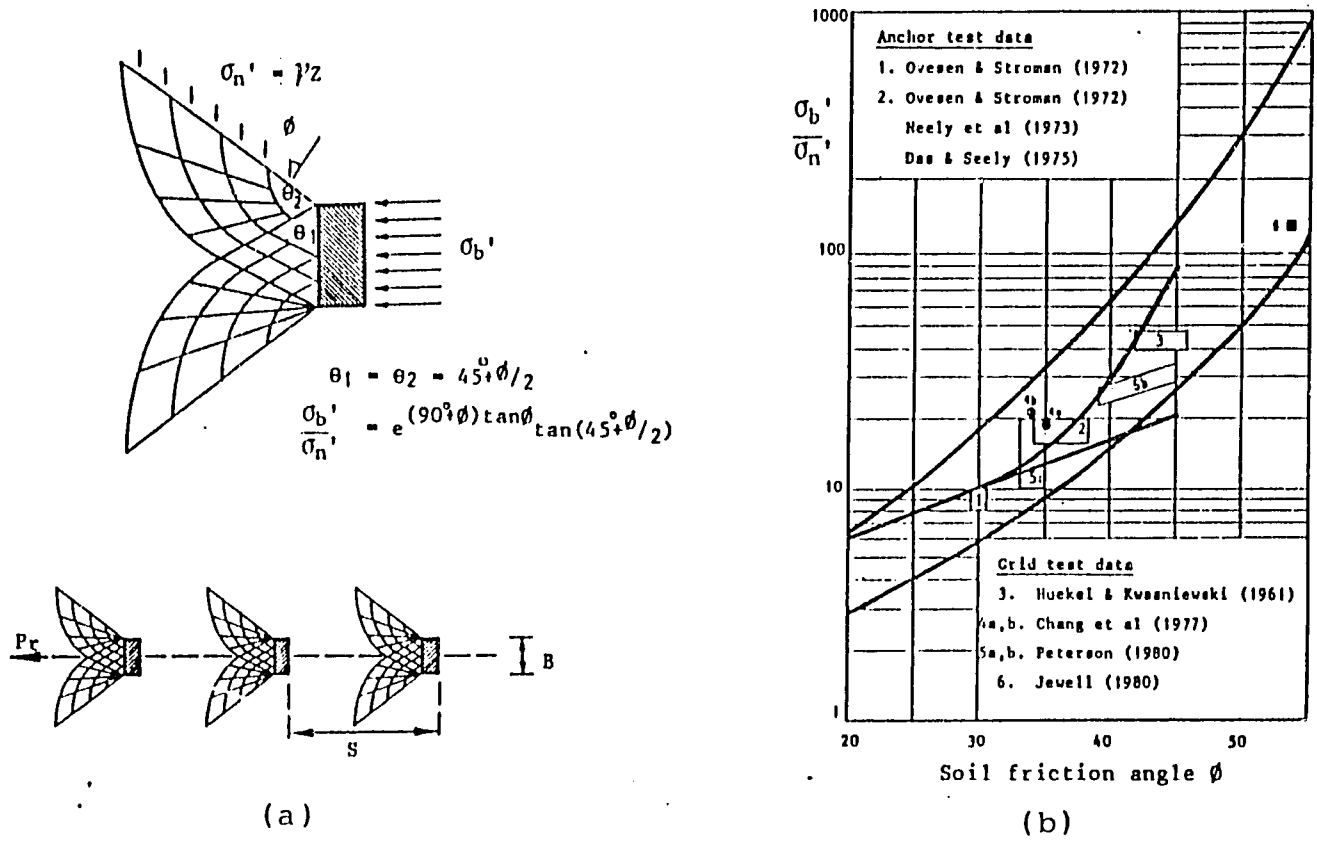

Fig. 15 a) Boundary Conditions for Bearing Stresses on Grid Reinforcement during Punching Shear (Jewell et al, 1984)
b) Comparison of Test Results with Predicted Values of Bearing Stress (Jewell et al, 1984).

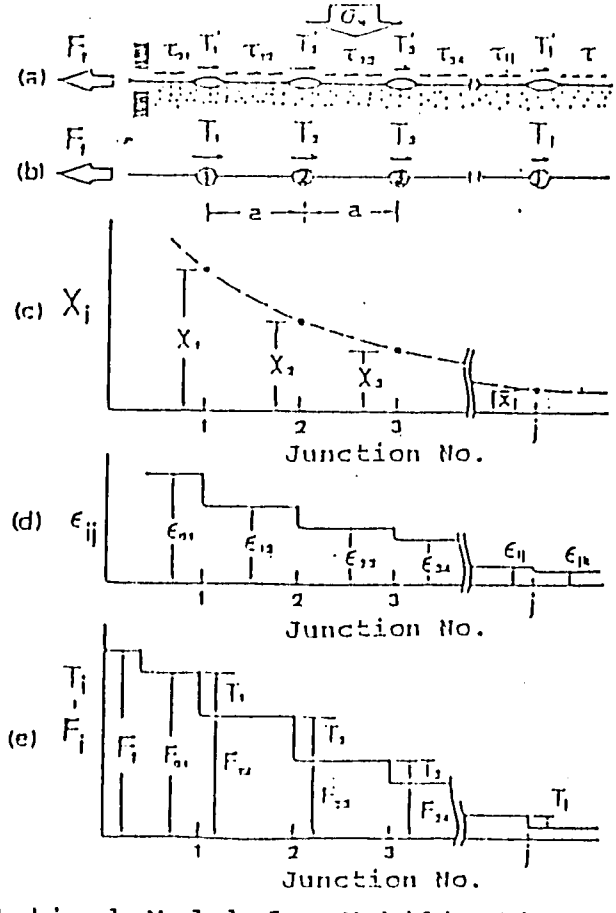

Fig. 16 Analytical Model for Mobilization of Passive Resistance at Grid Junctions (Ochiai et al, 1987)

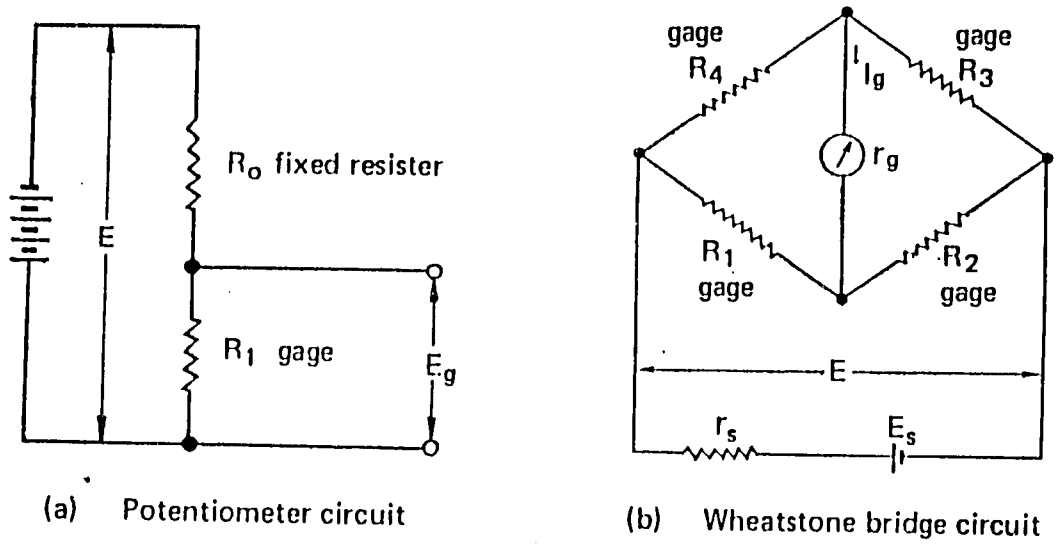

Fig. 17 Resistance Measurement Circuits

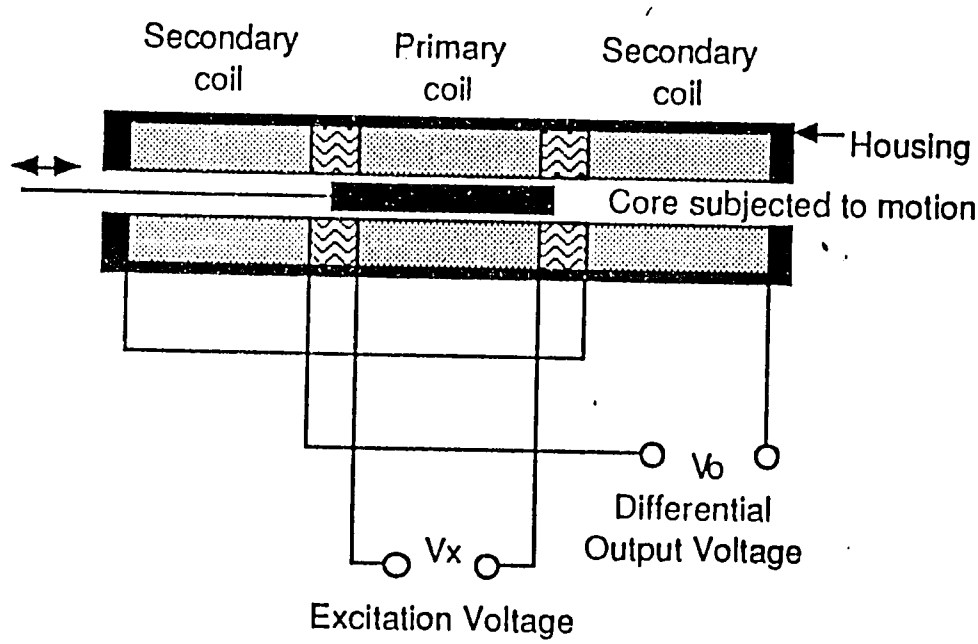

Fig. 18 Schematic of LVDT Showing Excitation Voltage and Differential Output Voltage Location (Bourne, 1989)

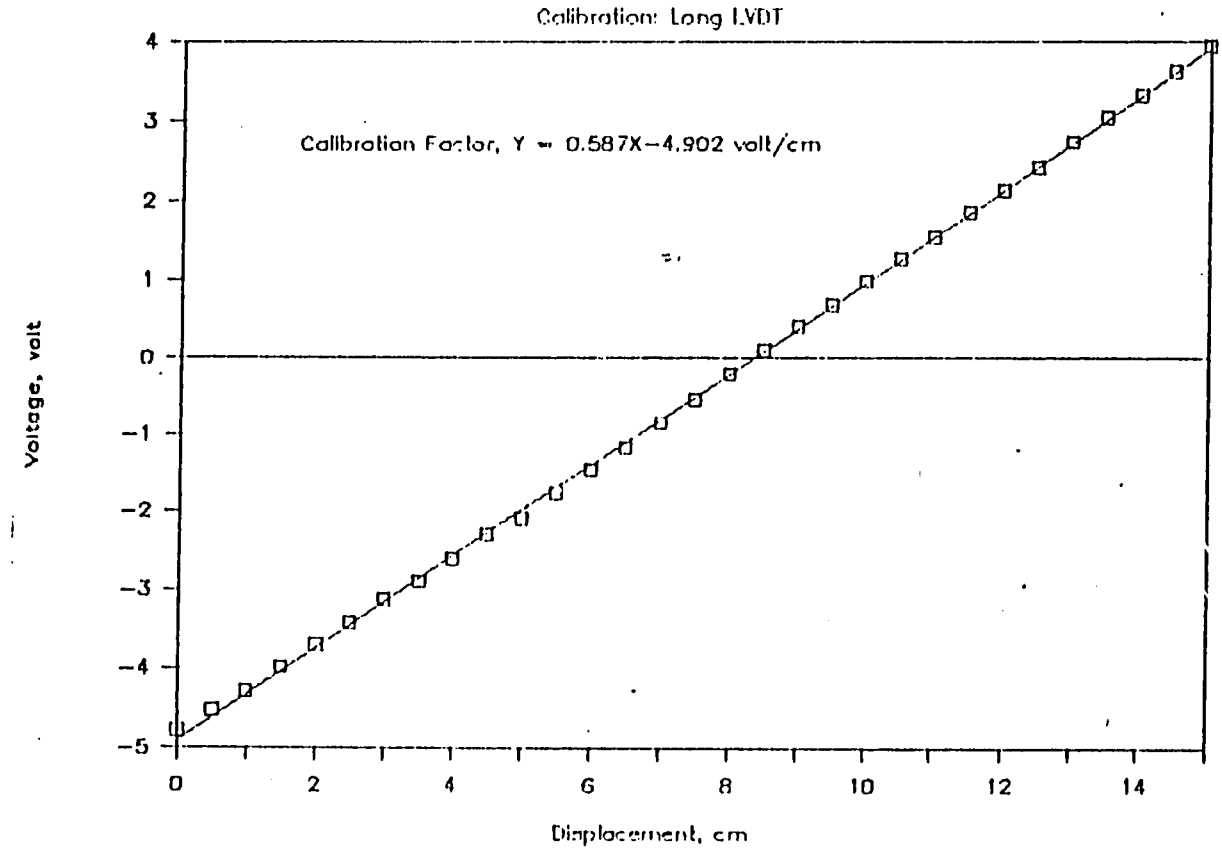

(a)

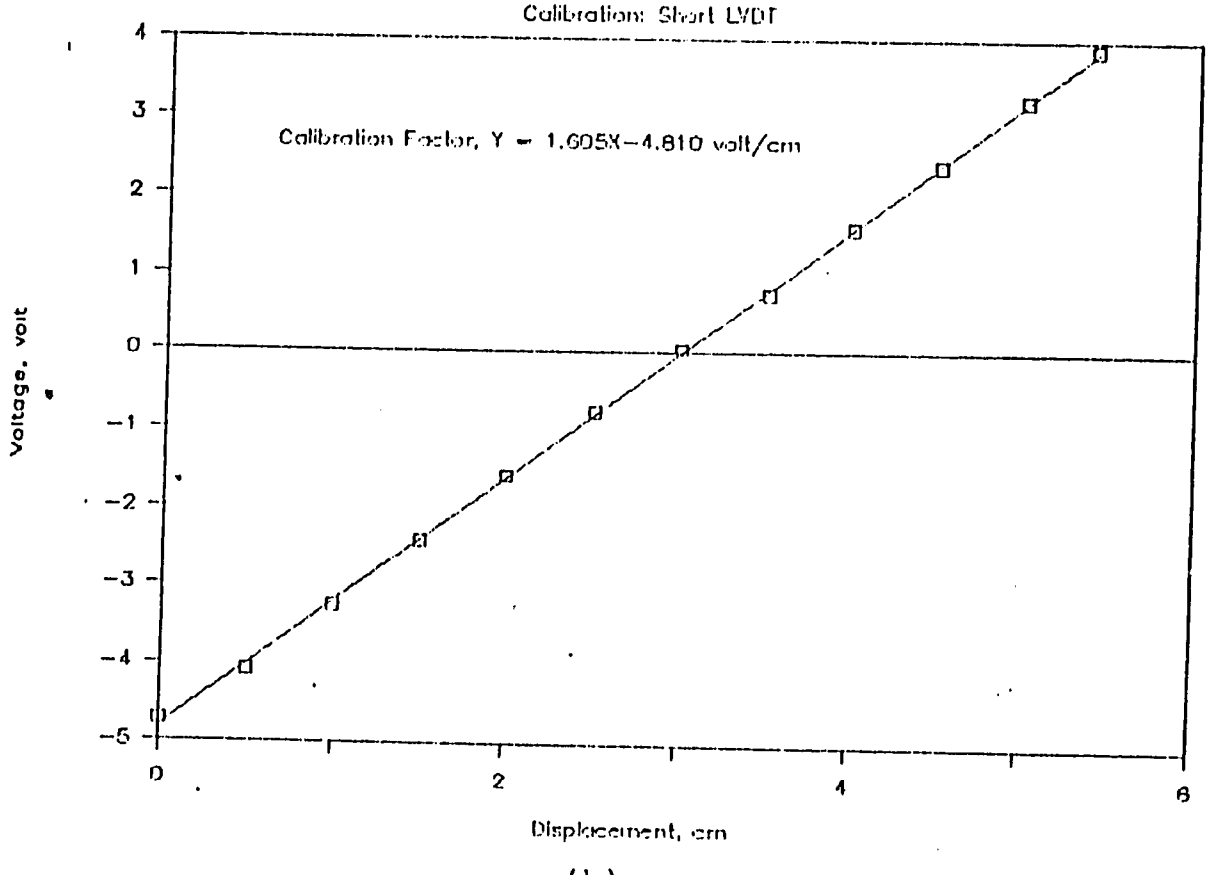

(b)

Fig. 19 a) Calibration Data for Long LVDT
b) Calibration Data for Short LVDT

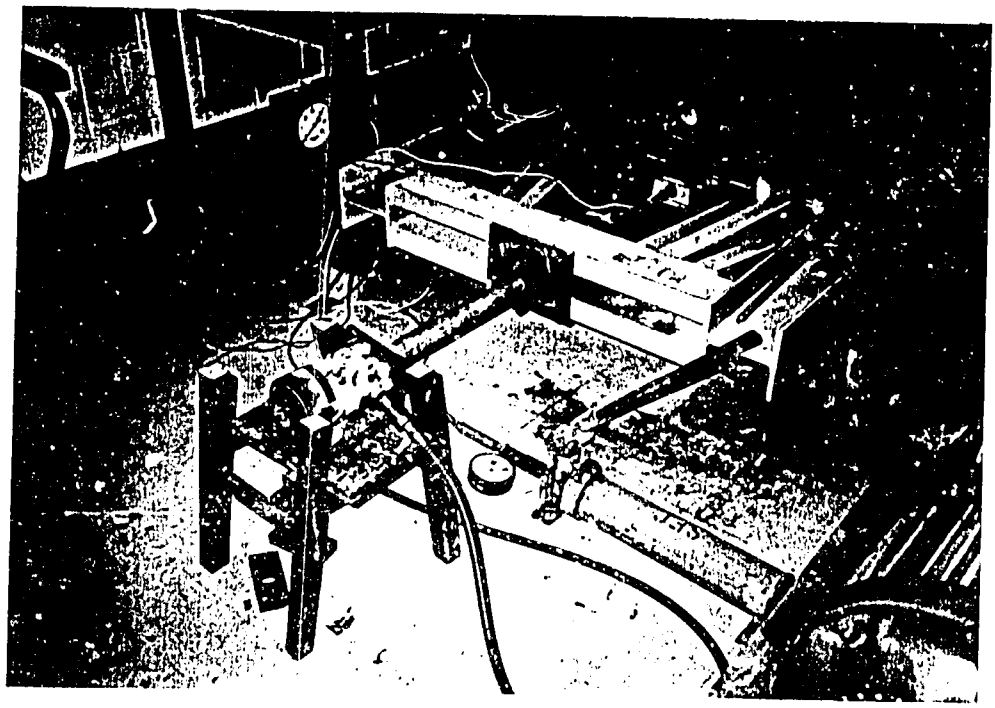

Fig. 20 Photograph Showing the Set-Up of the Hydraulic Pullout Jack

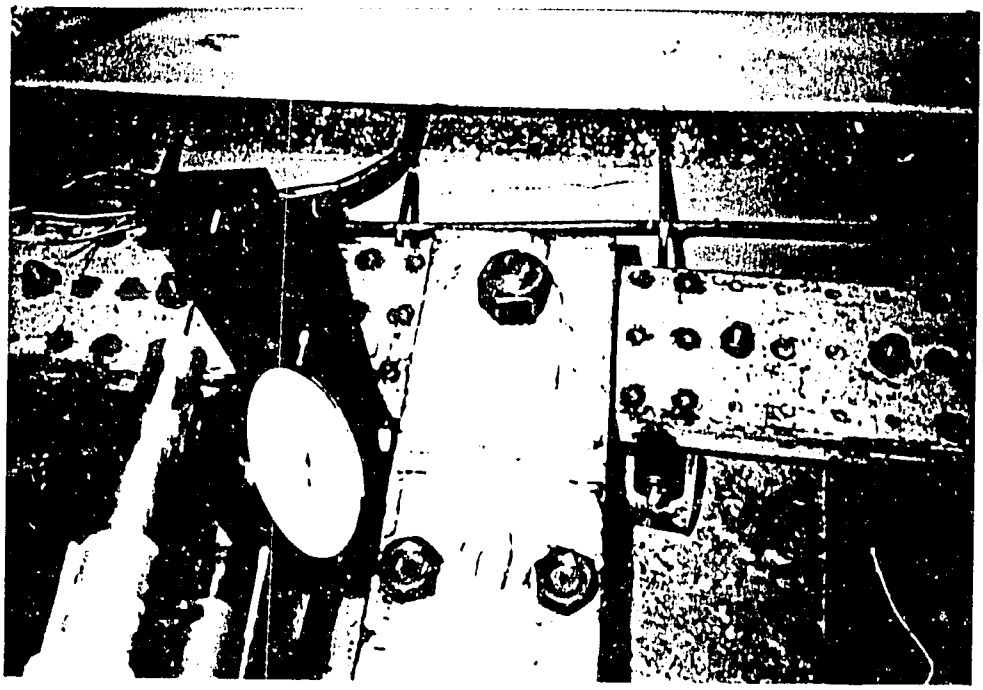

Fig. 21 Clamping Mechanism for the Pullout Test Showing Contraction Grippings Attached in the Longitudinal Members

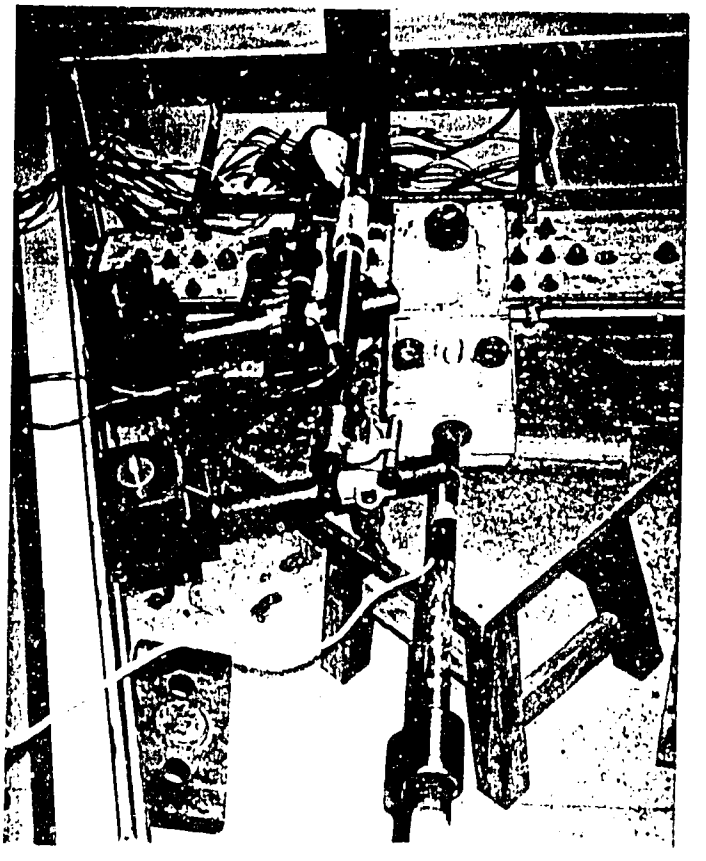

Fig. 22 Photograph of the LVDT and Dial Gage Positioned in Front of the Pullout Box

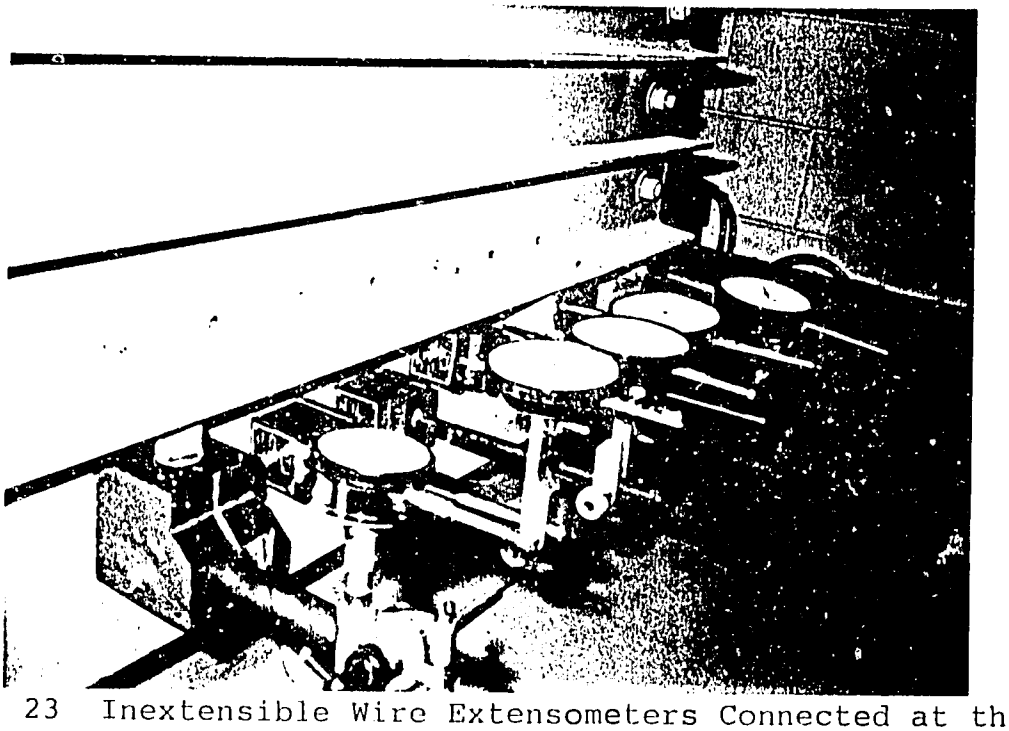

Fig. 23 Inextensible Wire Extensometers Connected at the Rear Portion of the Pullout Box

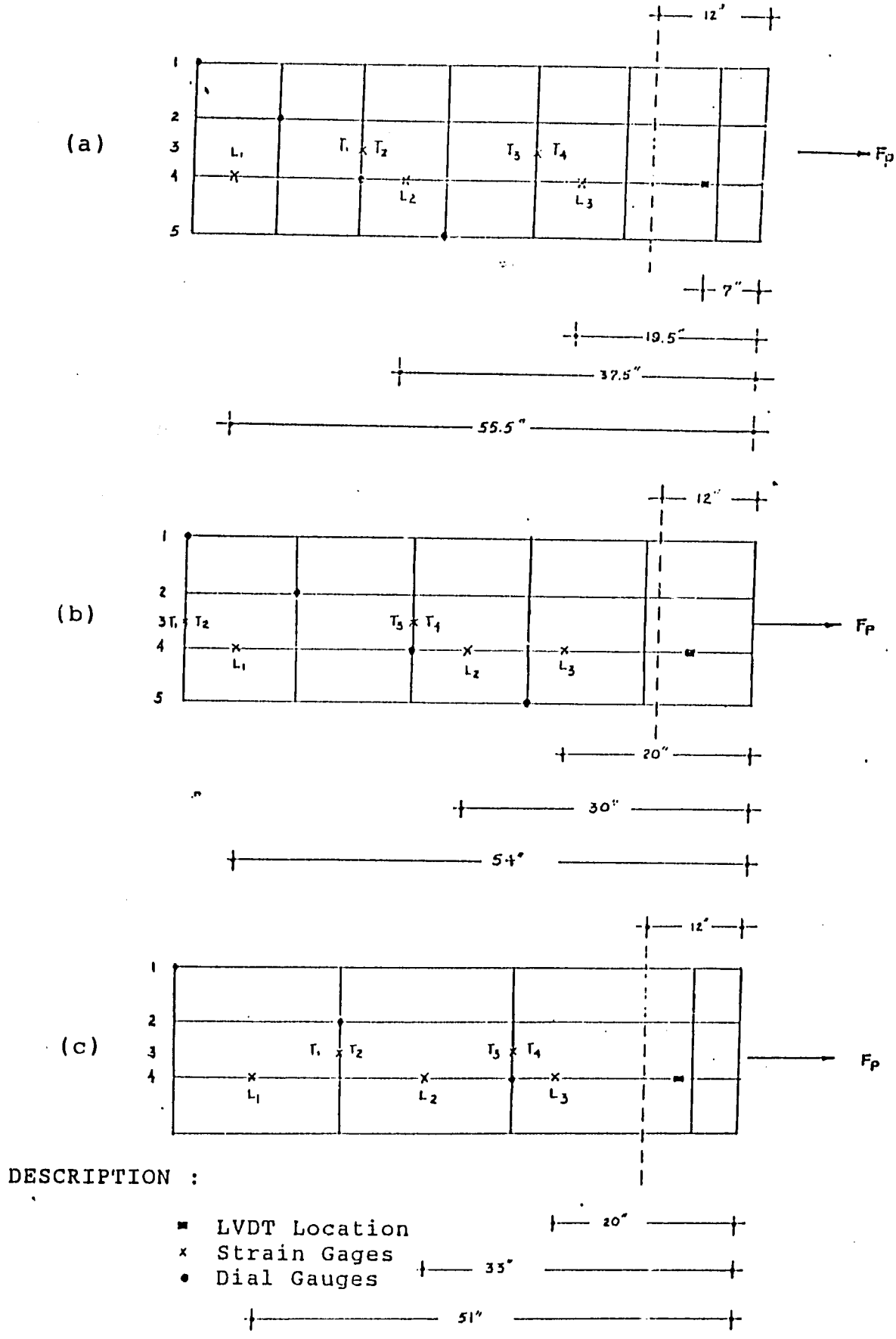

Fig. 24 Schematic Diagram of Strain Gages and Wire Extensometer Locations , a) 6"x9" mesh, b) 6"x12" mesh, c) 6"x18" mesh

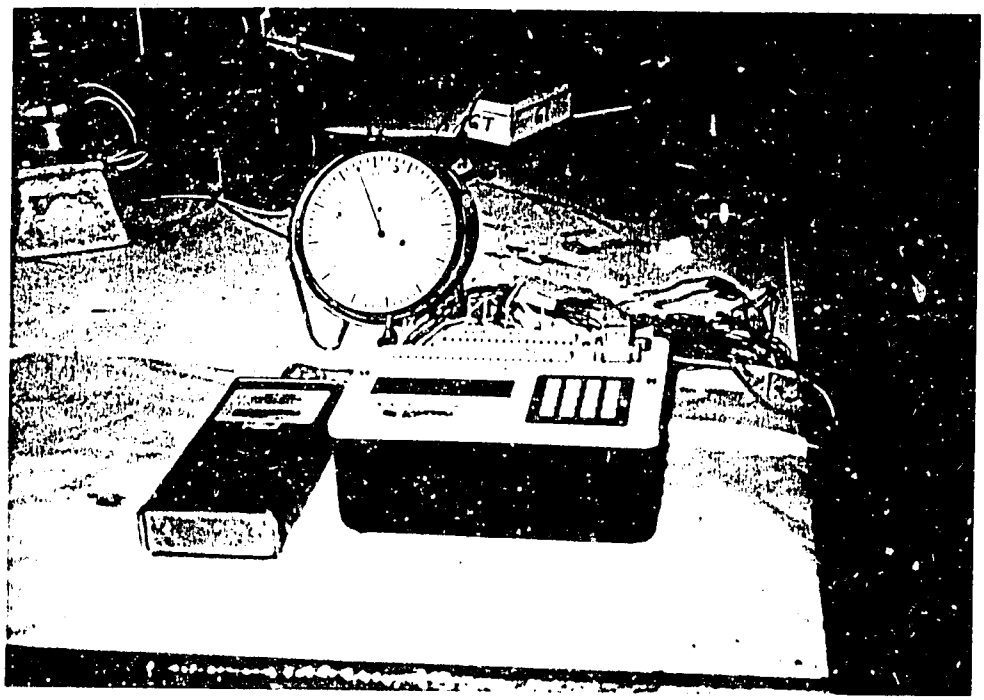

Fig. 25 Photograph of 21x Datalogger with the SM192 Storage Module while taking Strain Measurements During the Pullout Test

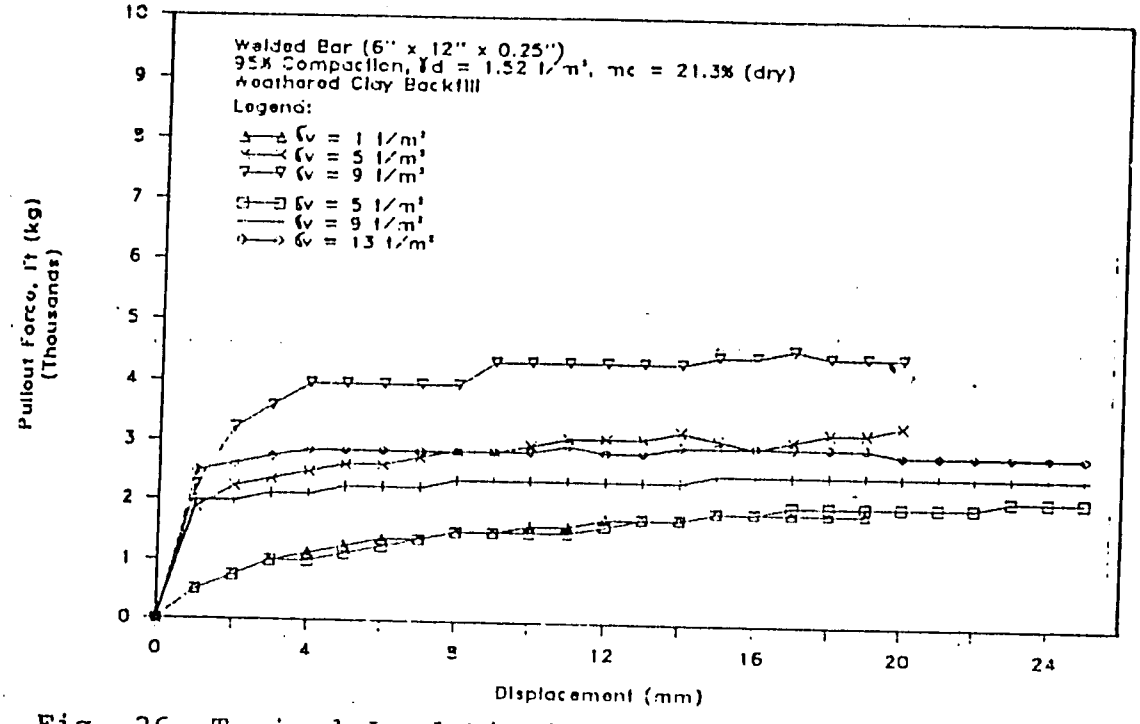

Fig. 26 Typical Load-Displacement Curves for Weathered Clay at the Dry Side of Optimum

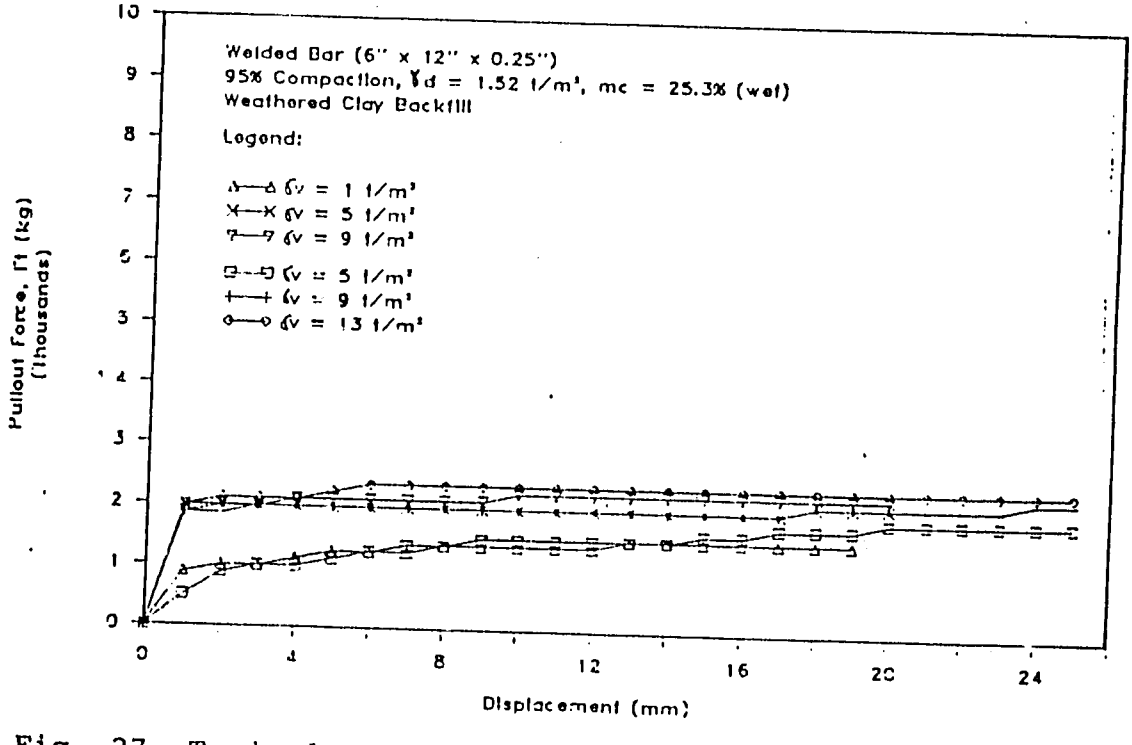

Fig. 27 Typical Load-Displacement Curves for Weathered Clay at the Wet Side of Optimum

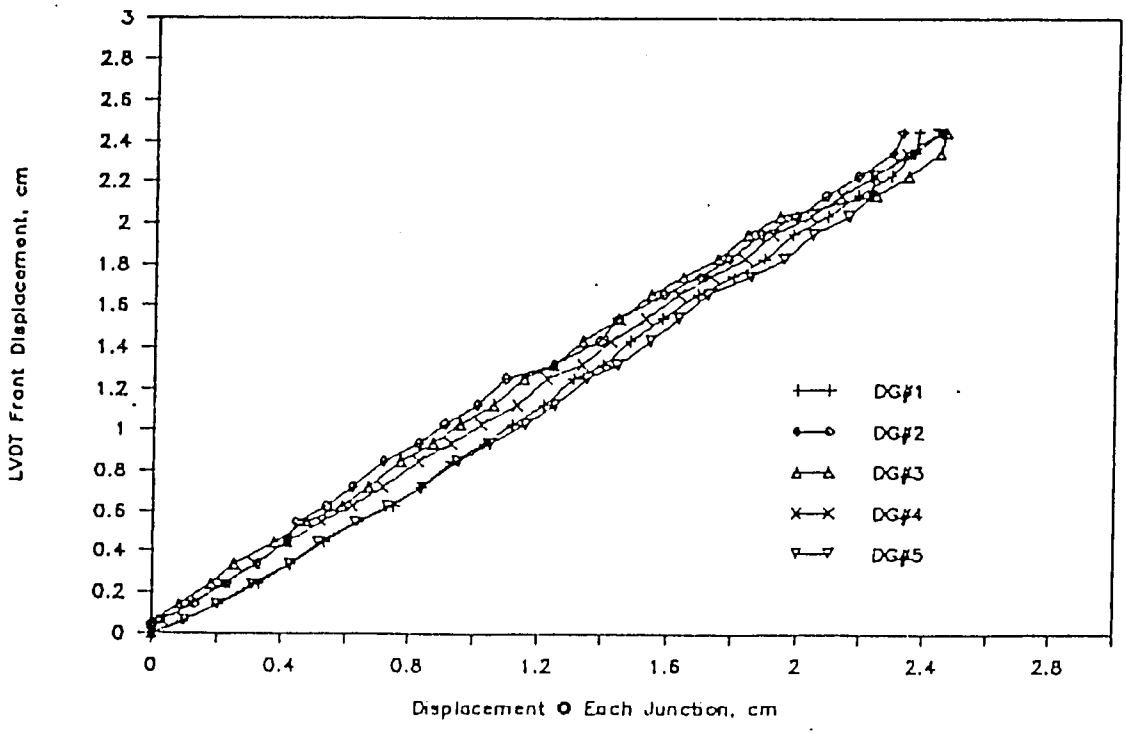

Fig. 28 Typical Plot of the Front Displacement of Mat Against the Displacement of each Junction for a 6"x12"x3/8" mesh compacted at the Dry Side of Optimum

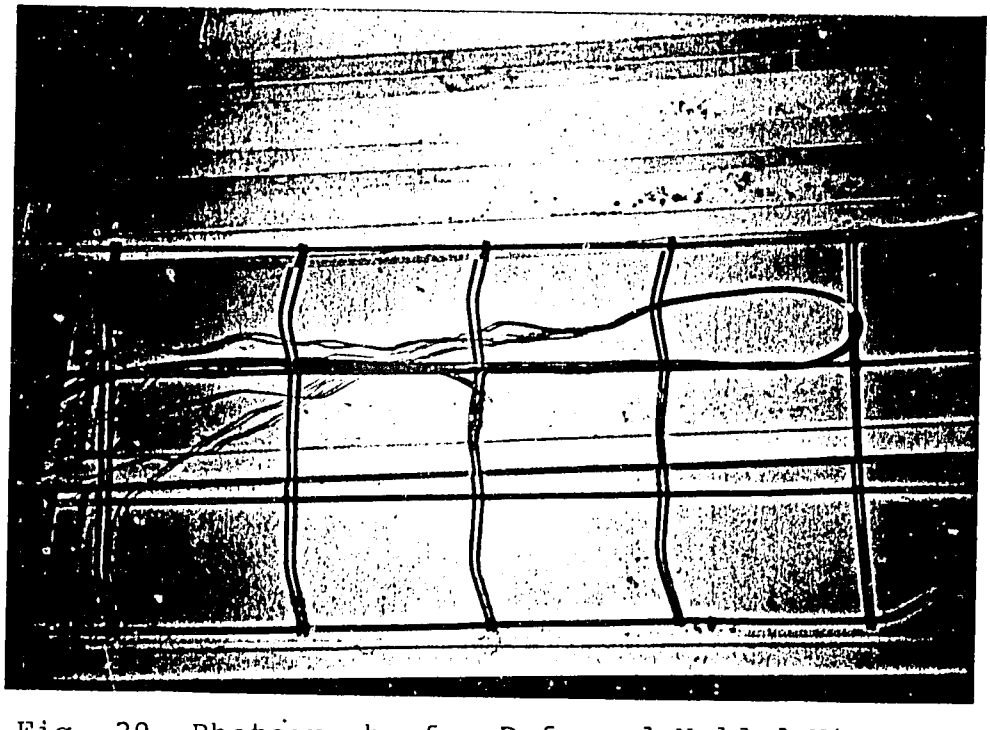

Fig. 29 Photograph of a Deformed Welded Wire Mat After the Test

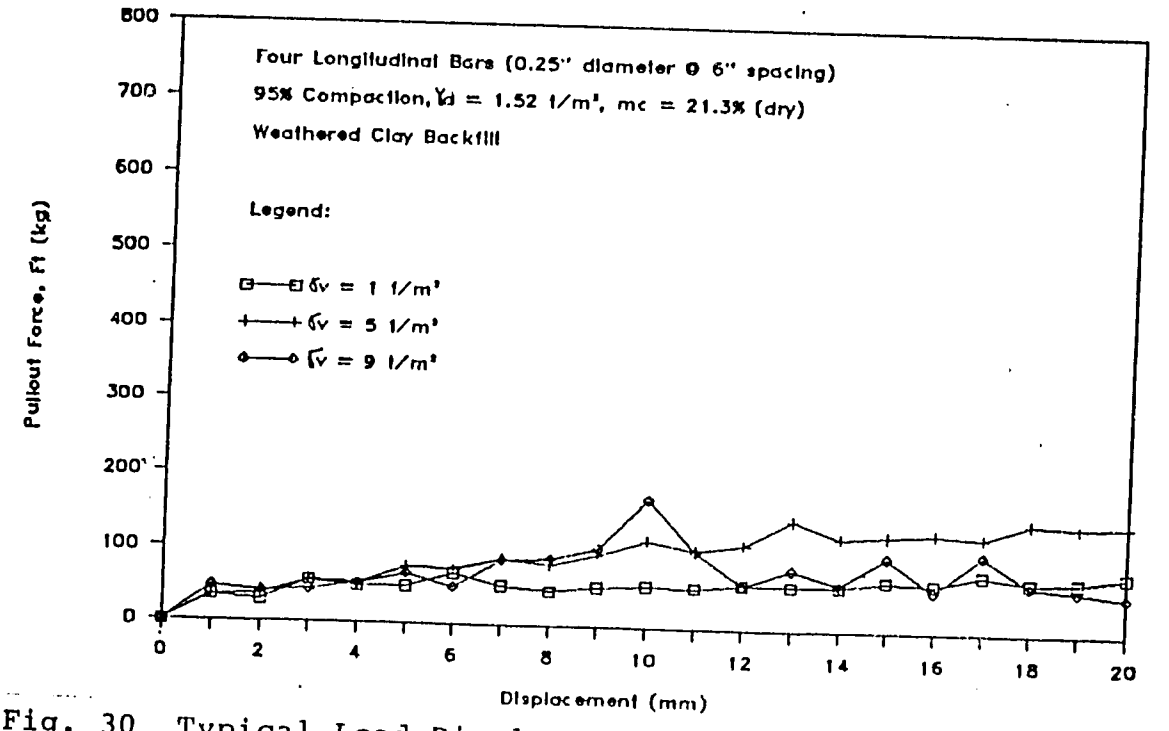

Fig. 30 Typical Load-Displacement Curves of Longitudinal Bars Embedded in Weathered Clay Backfill Compacted at the Dry Side of Optimum (1/4" Bar Diameter)

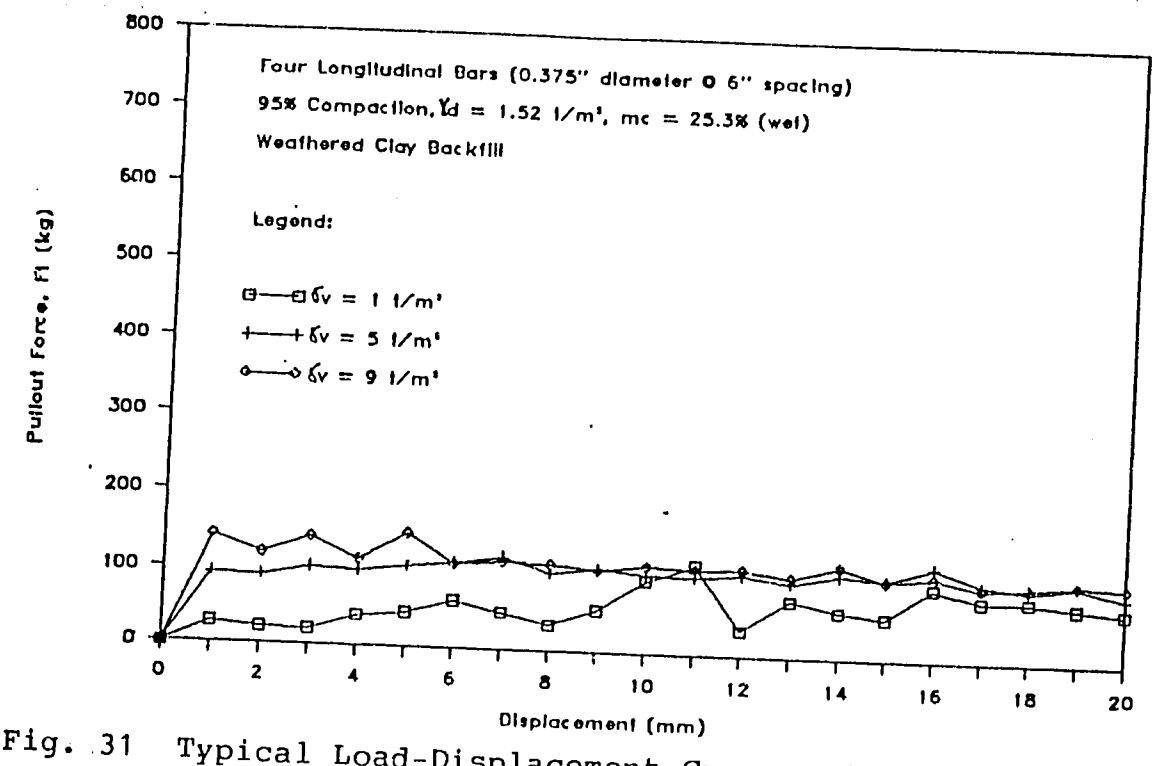

Fig. 31 Typical Load-Displacement Curves of Longitudinal Bars Embedded in Weathered Clay Backfill Compacted at the Wet Side of Optimum (3/8" Bar Diameter)

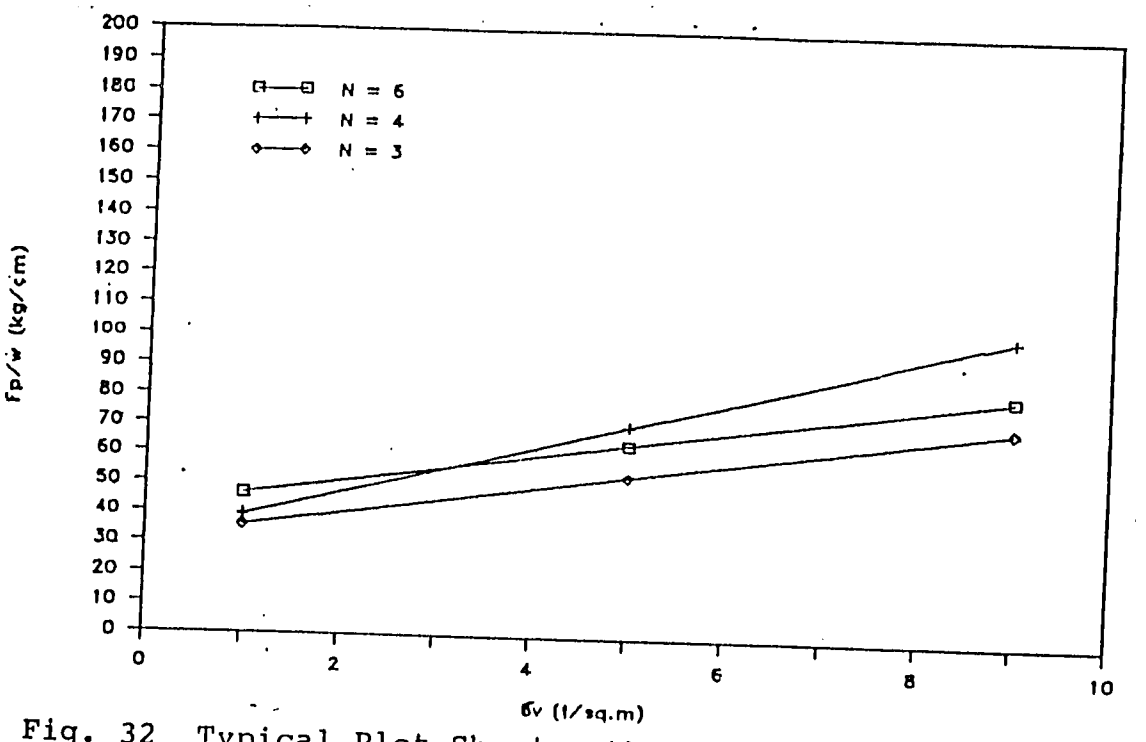

Fig. 32 Typical Plot Showing the Effect of the Number of Transverse Wires on the Passive Resistance of Transverse Members for Weathered Clay Compacted at Dry Side of Optimum

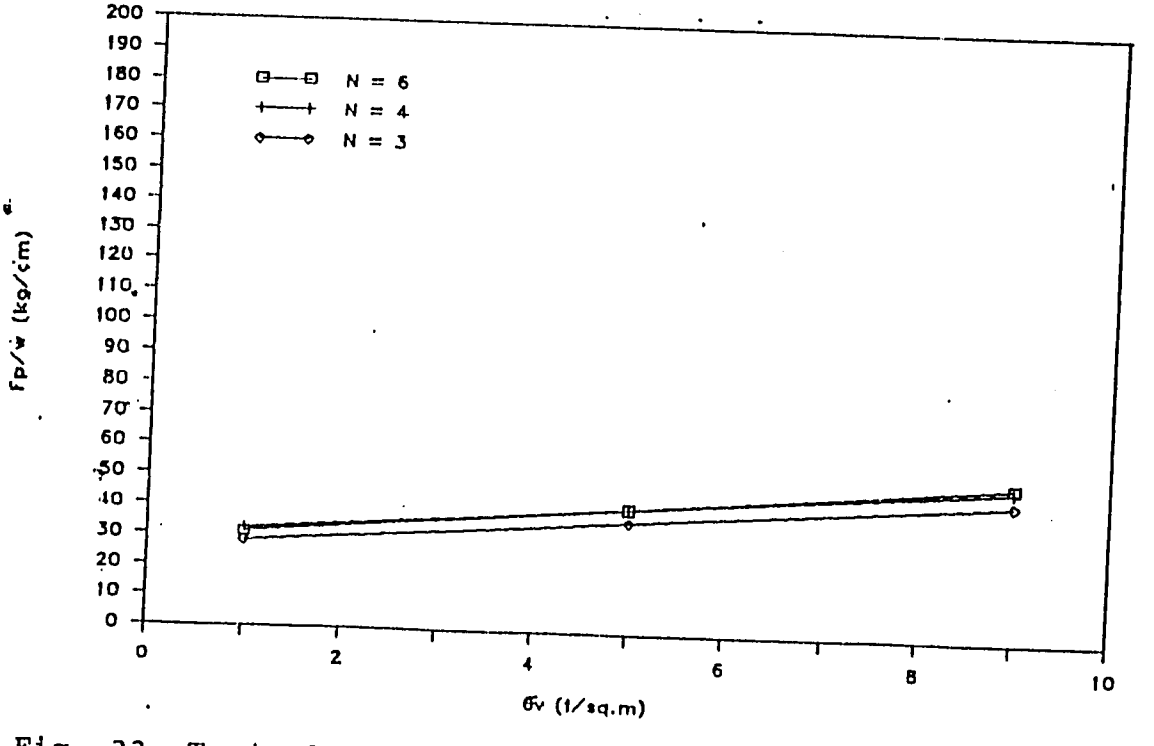

Fig. 33 Typical Plot Showing the Effect of the Number of Transverse Wires on the Passive Resistance of Transverse Members for Weathered Clay Compacted at Wet Side of Optimum

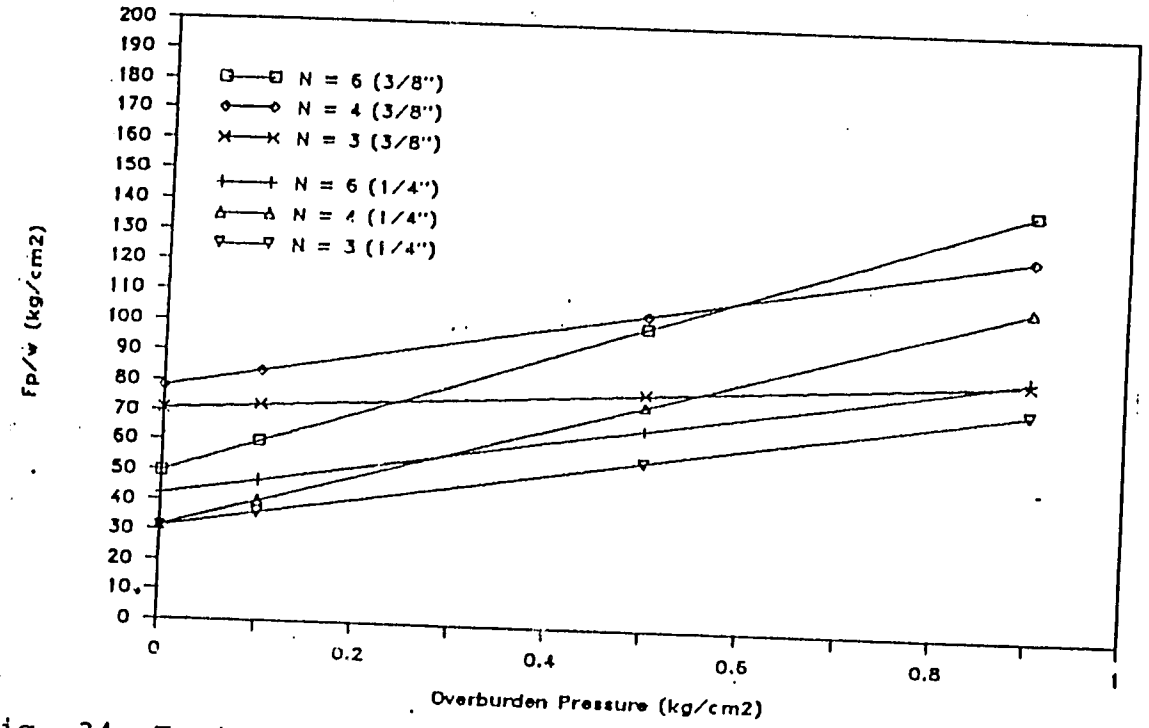

Fig. 34 Typical Plot Showing the Effect of the Bar Diameter on the Passive Resistance of Transverse Members for Weathered Clay Compacted at Dry Side of Optimum

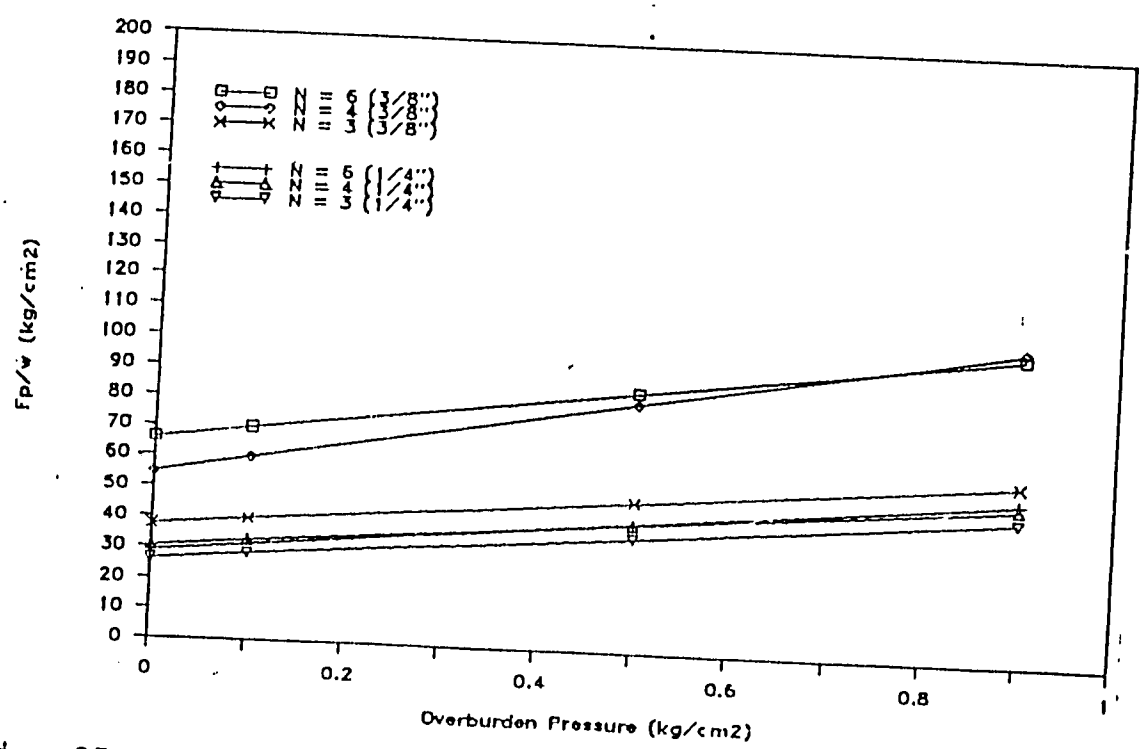

Fig. 35 Typical Plot Showing the Effect of the Bar Diameter on the Passive Resistance of Transverse Members for Weathered Clay Compacted at Wet Side of Optimum

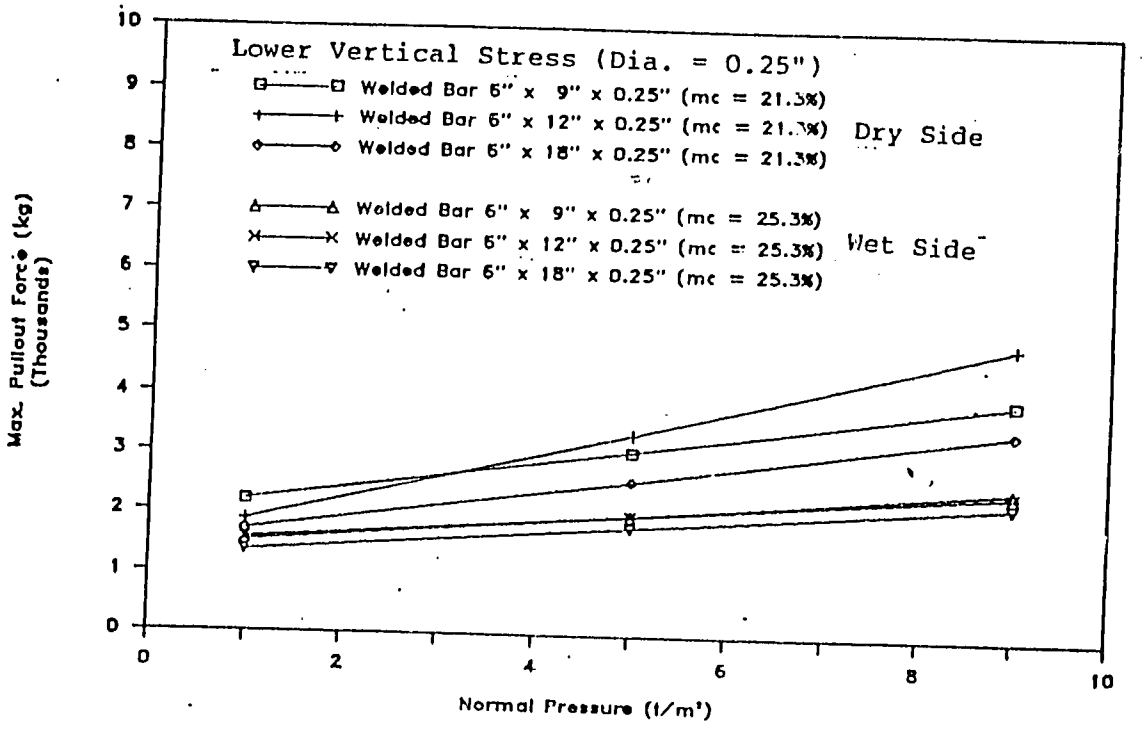

(a)

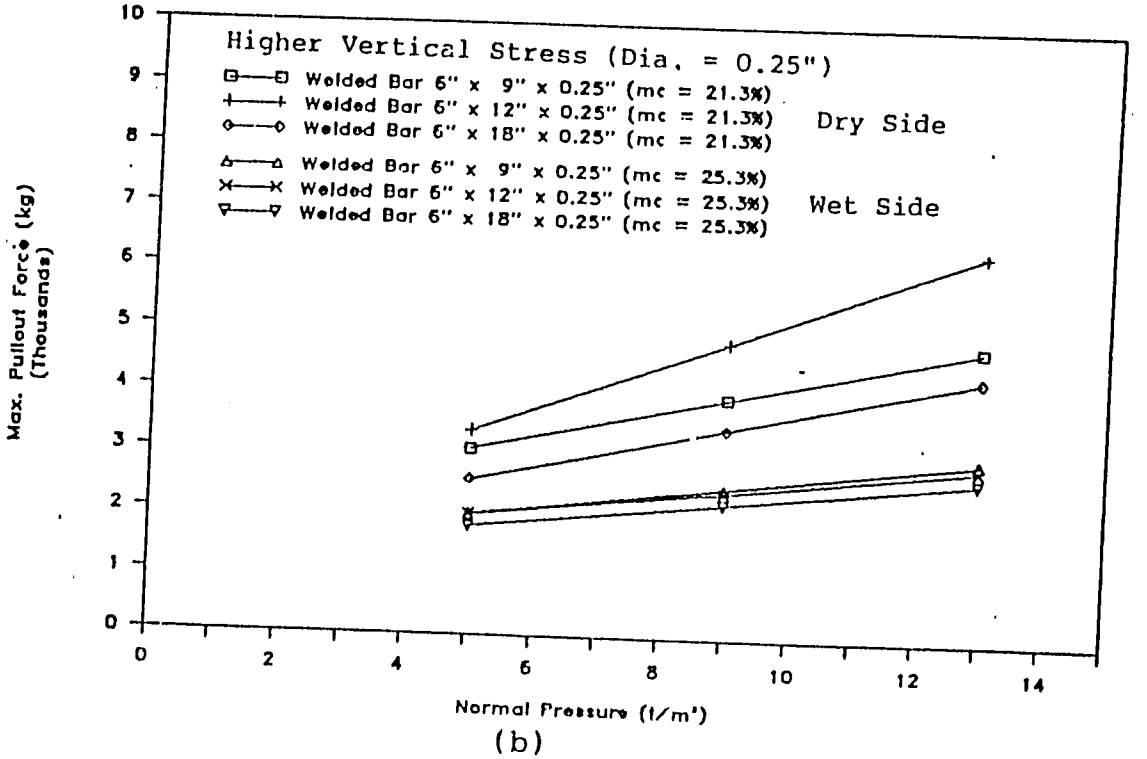

(b)

Fig. 36 Typical Variation of the Total Pullout Resistance with Normal Pressure for Weathered Clay Backfill a) Lower Vertical Stress, b) Higher Vertical Stress

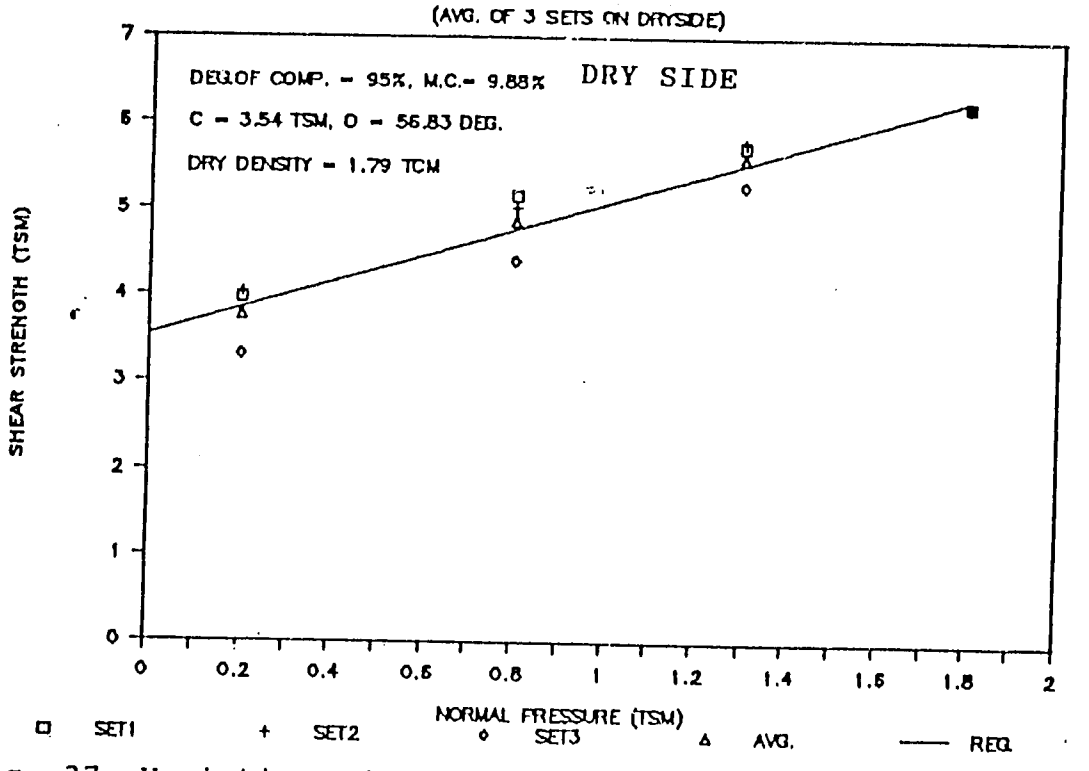

Fig. 37 Variation of Shear Strength with Normal Pressure from Direct Shear Test on Lateritic Residual Soil (Dry Side of Optimum)

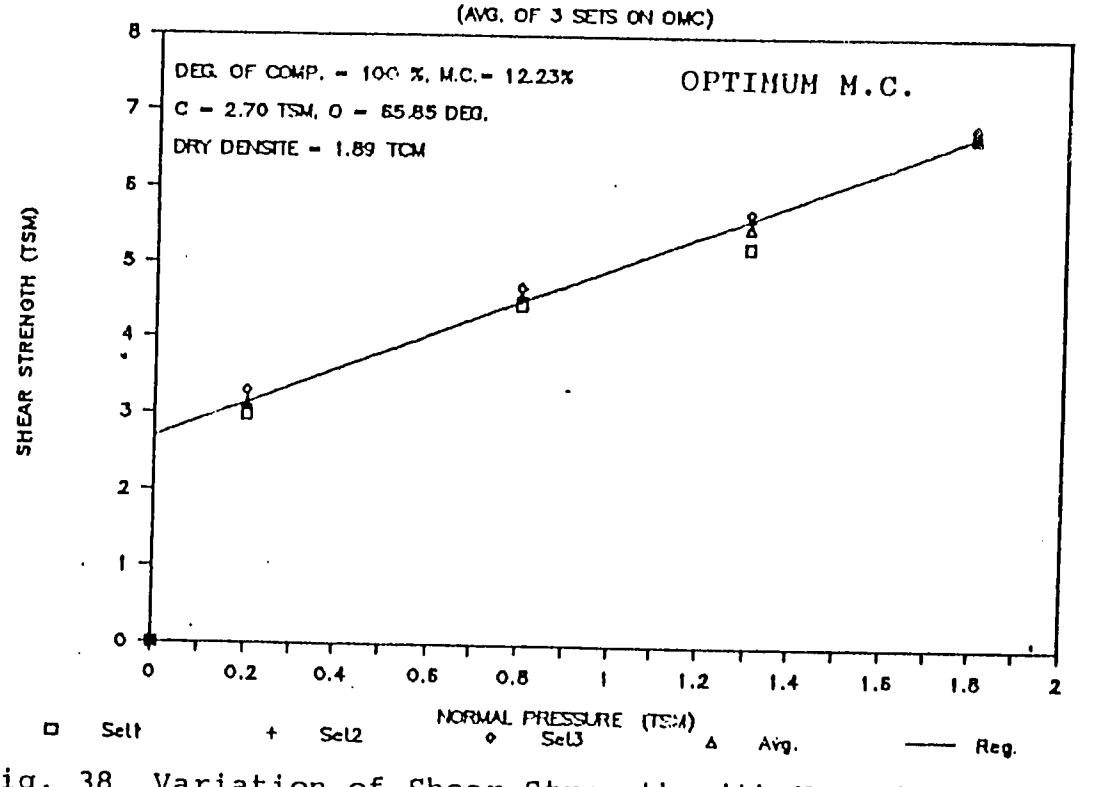

Fig. 38 Variation of Shear Strength with Normal Pressure from Direct Shear Test on Lateritic Residual Soil (Optimum Moisture Content)

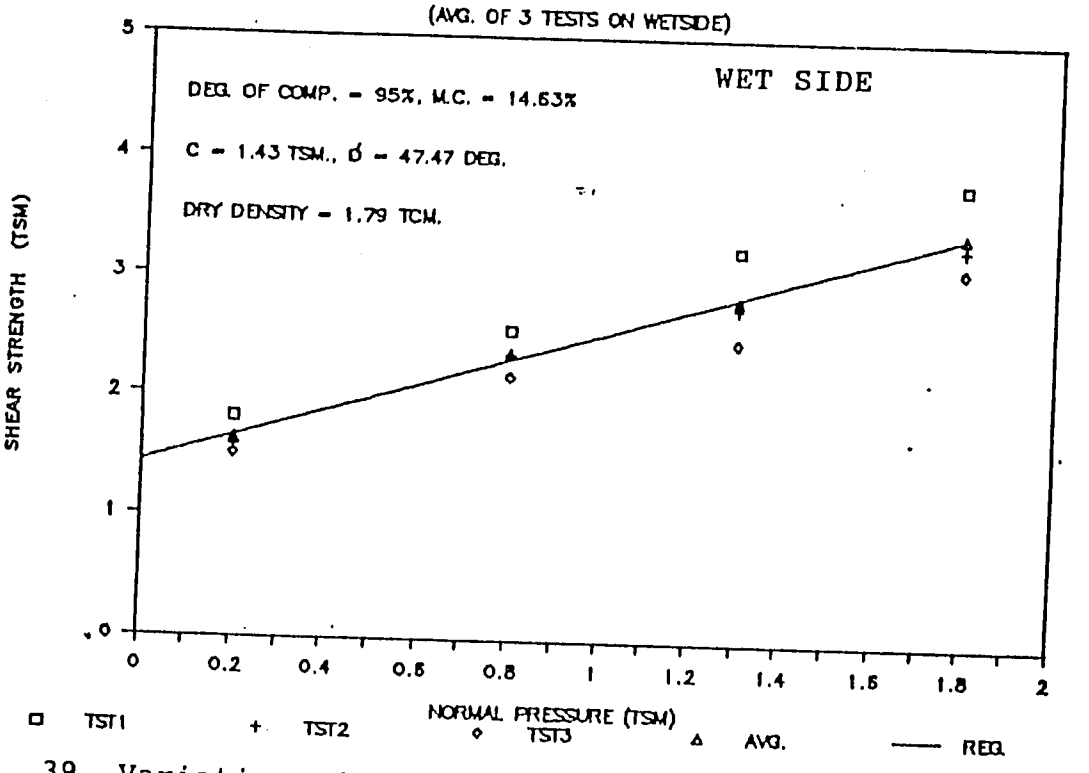

Fig. 39 Variation of Shear Strength with Normal Pressure from Direct Shear Test on Lateritic Residual Soil (Wet Side of Optimum)

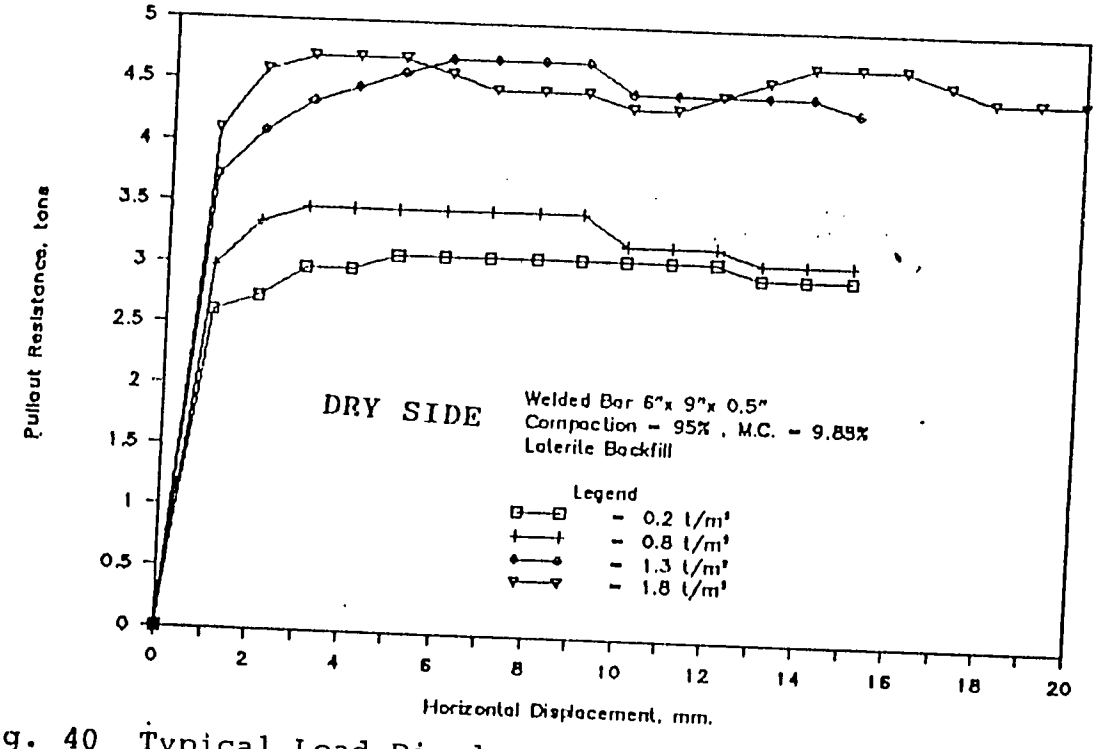

Fig. 40 Typical Load-Displacement Curves from Pullout Test on Lateritic Residual Soil Compacted at the Dry Side of Optimum

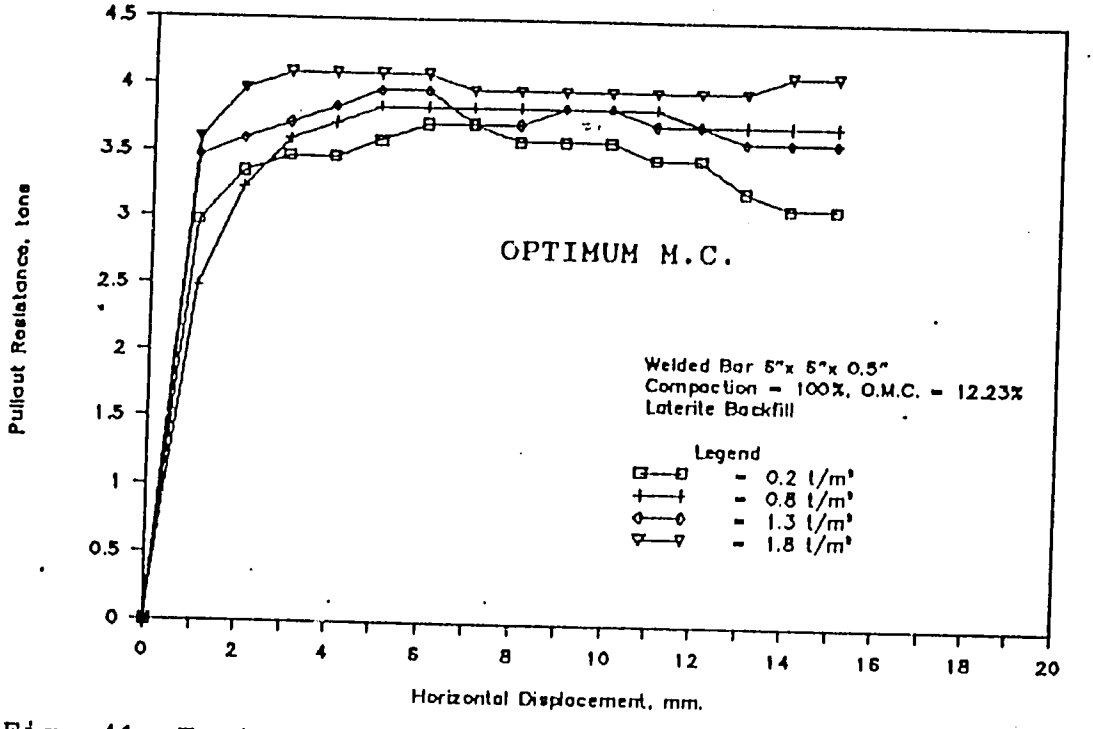

Fig. 41 Typical Load-Displacement Curves from Pullout Test on Lateritic Residual Soil Compacted at the Optimum Moisture Content

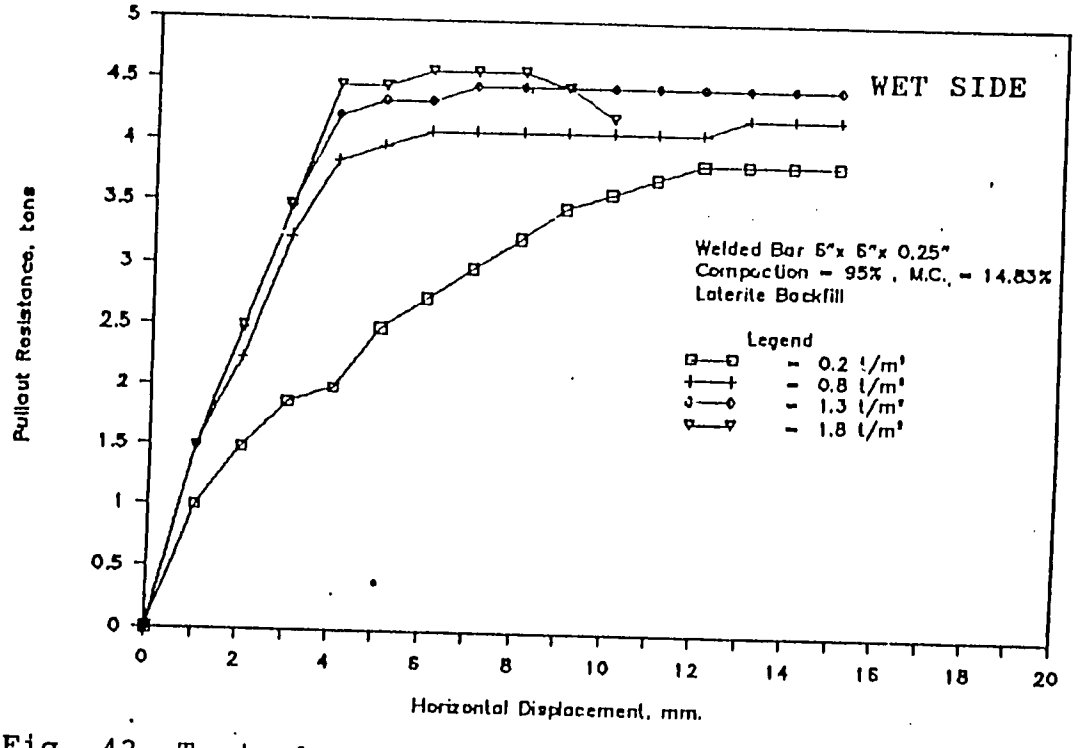

Fig. 42 Typical Load-Displacement Curves from Pullout Test on Lateritic Residual Soil Compacted at the Wet Side of Optimum

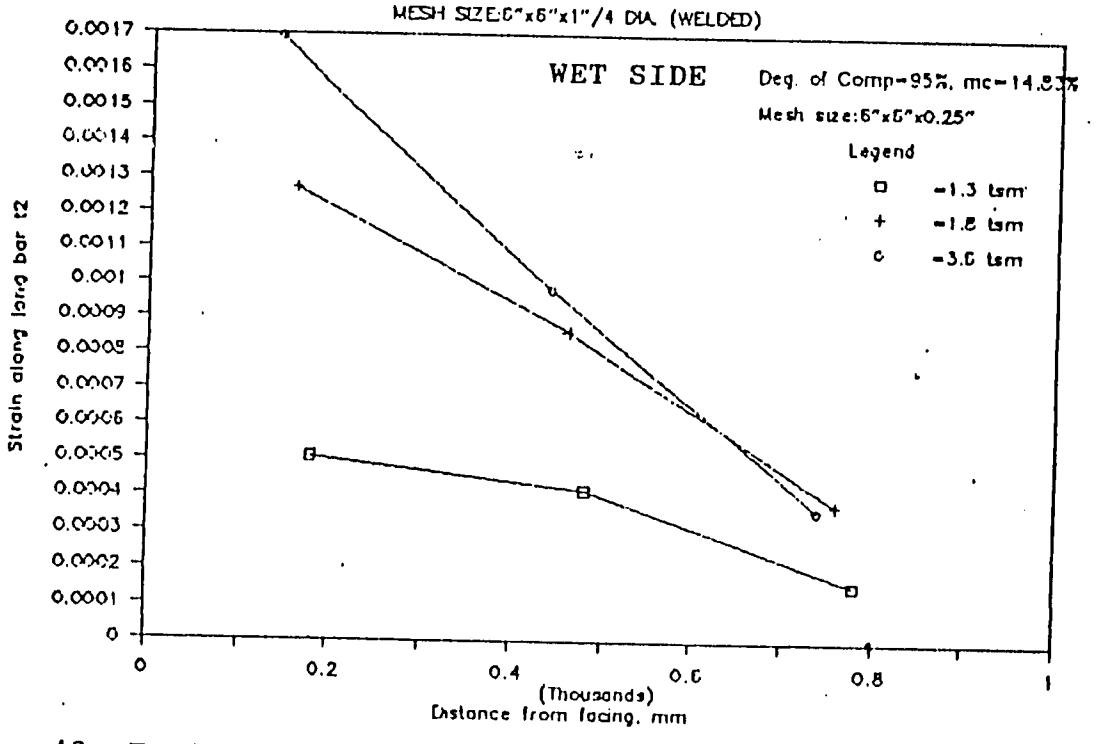

Fig. 43 Typical Variation of Strains with Distance from the Front Face of Pullout Box (Lateritic Residual Soil - Wet Side of Optimum)

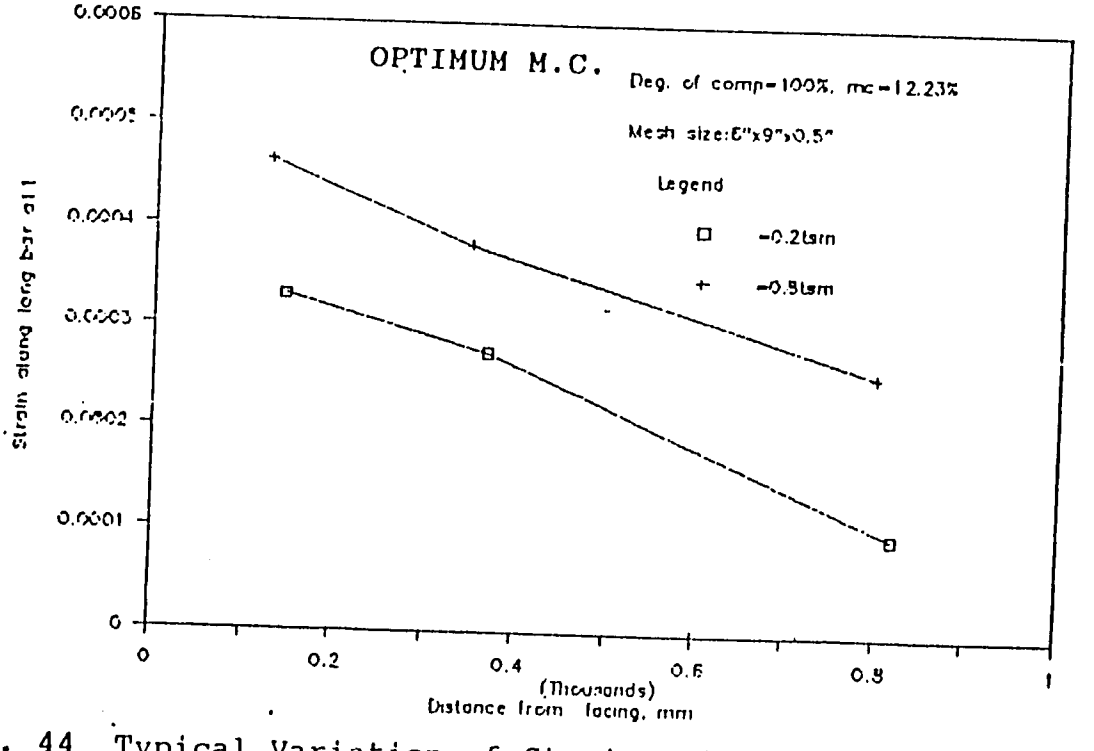

Fig. 44 Typical Variation of Strains with Distance from the Front Face of Pullout Box (Lateritic Residual Soil - Optimum Moisture Content)

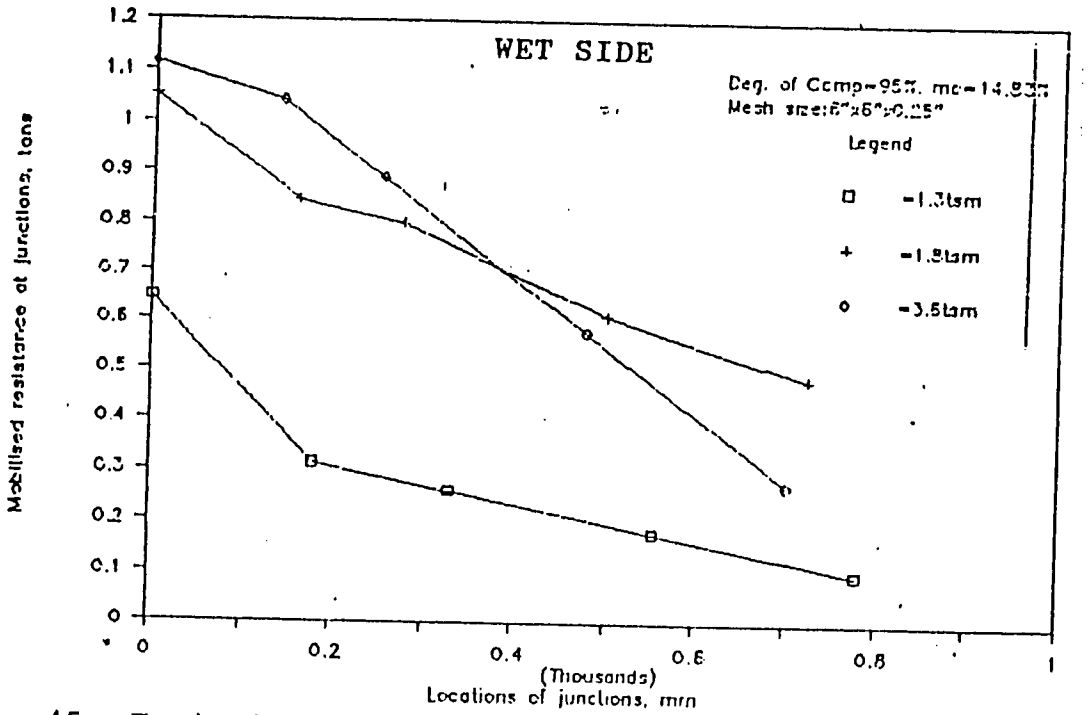

Fig. 45 Typical Variation of the Mobilized Resistance at Grid Junctions with Distance from the Front Face of the Pullout Box (Lateritic Residual Soil- Wet Side of Optimum)

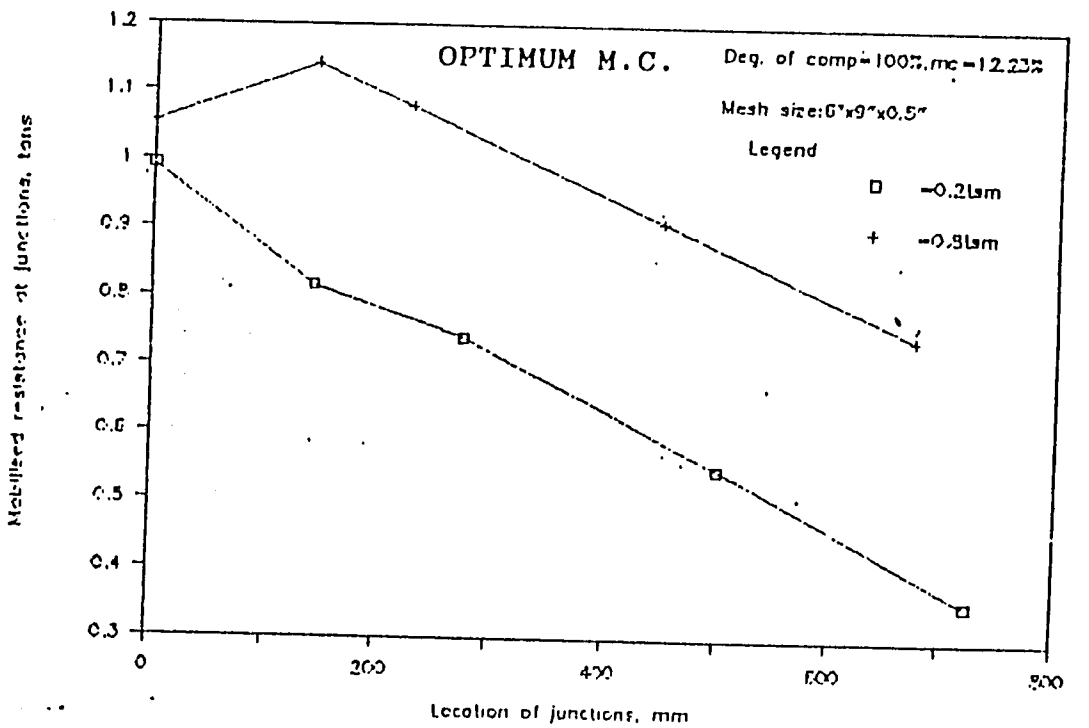

Fig. 46 Typical Variation of the Mobilized Resistance at Grid Junctions with Distance from the Front Face of the Pullout Box (Lateritic Residual Soil - Optimum Moisture Content)

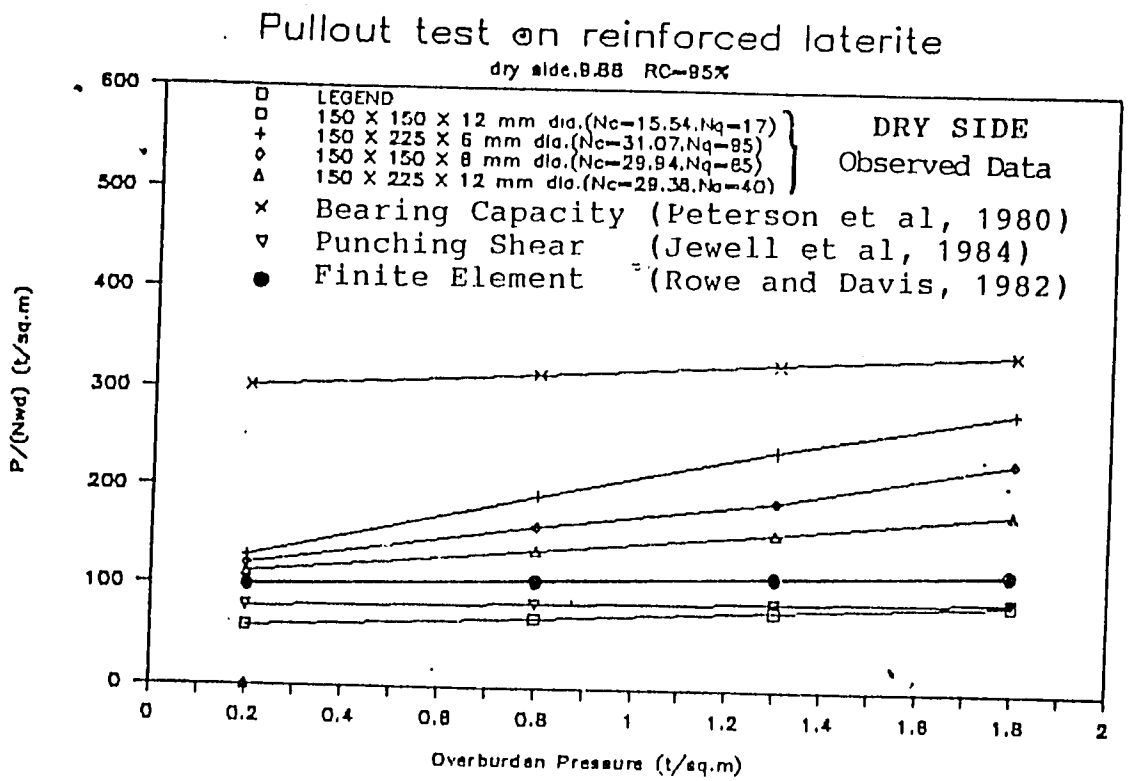

Fig. 47 Comparison of the Observed and Theoretically Predicted Values of Normalized Passive Resistance Plotted Against the Overburden Pressure for Lateritic Residual Soil (Dry Side of Optimum)

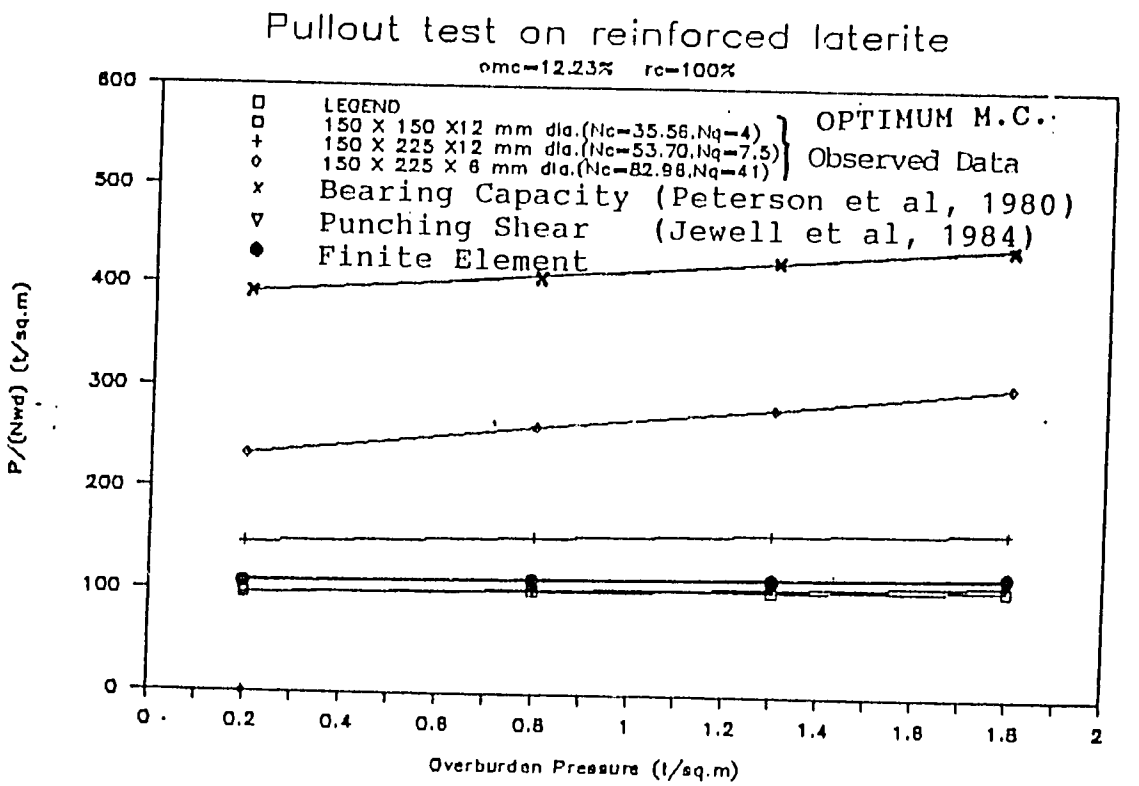

Fig. 48 Comparison of the Observed and Theoretically Predicted Values of Normalized Passive Resistance Plotted Against the Overburden Pressure for Lateritic Residual Soil (Optimum Moisture Content)

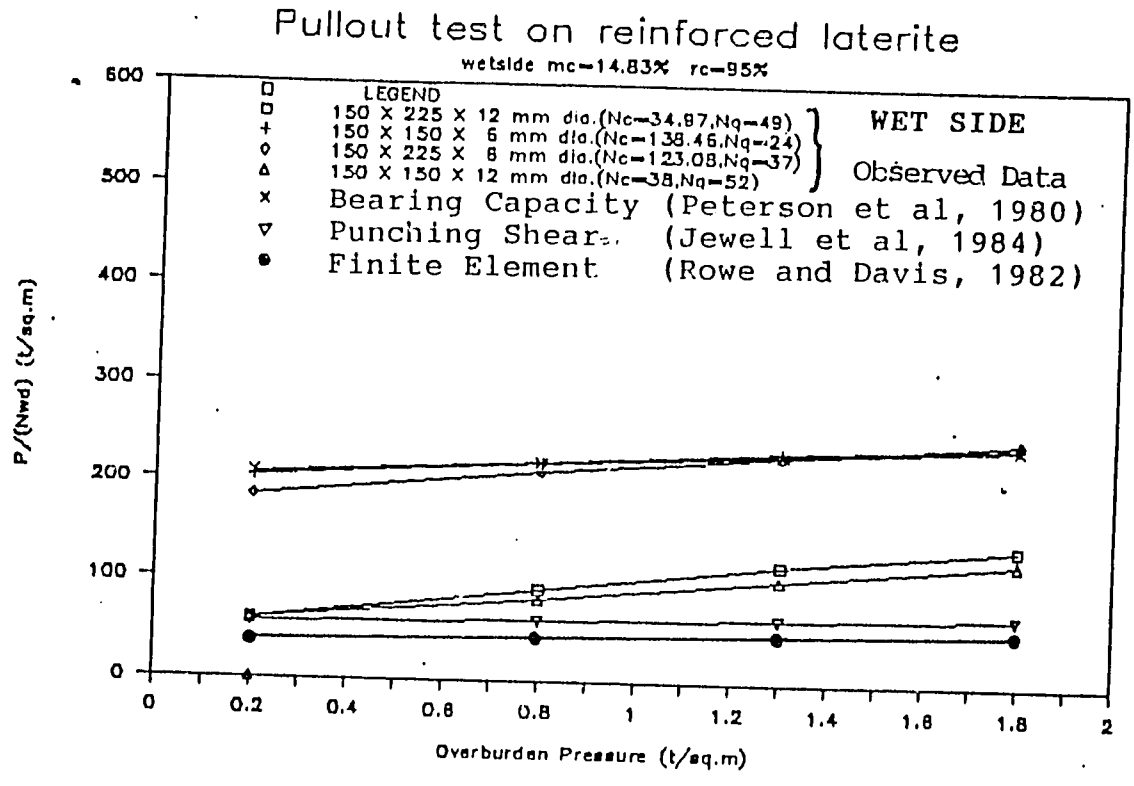

Fig. 49 Comparison of the Observed and Theoretically Predicted Values of Normalized Passive Resistance Plotted Against the Overburden Pressure for Lateritic Residual Soil (Wet Side of Optimum)

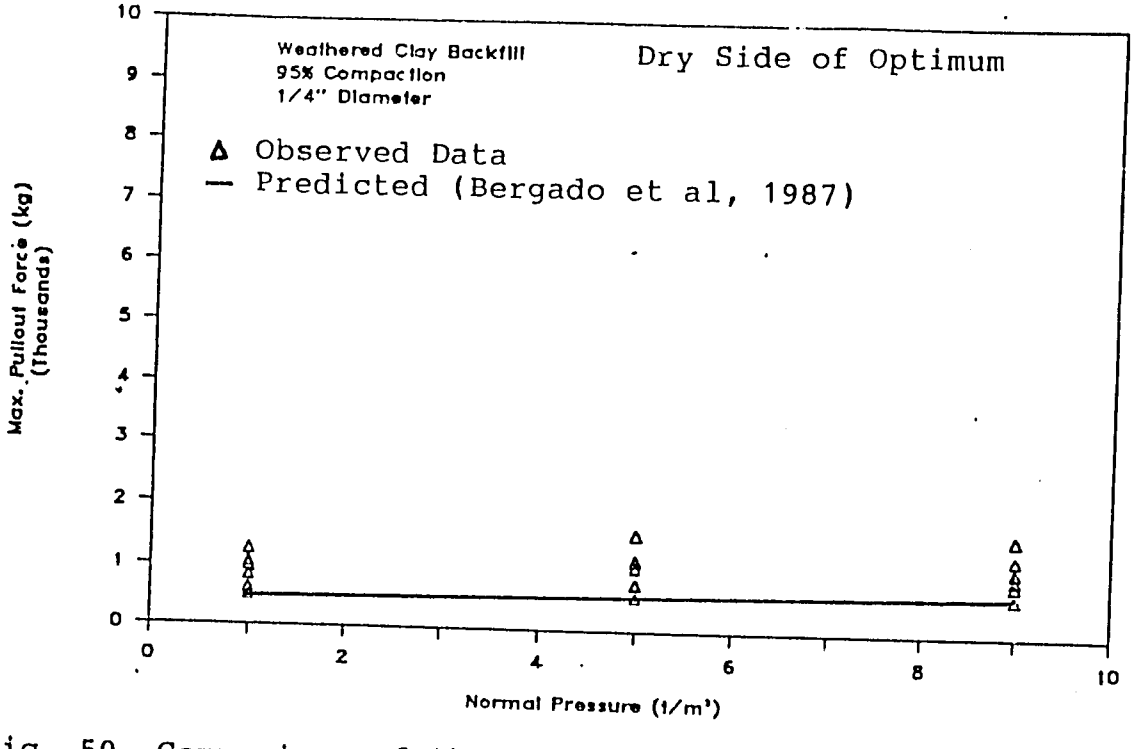

Fig. 50 Comparison of the Observed Maximum Total Pullout Resistance with Predicted Values for Weathered Clay Backfill Compacted at the Dry Side of Optimum (1/4" Bar Diameter)

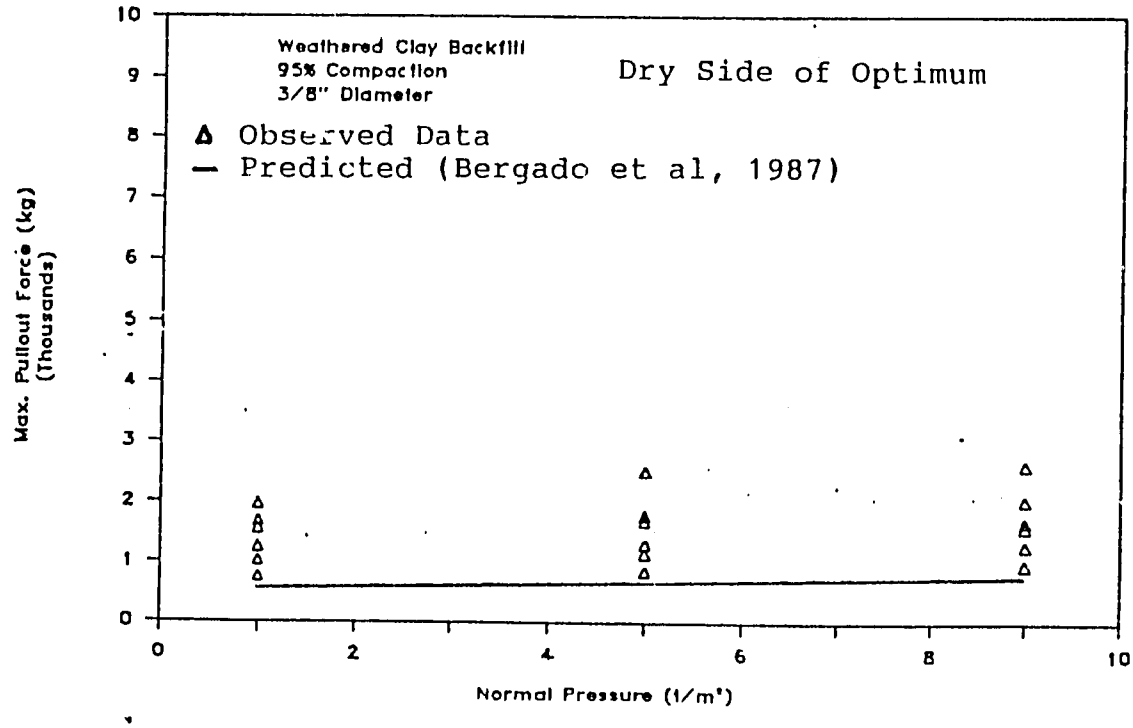

Fig. 51 Comparison of the Observed Maximum Total Pullout Resistance with Predicted Values for Weathered Clay Backfill Compacted at the Dry Side of Optimum (3/8" Bar Diameter)

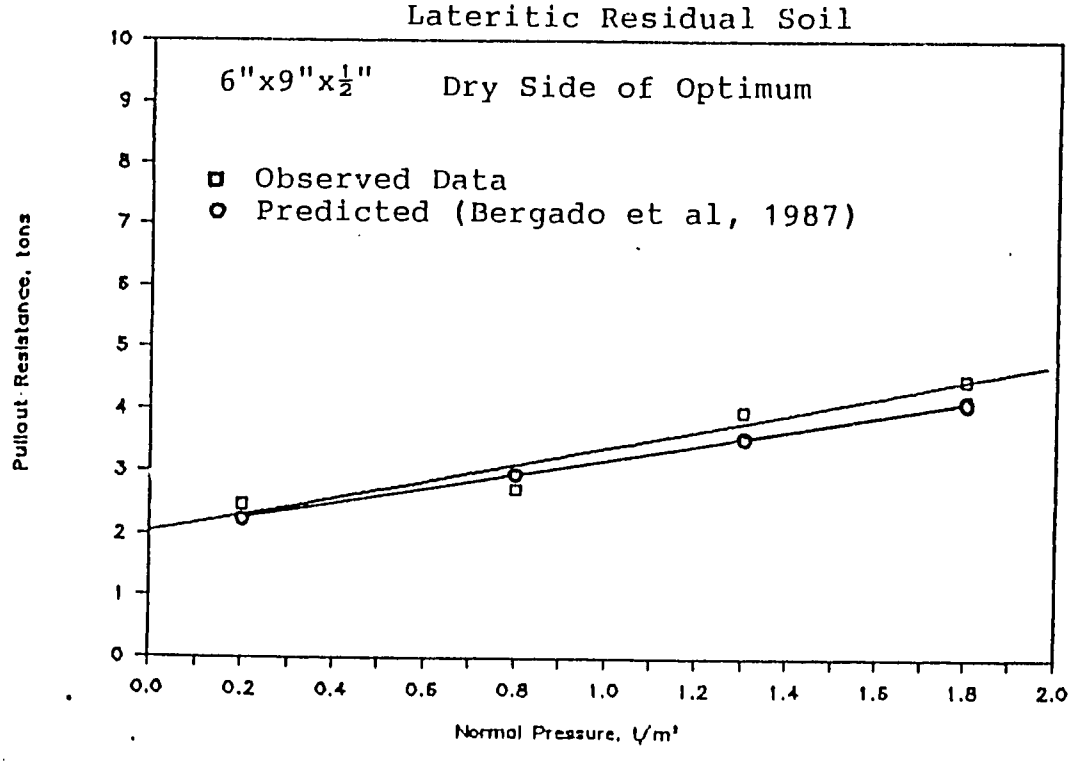

Fig. 52 Comparison of the Observed Maximum Total Pullout Resistance with Predicted Values for Lateritic Residual Soil Compacted at the Dry Side of Optimum

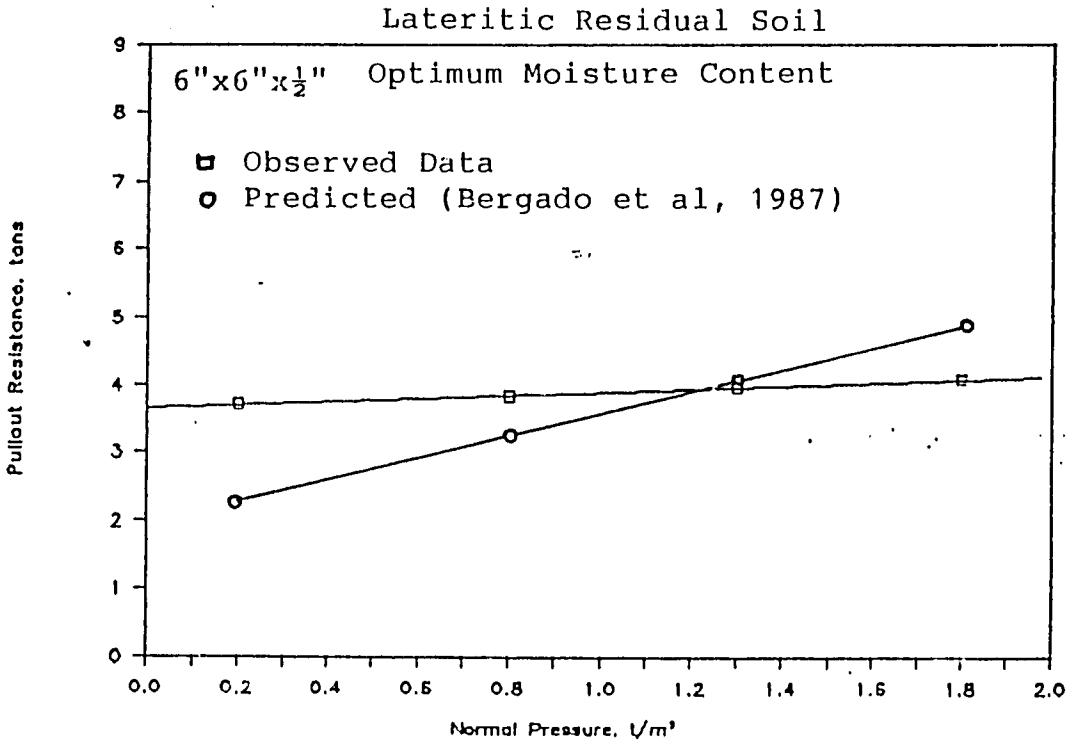

Fig. 53 Comparison of the Observed Maximum Total Pullout Resistance with Predicted Values for Lateritic Residual Soil Compacted at the Optimum Moisture Content

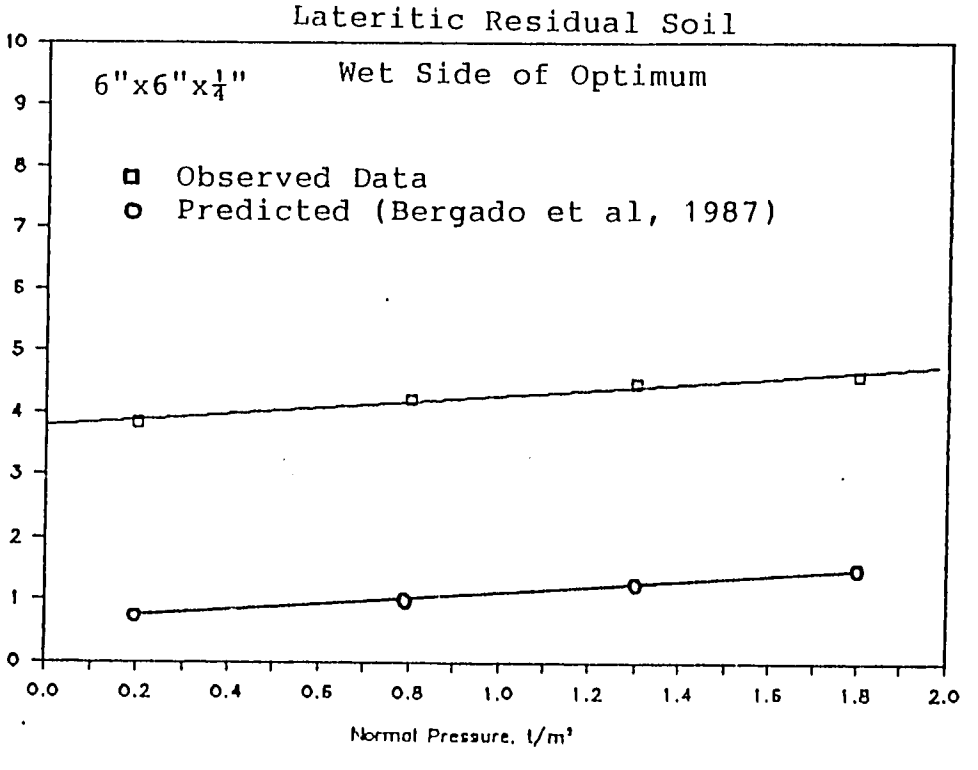

Fig. 54 Comparison of the Observed Maximum Total Pullout Resistance with Predicted Values for Lateritic Residual Soil Compacted at the Dry Side of Optimum

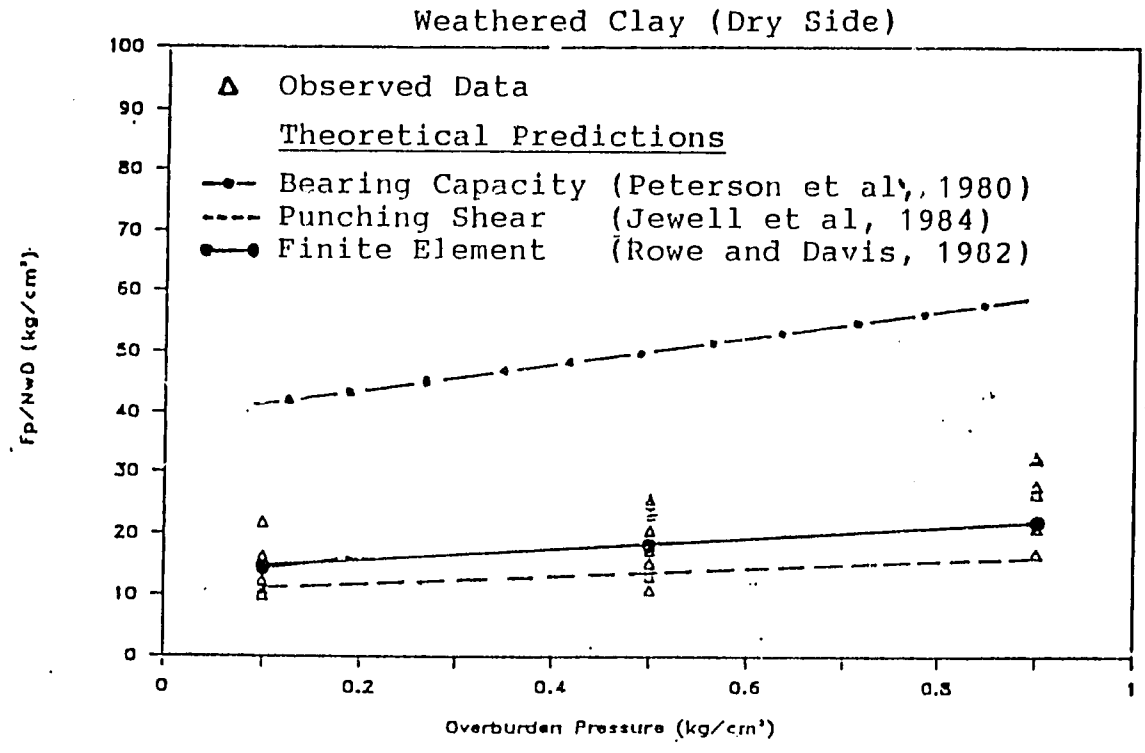

Fig. 55 Predicted Versus Observed Passive Resistance of Transverse Members for Weathered Clay Backfill Compacted at the Dry Side of Optimum

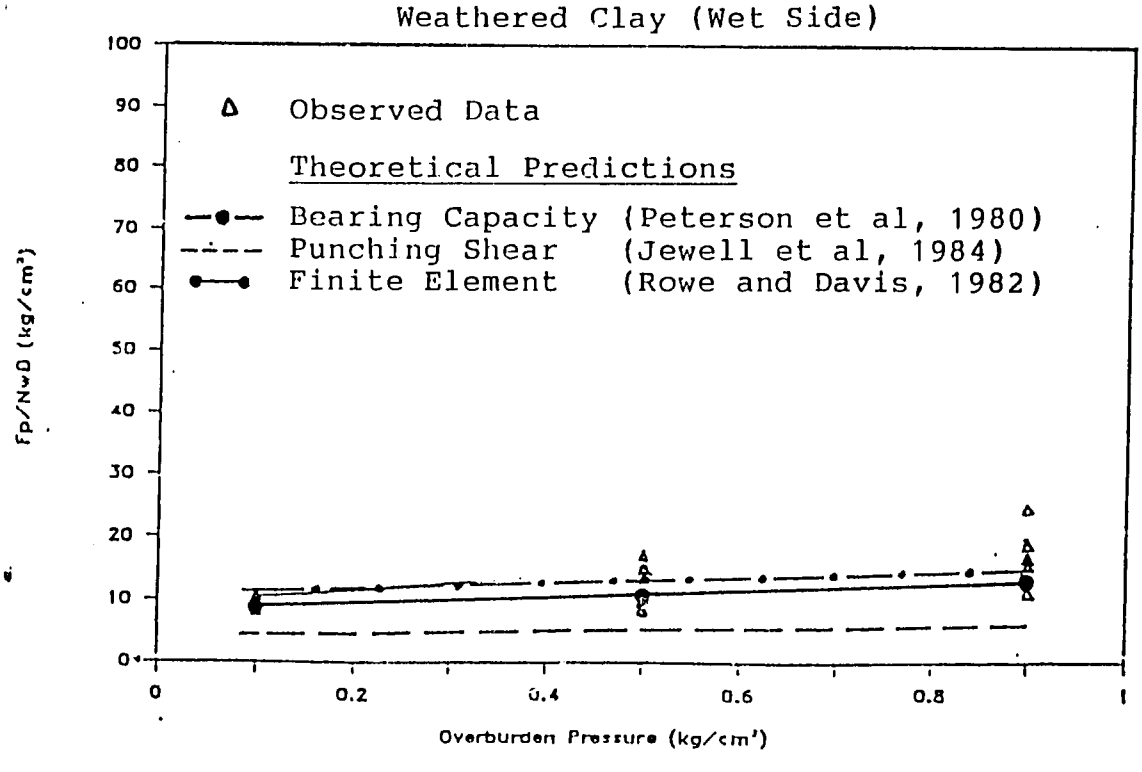

Fig. 56 Predicted Versus Observed Passive Resistance of Transverse Members for Weathered Clay Backfill Compacted at the Wet Side of Optimum

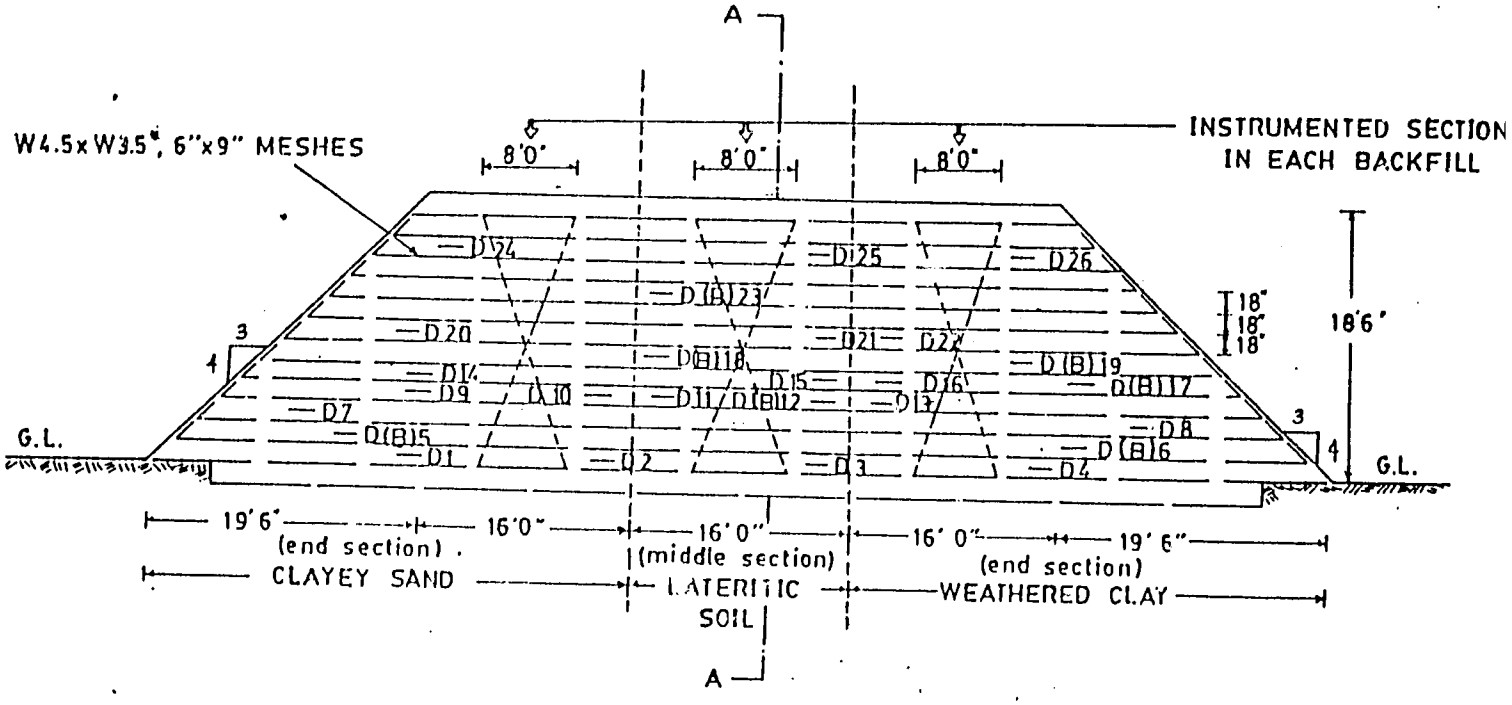

Fig. 57 Front Section of the Welded Wire Wall

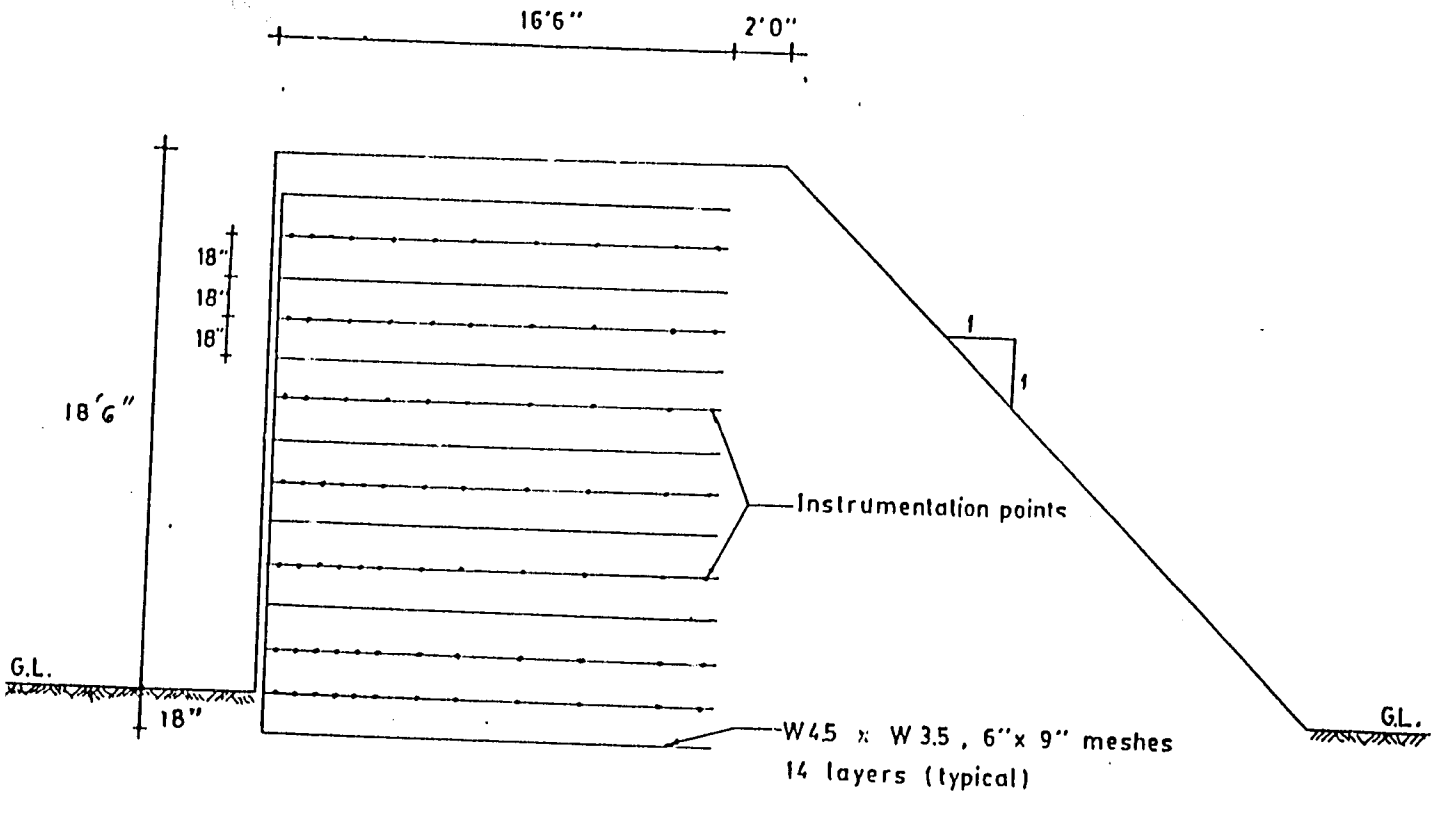

Fig. 58 View of the Welded Wire Wall Along Section A-A Showing the Instrumented Welded Wire Mat Layers

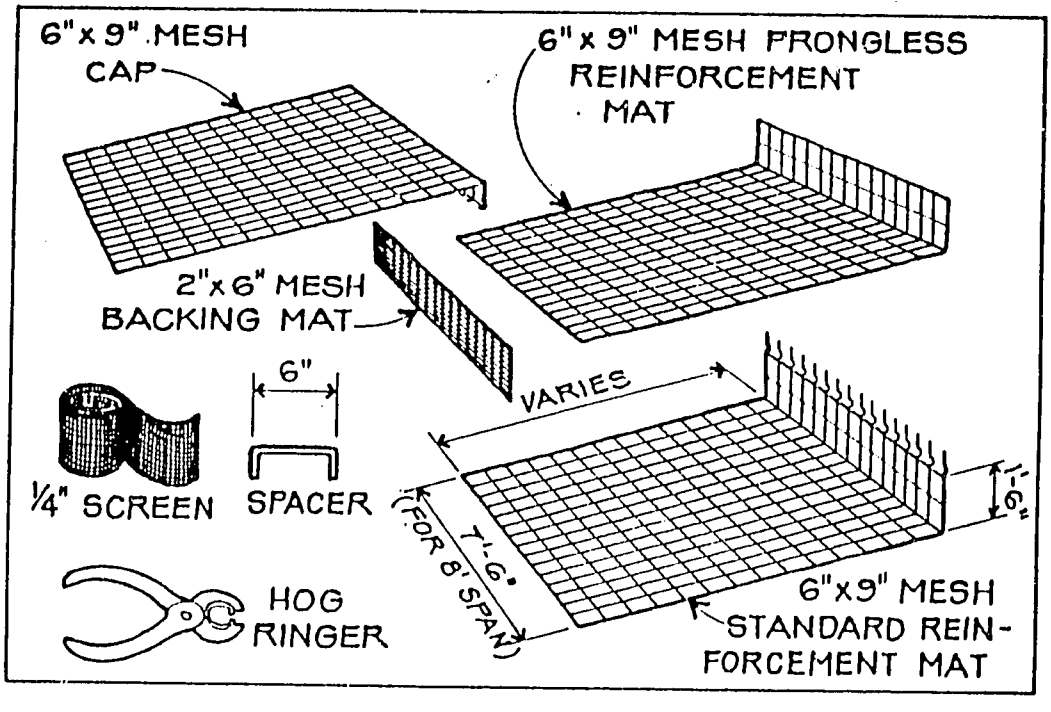

Fig. 59 Accessories Used for the Construction of the Welded Wire Wall (after Hilfiker Co., 1988)

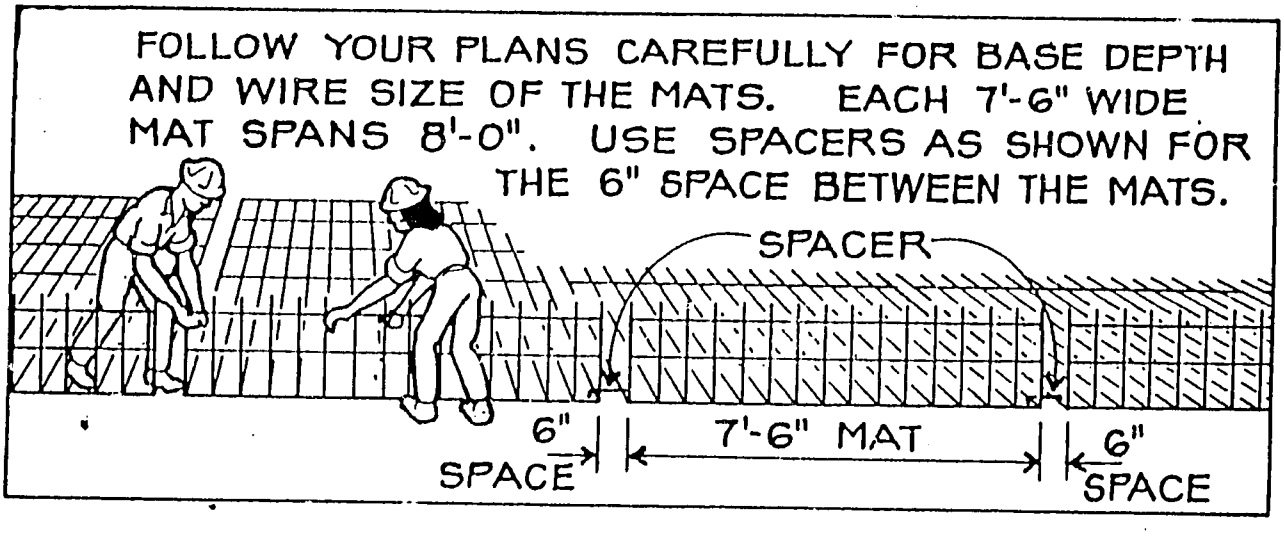

Fig. 60 Welded Wire Mat Layout Showing the 6" Spacers (after Hilfiker Co., 1988)

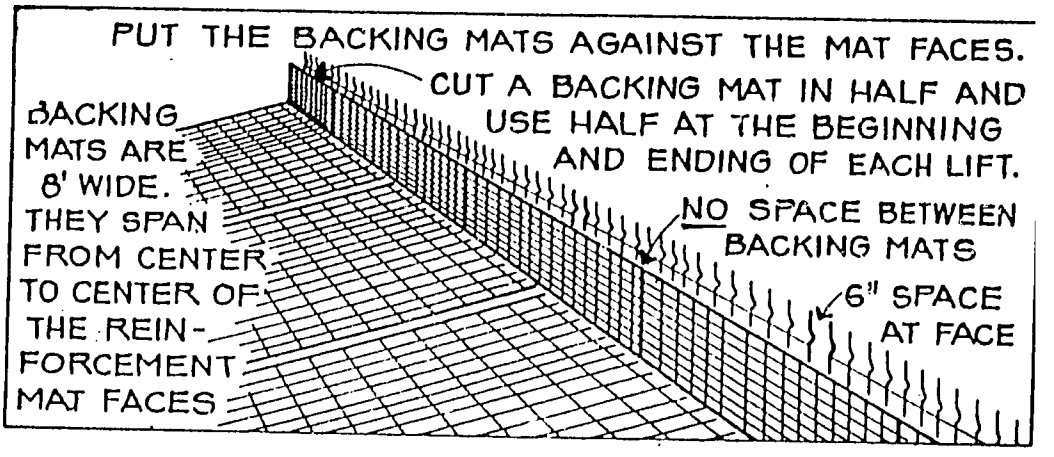

Fig. 61 Placement of the Backing Mats Against the Face the Wall (after Hilfiker Co., 1988)

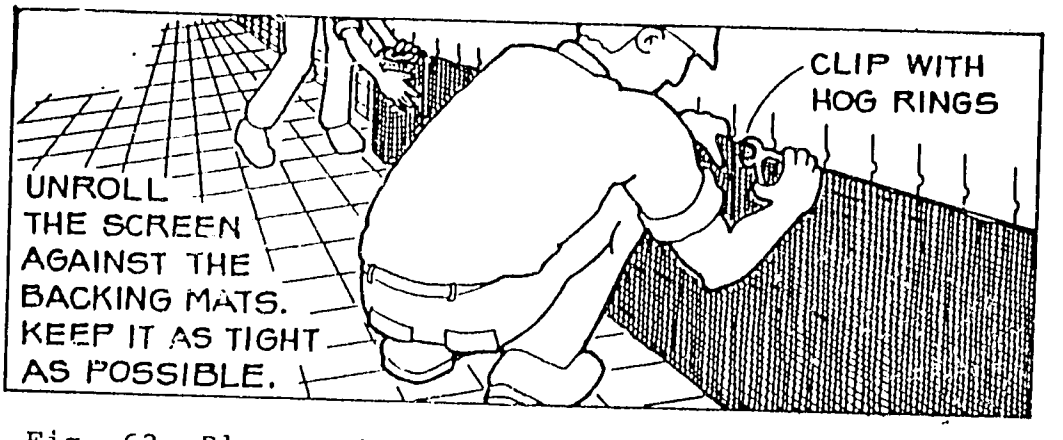

Fig. 62 Placement of the Screen with Hog Rings (after Hilfiker Co., 1988)

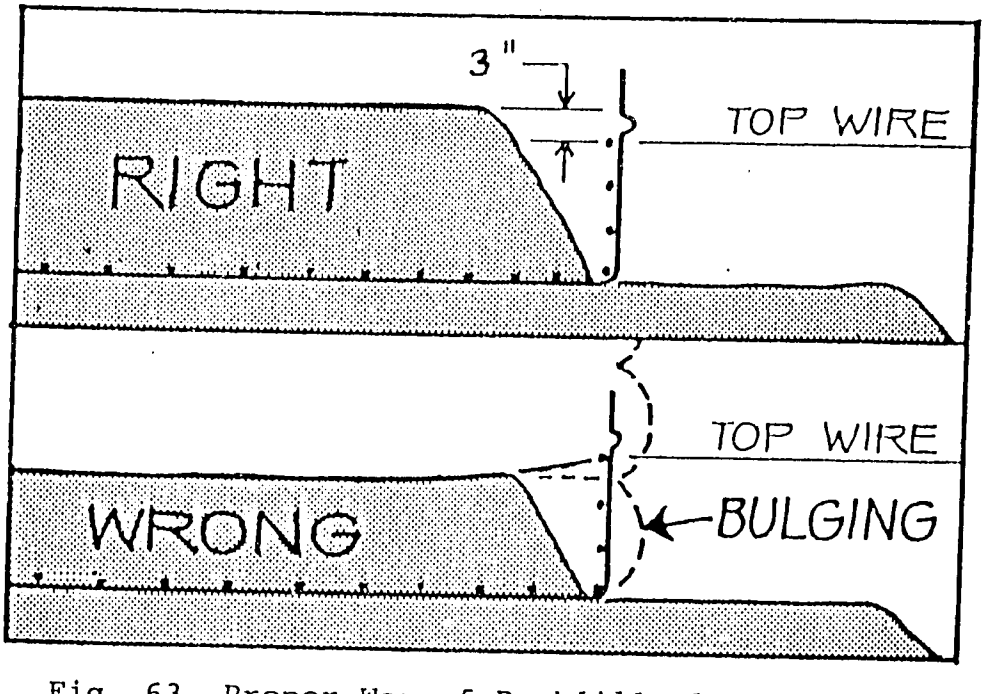

Fig. 63 Proper Way of Backfill Placement (after Hilfiker Co., 1988)

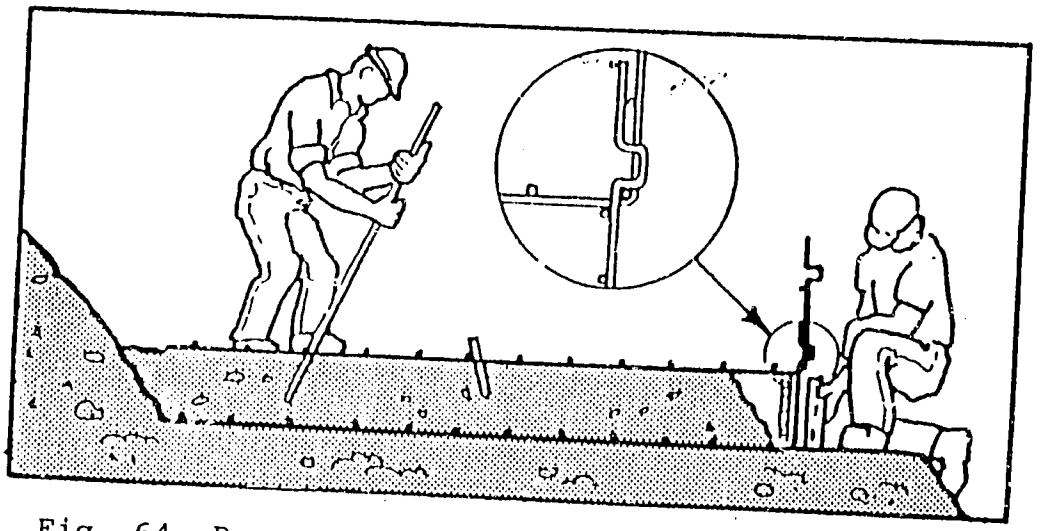

Fig. 64 Proper Placement of Two Succeeding Mats (after Hilfiker Co., 1988)

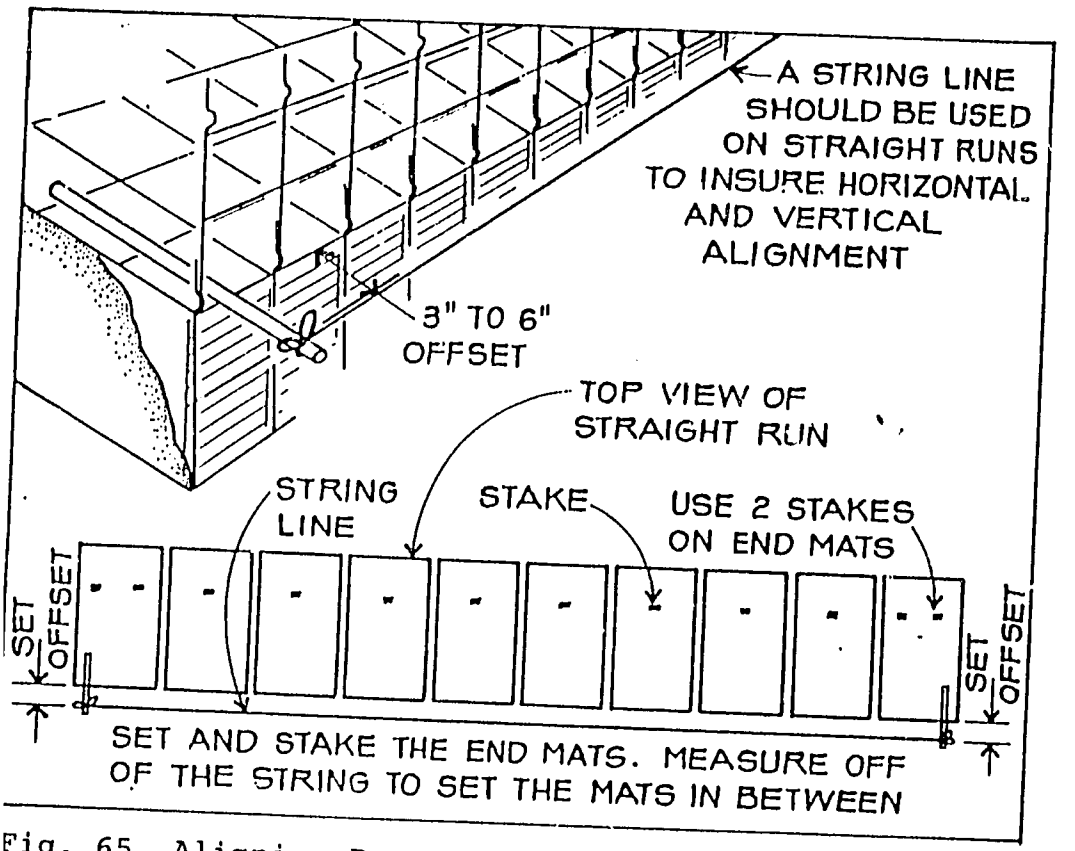

Fig. 65 Aligning Procedure for the Welded Wire Mats (after Hilfiker Co., 1988)

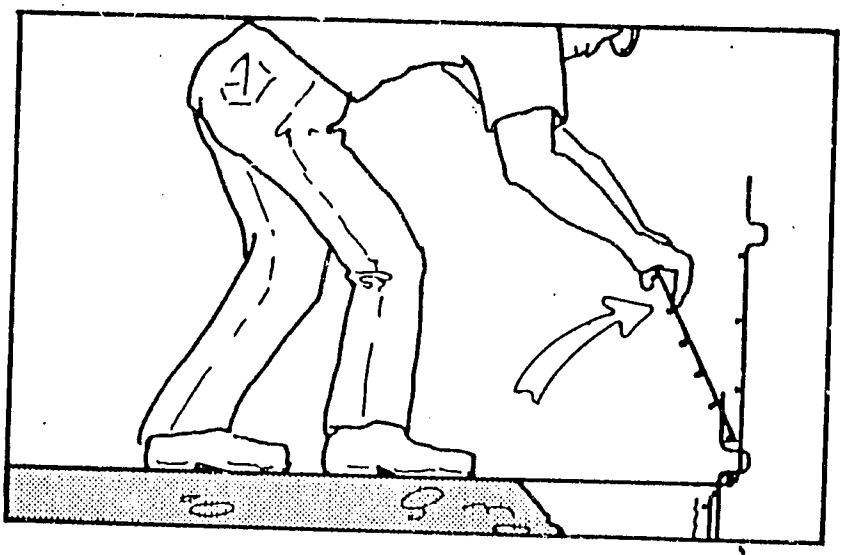

Fig. 66 Placement of Backing Mats for Succeeding Layers Other than the First Layer (after Hilfiker Co., 1988)

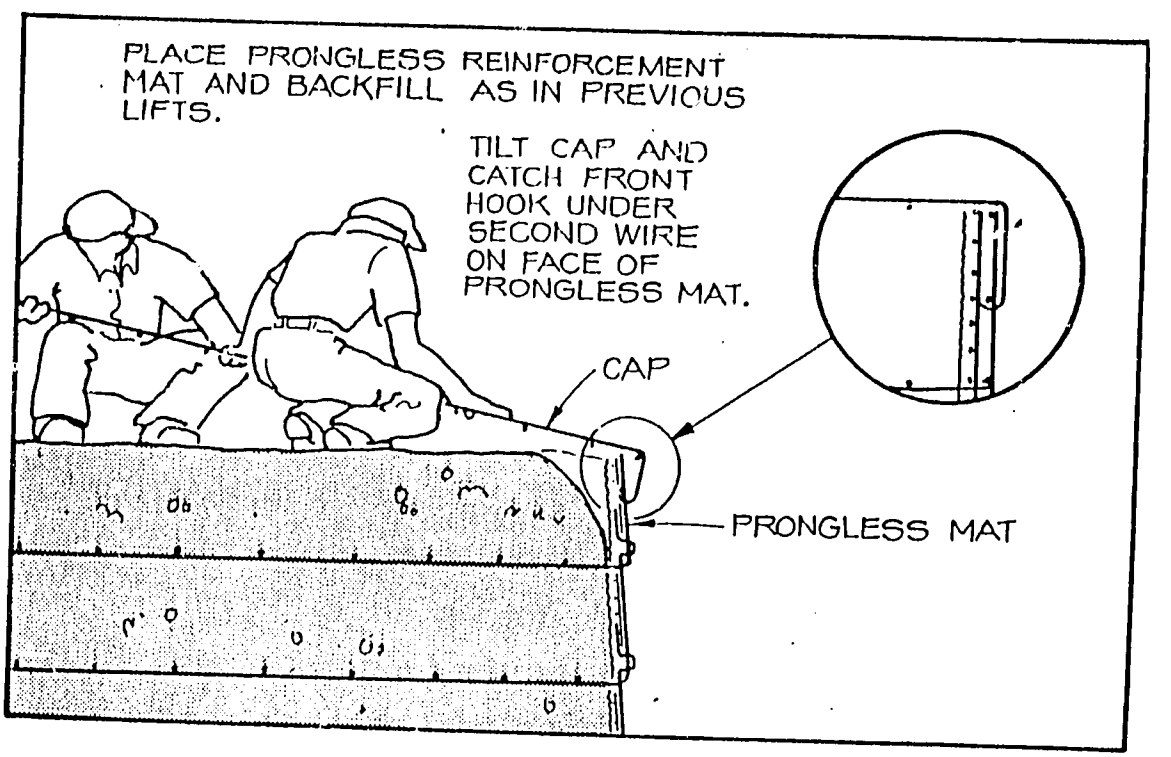

Fig. 67 Installation of the Prongless Reinforcing Mat and the Top Cap in the Topmost Layer of the Wall (after Hilfiker Co., 1988)

(a)

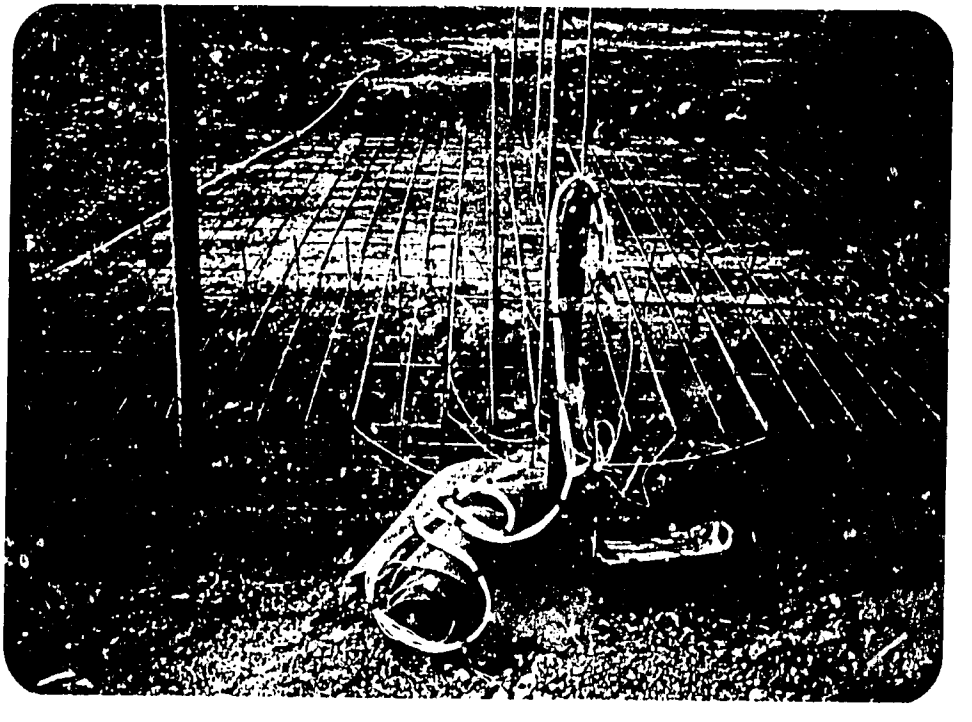

(b)

Fig. 68 a) Experimental Site of the Welded Wire Wall Just After the Installation of the Subsoil Instruments
b) Photograph of the Site of Welded Wire Wall Taken During the Placement of the First Layer of Reinforcing Mats

(a)

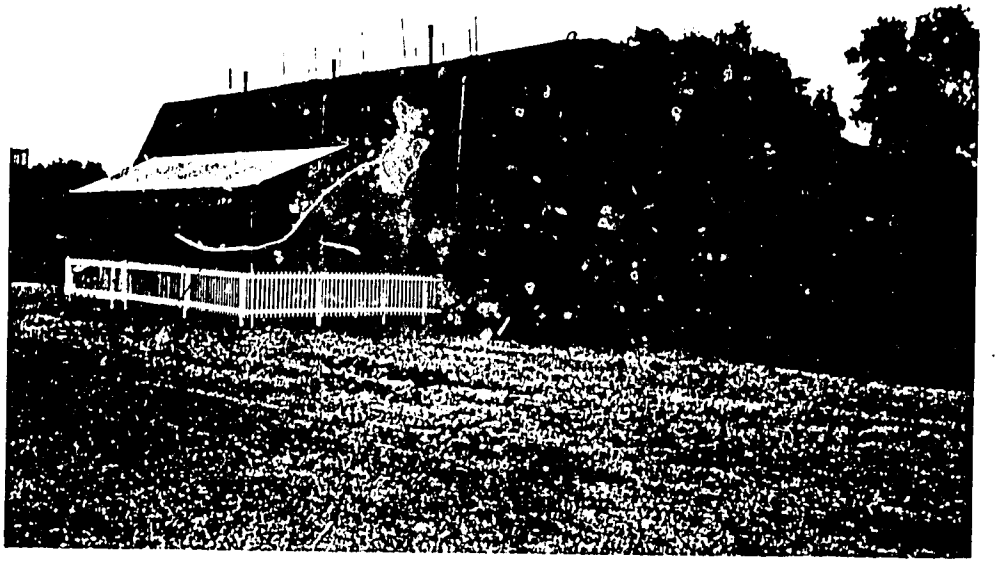

(b)

Fig. 69 Welded Wire Wall After Laying Out the Fourth Layer
b) Photograph Showing the Completed View of the Welded Wire Wall

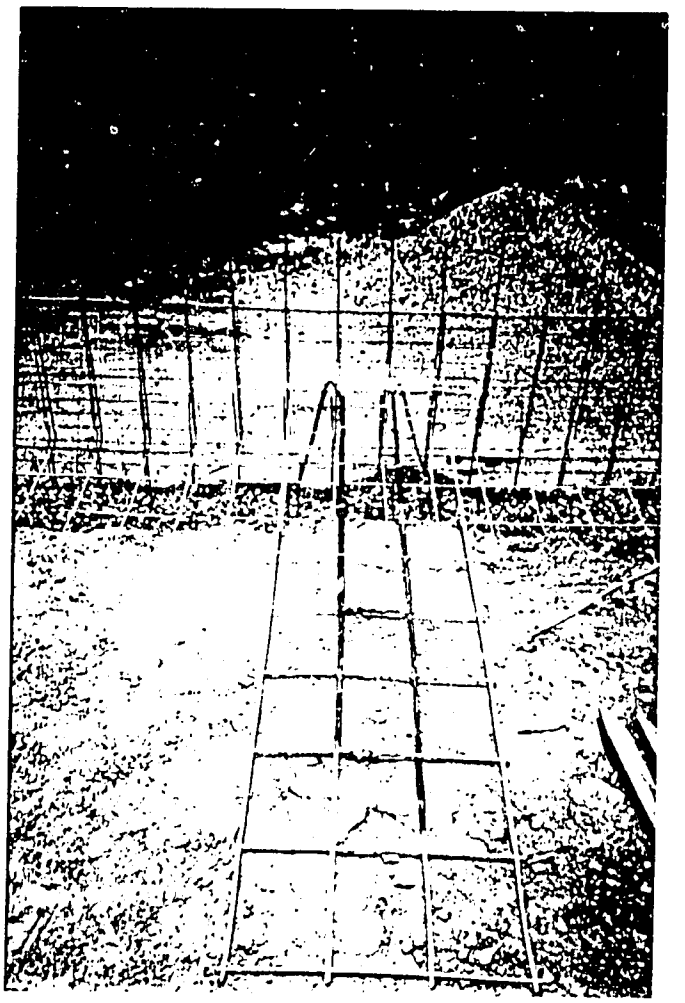

(a)

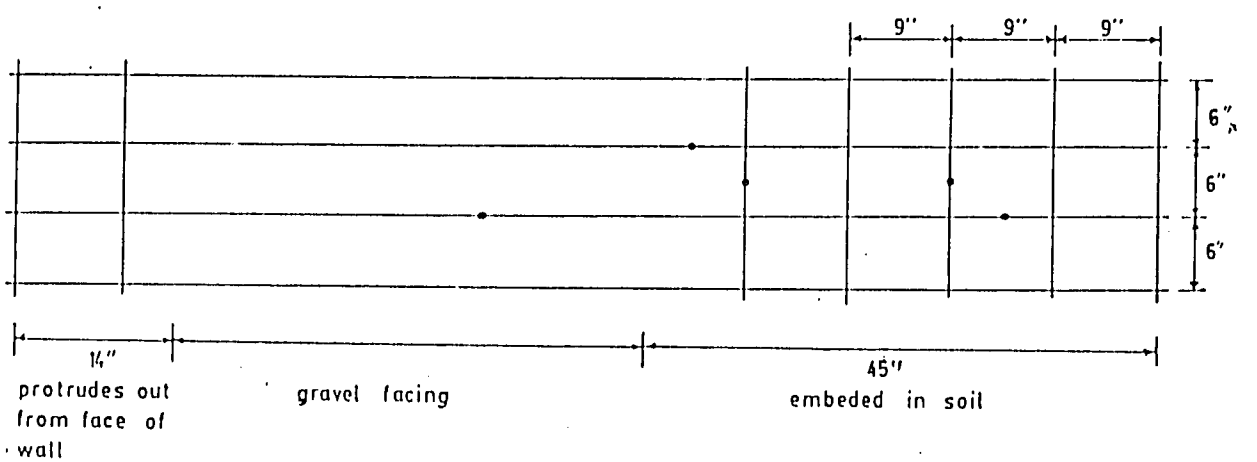

(b)

Fig. 70 a) Photograph Showing the Dummy Mat for Pullout Test Laid in Place
b) Schematic Diagram of the Dummy Mat Showing Location of Instrumentation Points

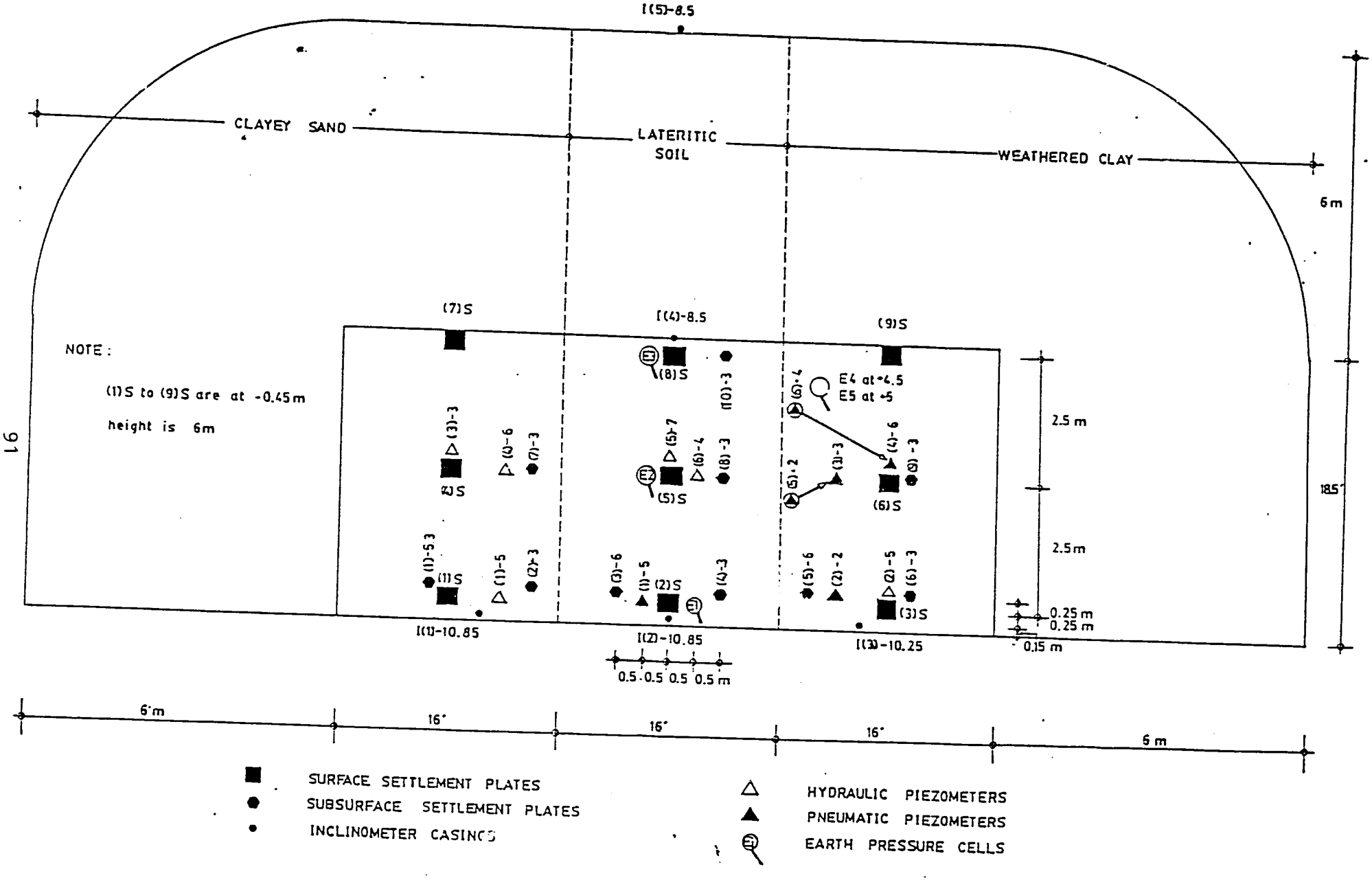

Fig. 71 Schematic Layout of Field Instrumentation for the Welded Wire Wall

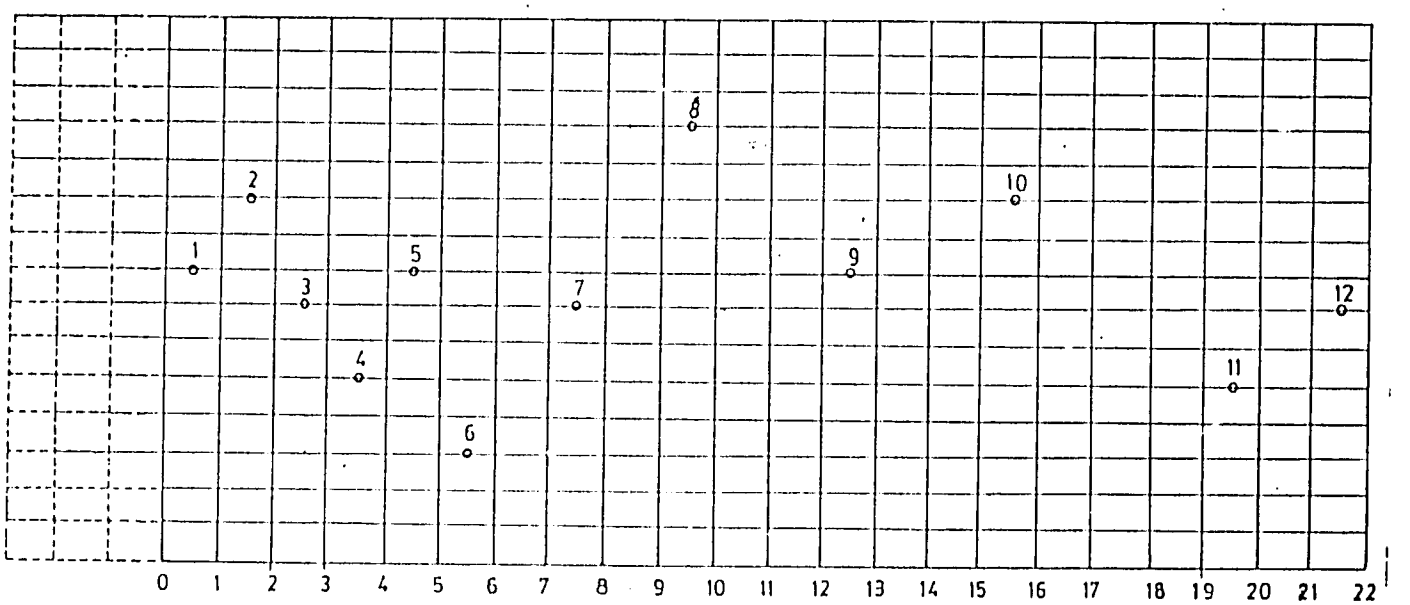

Fig. 72 Location of Strain Gages Along the Welded Wire Mat for the Bottom Four Instrumented Layers

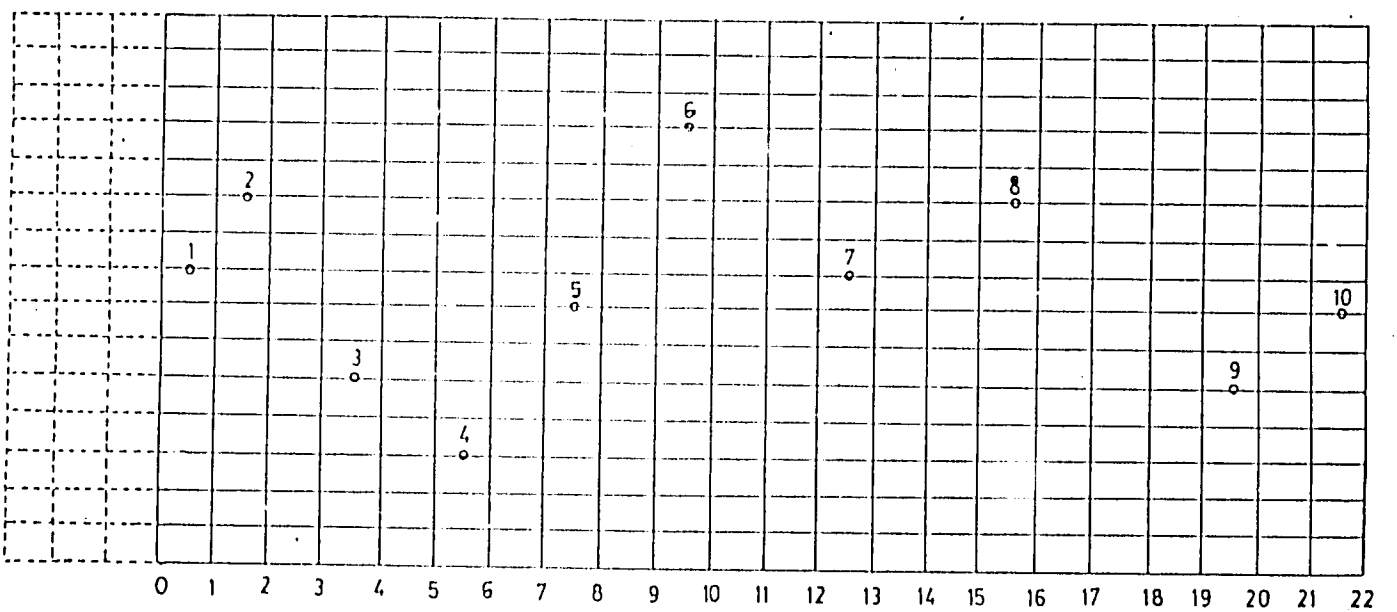

Fig. 73 Strain Gage Locations Along the Welded Wire Mat for the Top Three Instrumented Layers

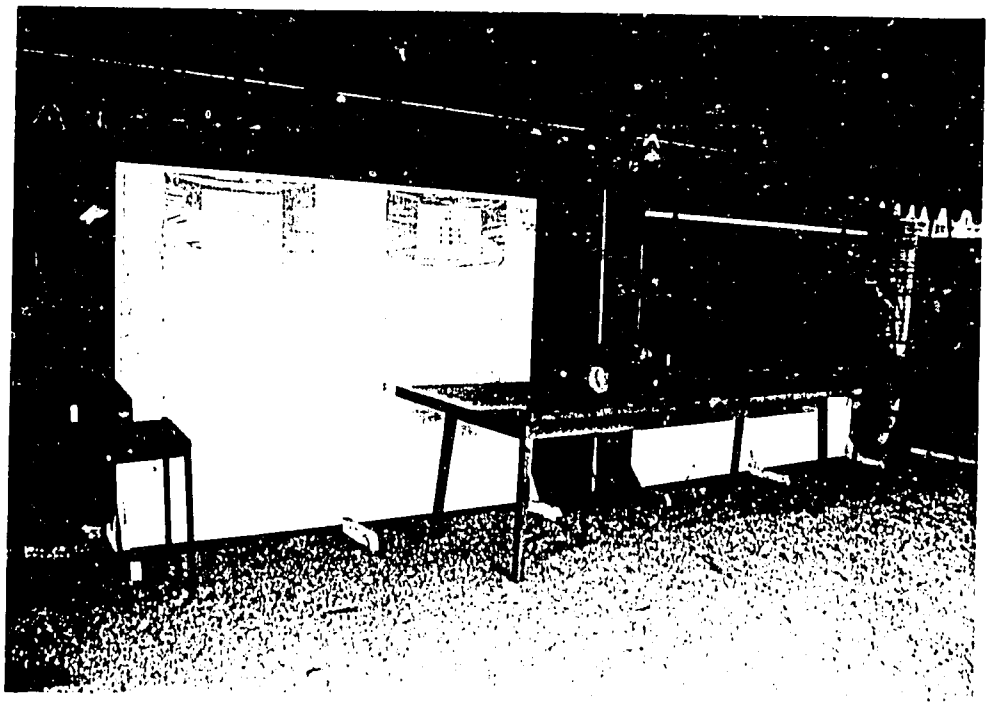

(a)

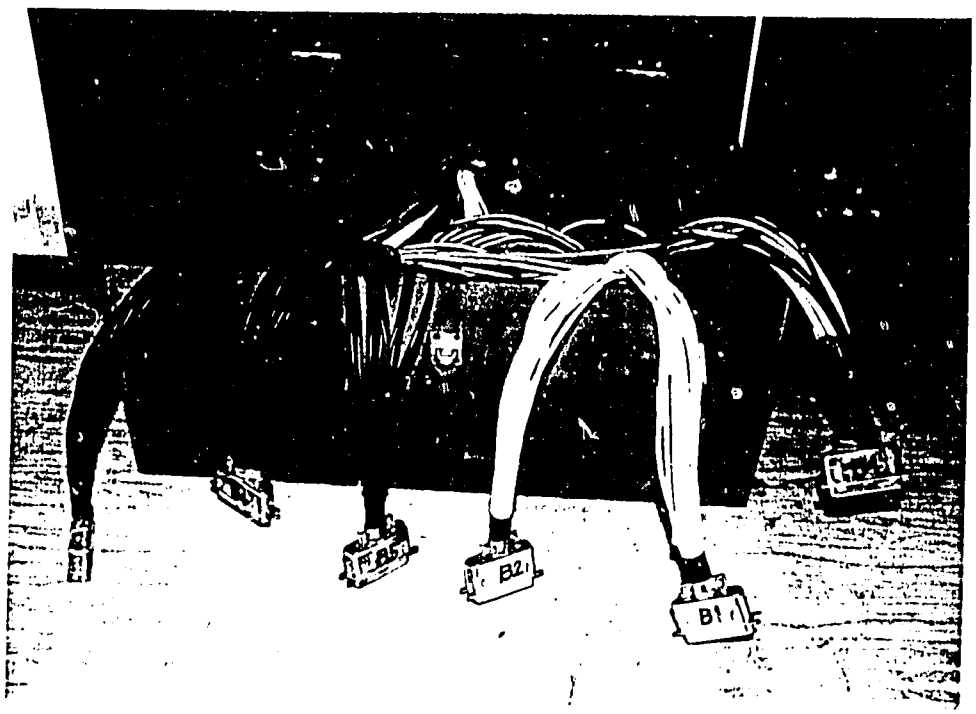

(b)

Fig. 74 a) Monitoring Station Located Just in Front of the Welded Wire Wall Showing the Boxes for the Quick-connect Plugs Connected to the Strain Gages
b) Close-Up View of the Bundled Lead Wires with Connecting Plugs for Tension Measurement

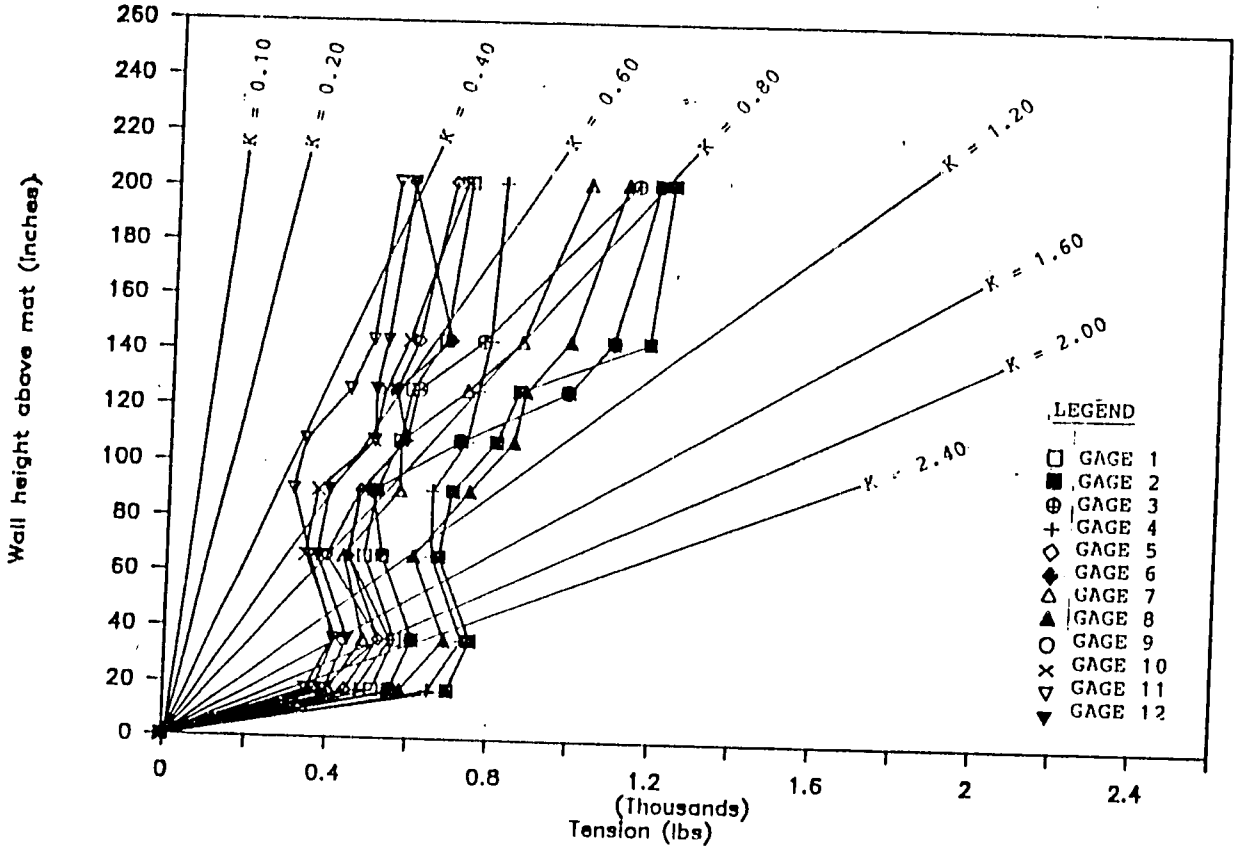

(a)

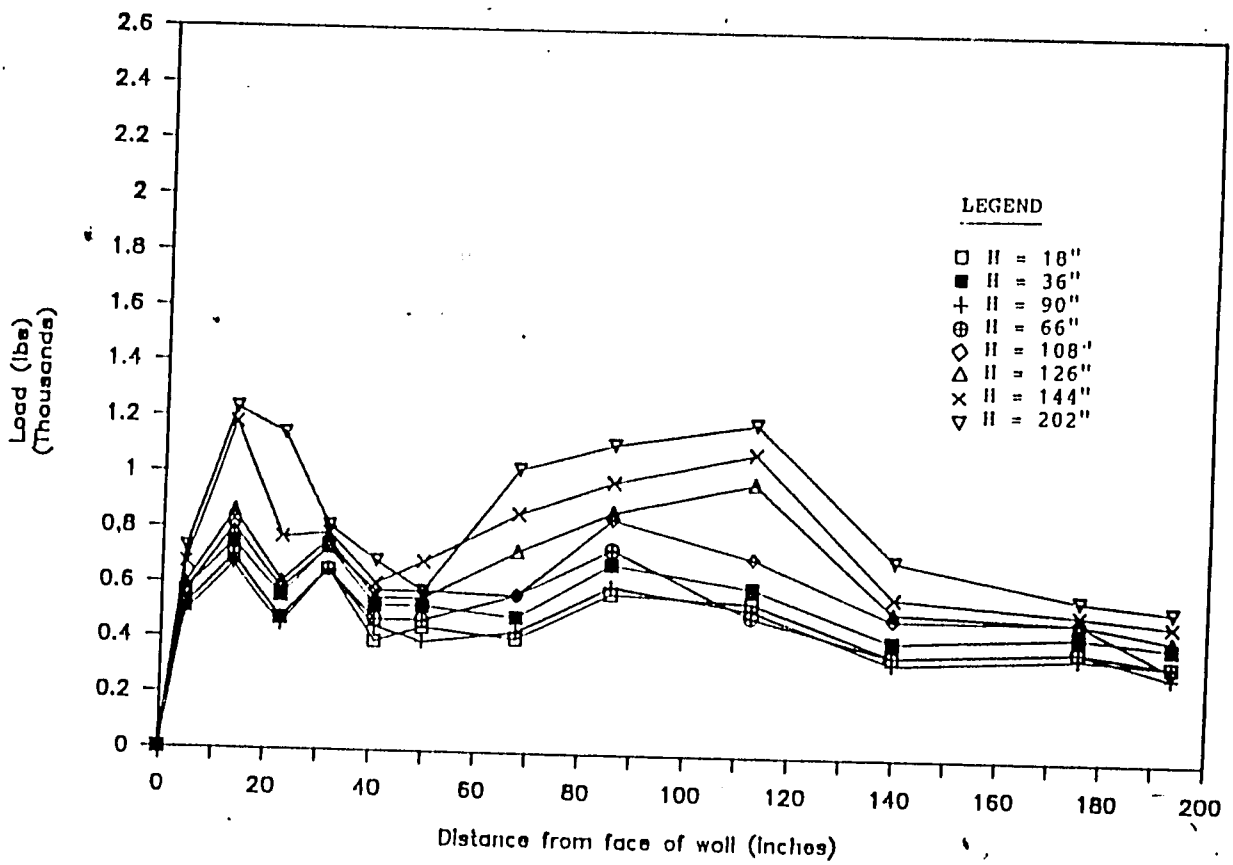

(b)

Fig. 75 a) Plot of Tension Against Wall Height Above Mat for Clayey Sand (Mat No. 2)
b) Plot of Tension Against Distance from the Face of the Wall for Clayey Sand (Mat No. 2)

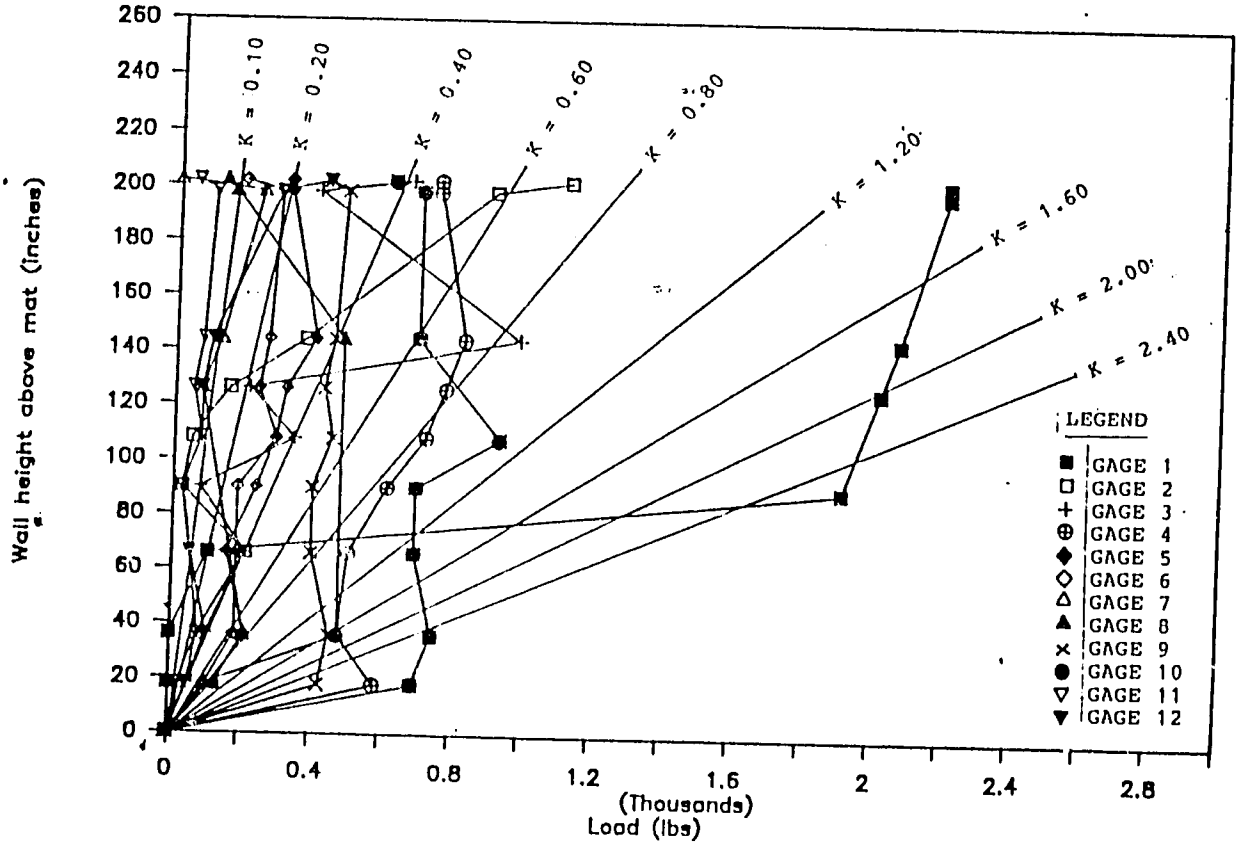

(a)

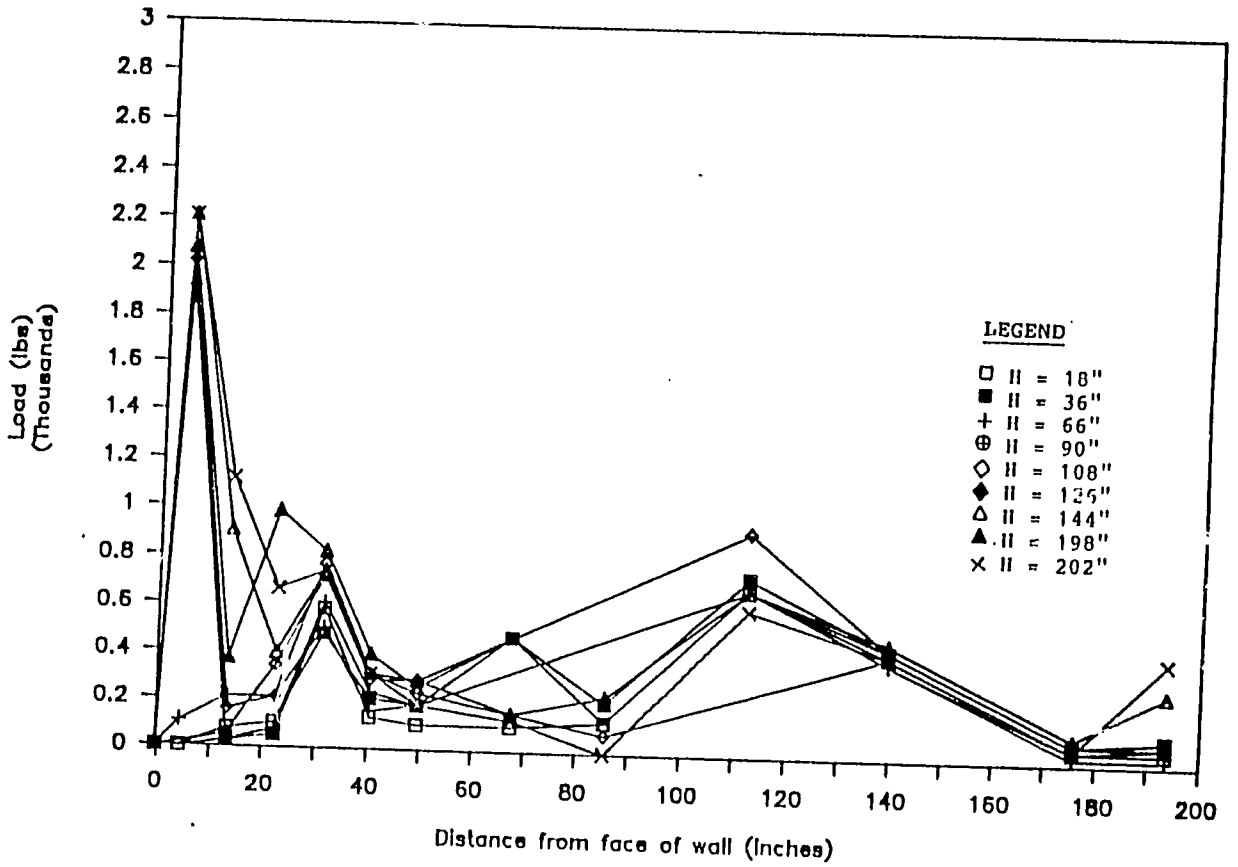

(b)

Fig. 76 a) Plot of Tension Against Wall Height Above Mat for Lateritic Residual Soil (Mat No. 2)
b) Plot of Tension Against Distance from the Face of the Wall for Lateritic Residual Soil (Mat No. 2)

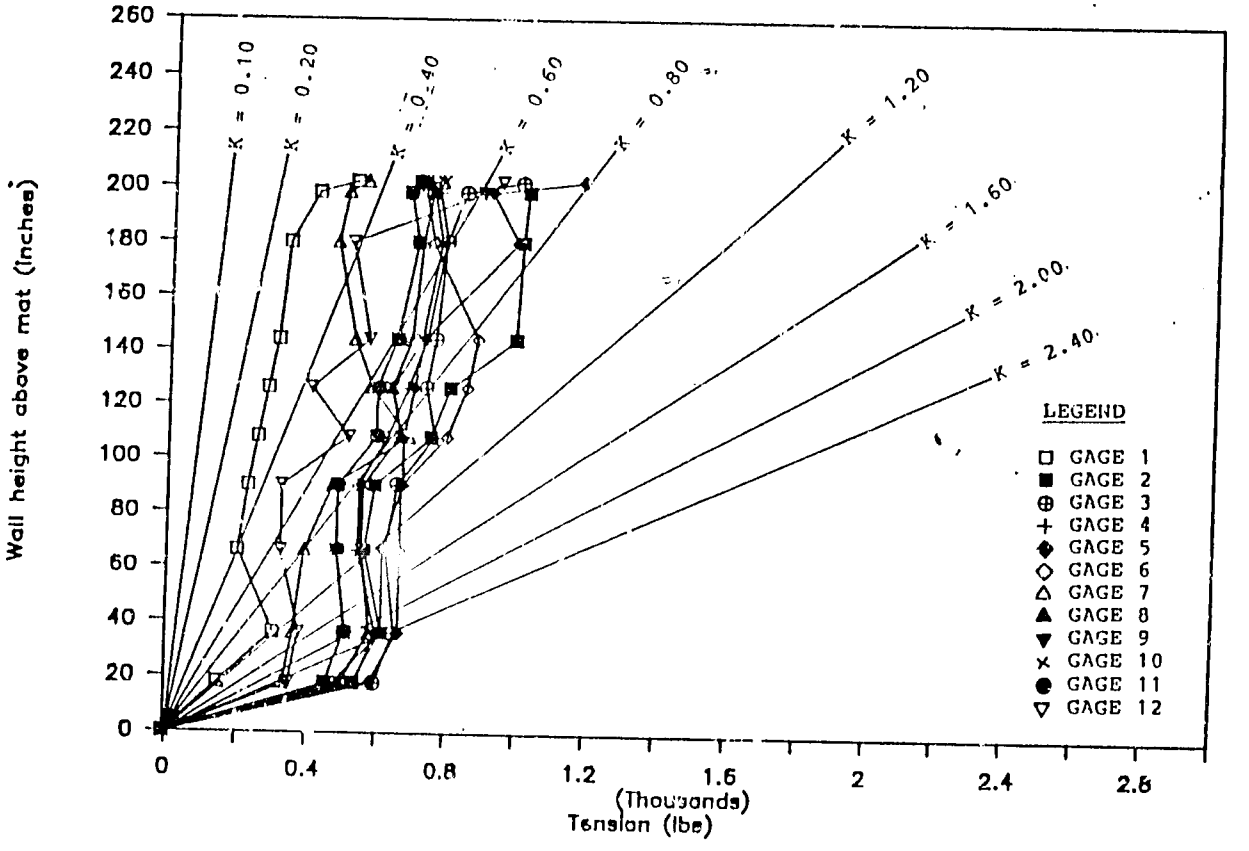

(a)

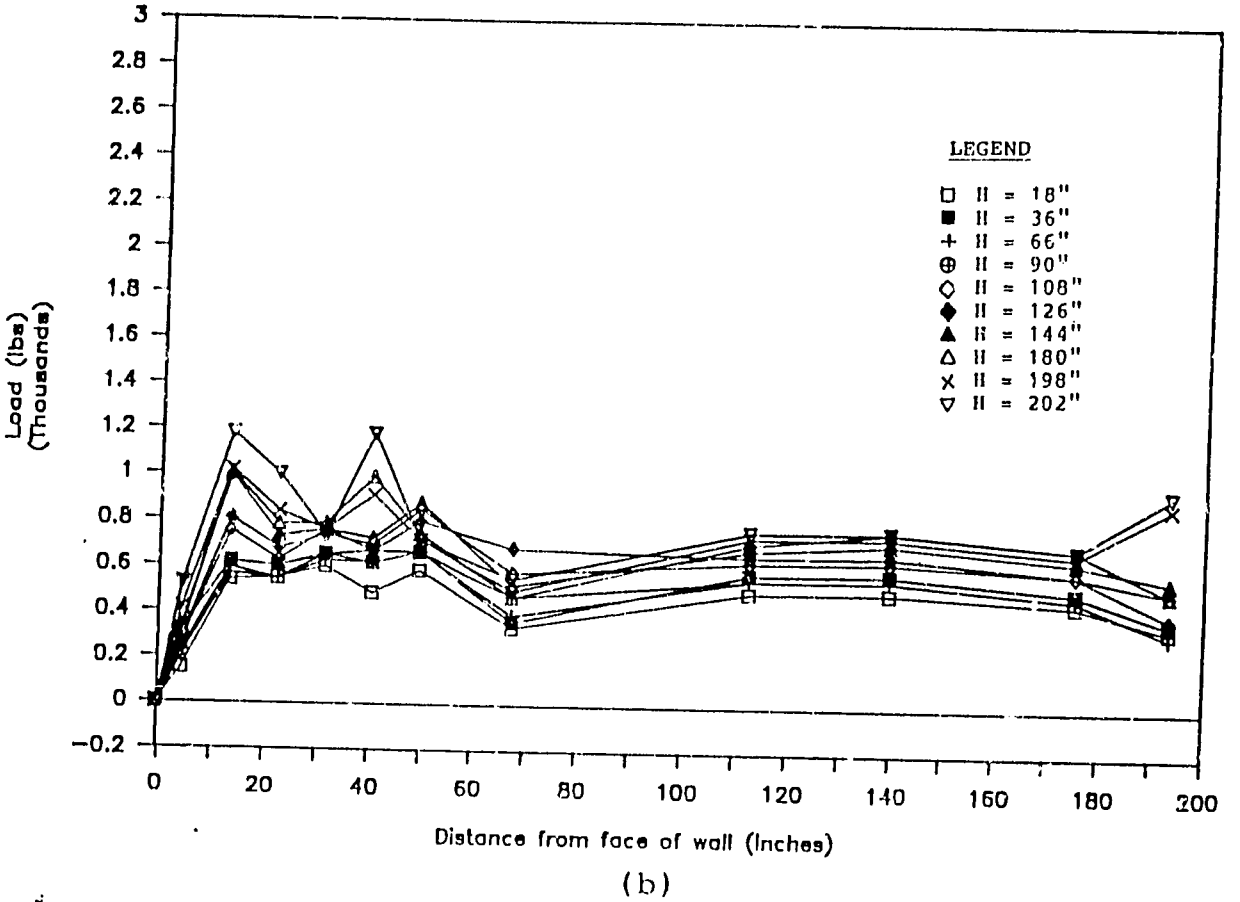

(b)

Fig. 77 a) Plot of Tension Against Wall Height Above Mat for Weathered Clay (Mat No. 2)
b) Plot of Tension Against Distance from the Face of the Wall for Weathered Clay (Mat No. 2)

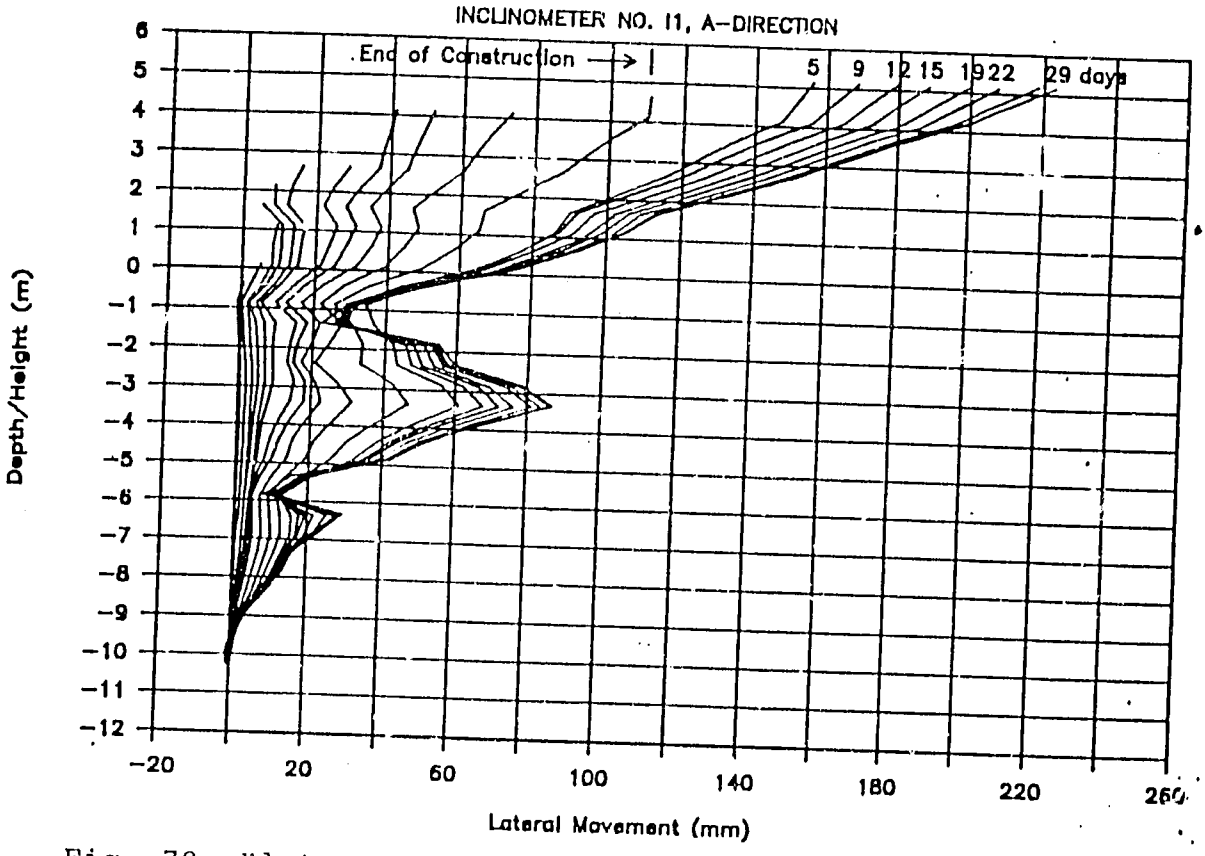

Fig. 78 Plots of Depth/Height Against Lateral Movement for Inclinometer No. 1

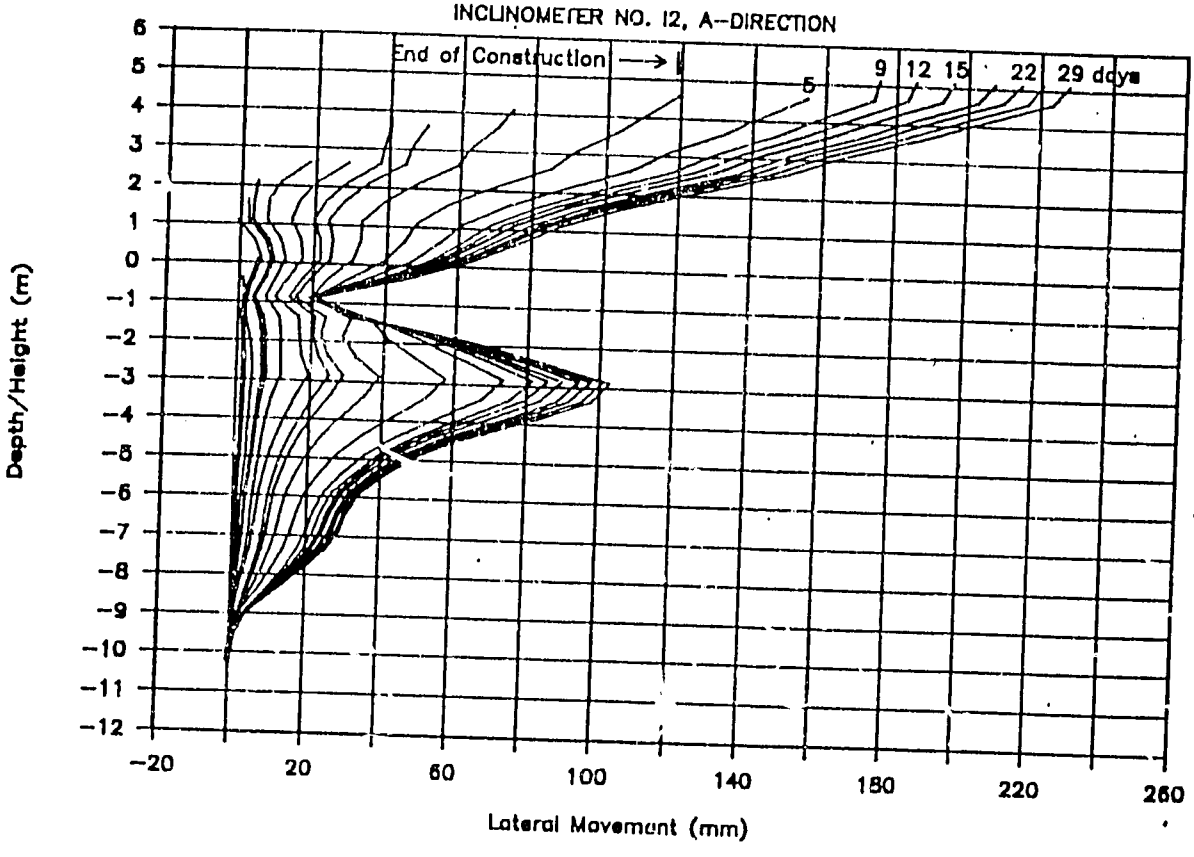

Fig. 79 Plots of Depth/Height Against Lateral Movement for Inclinometer No. 2

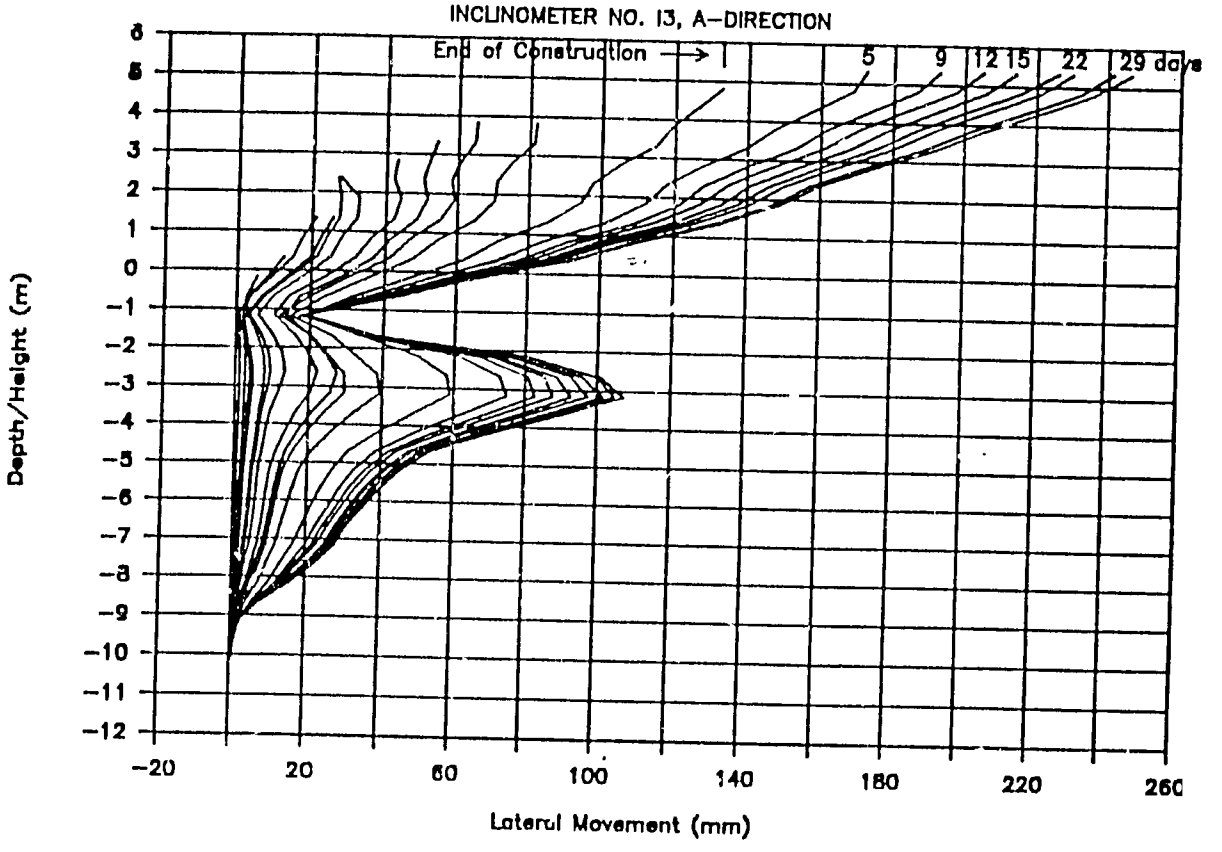

Fig. 80 Plots of Depth/Height Against Lateral Movement for Inclinometer No. 3

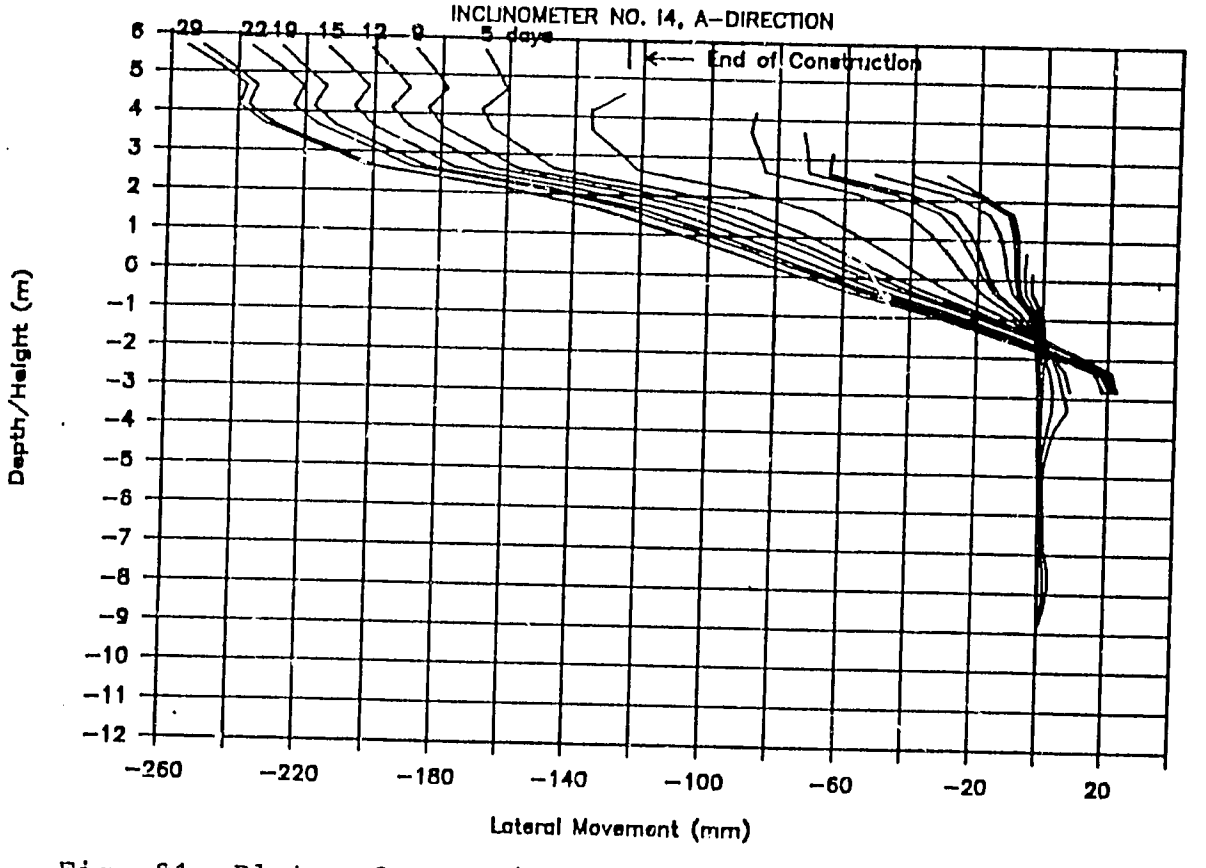

Fig. 81 Plots of Depth/Height Against Lateral Movement for Inclinometer No. 4

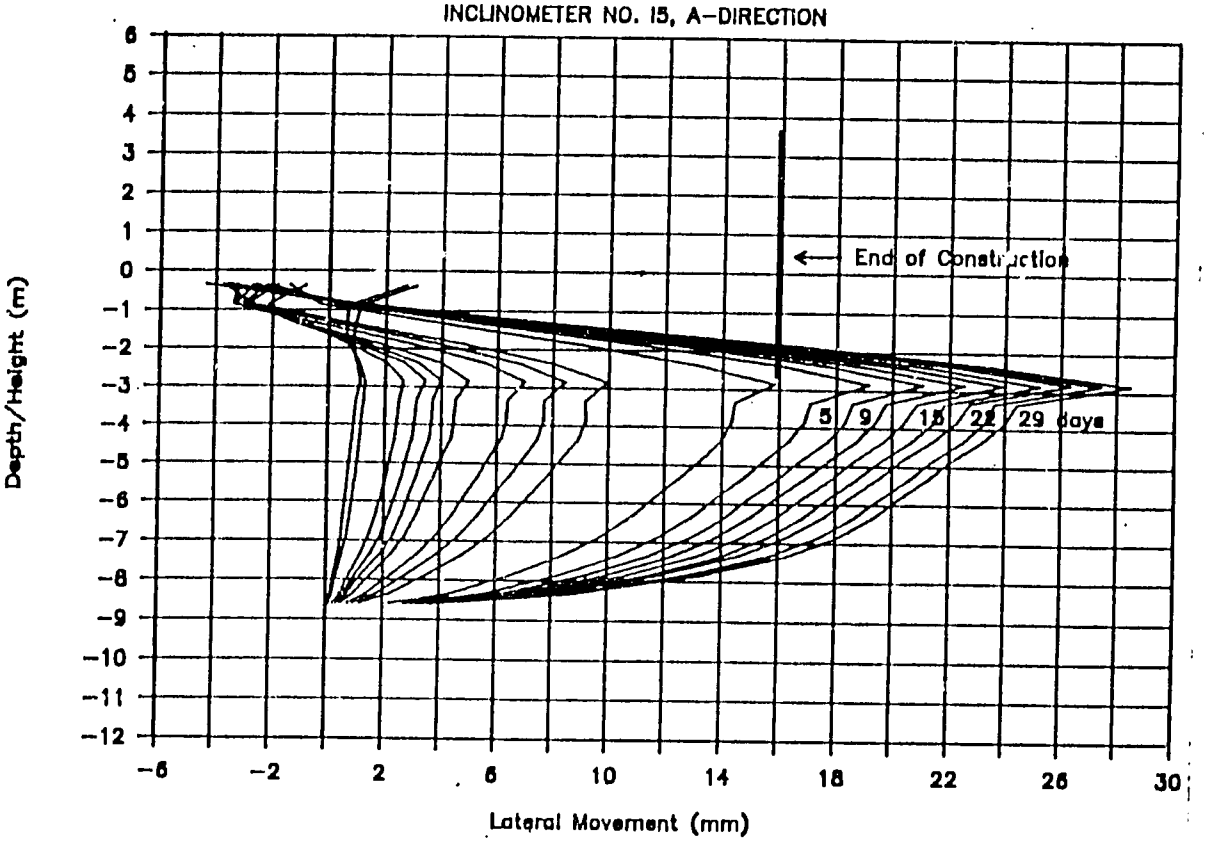

Fig. 82 Plots of Depth/Height Against Lateral Movement for Inclinometer No. 5

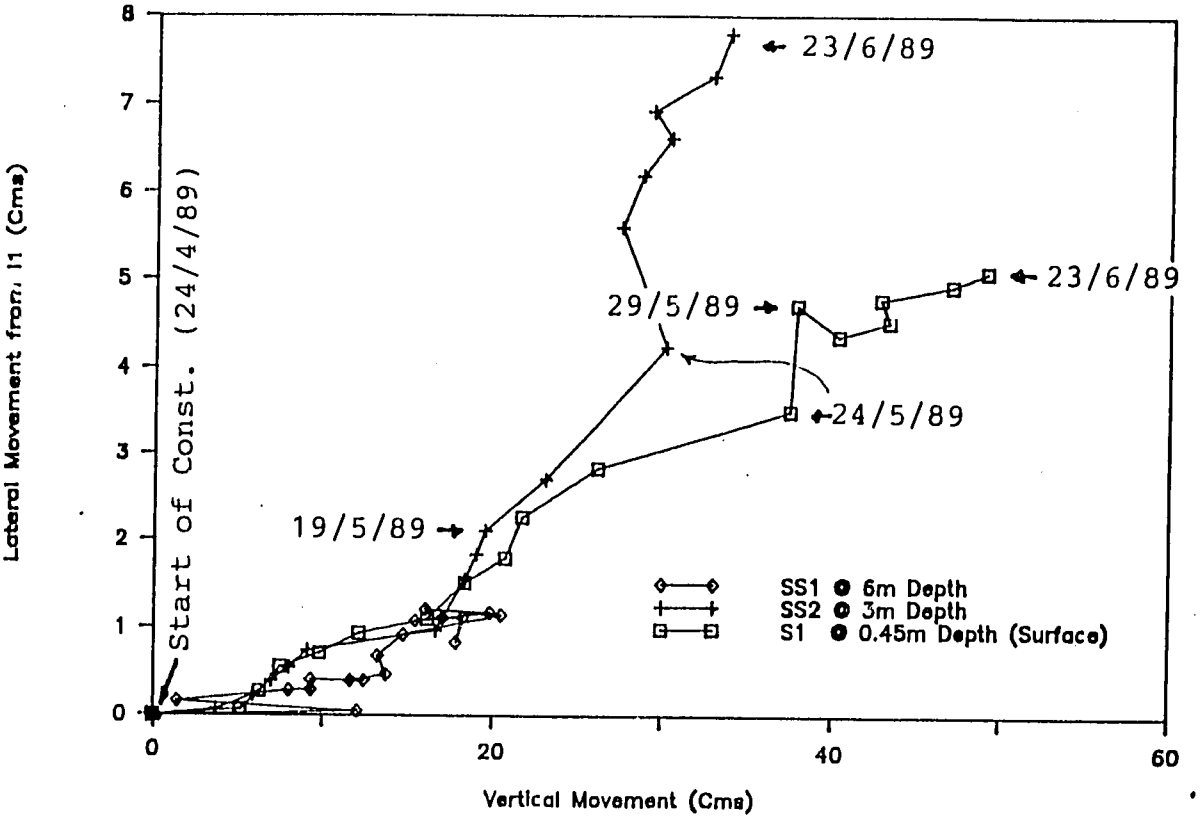

Fig. 83 Lateral Movement Plotted Against the Vertical Movement of Wall (Inclinometer No. 1)

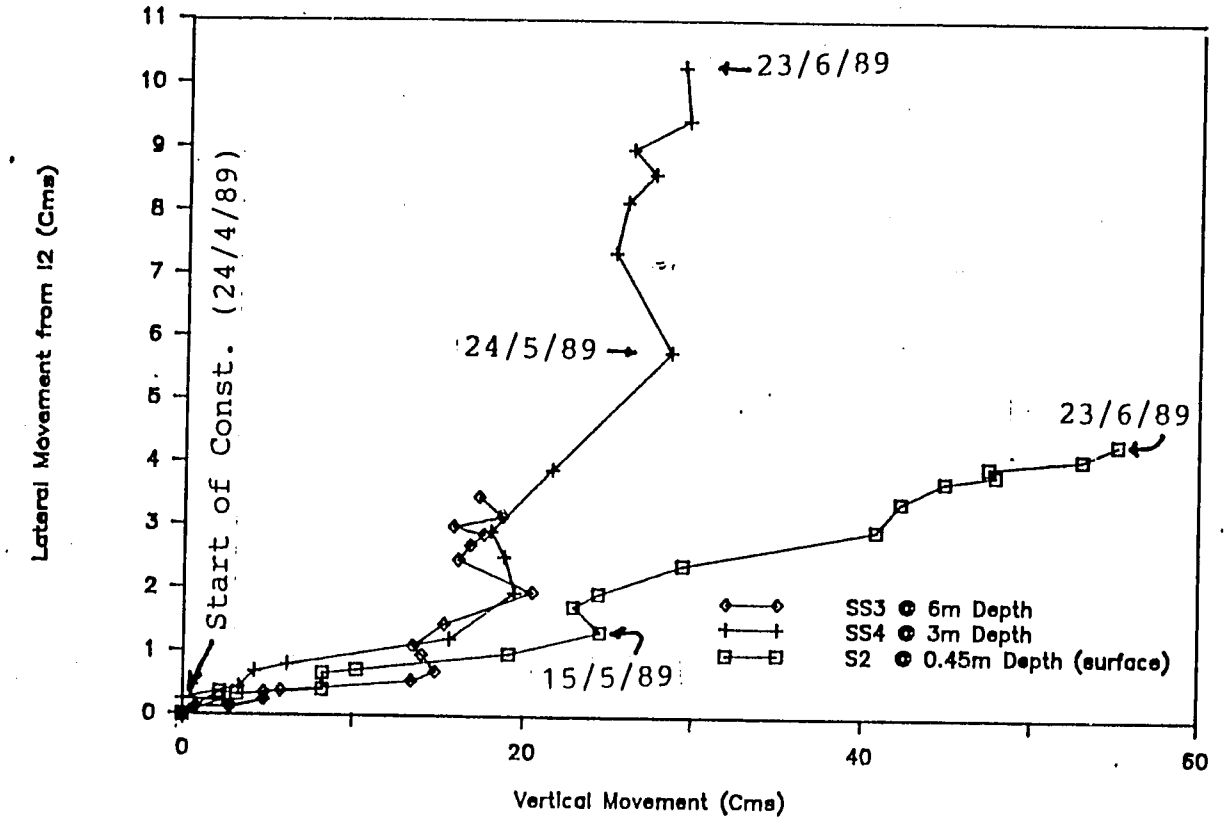

Fig. 84 Lateral Movement Plotted Against the Vertical Movement of Wall (Inclinometer No. 2)

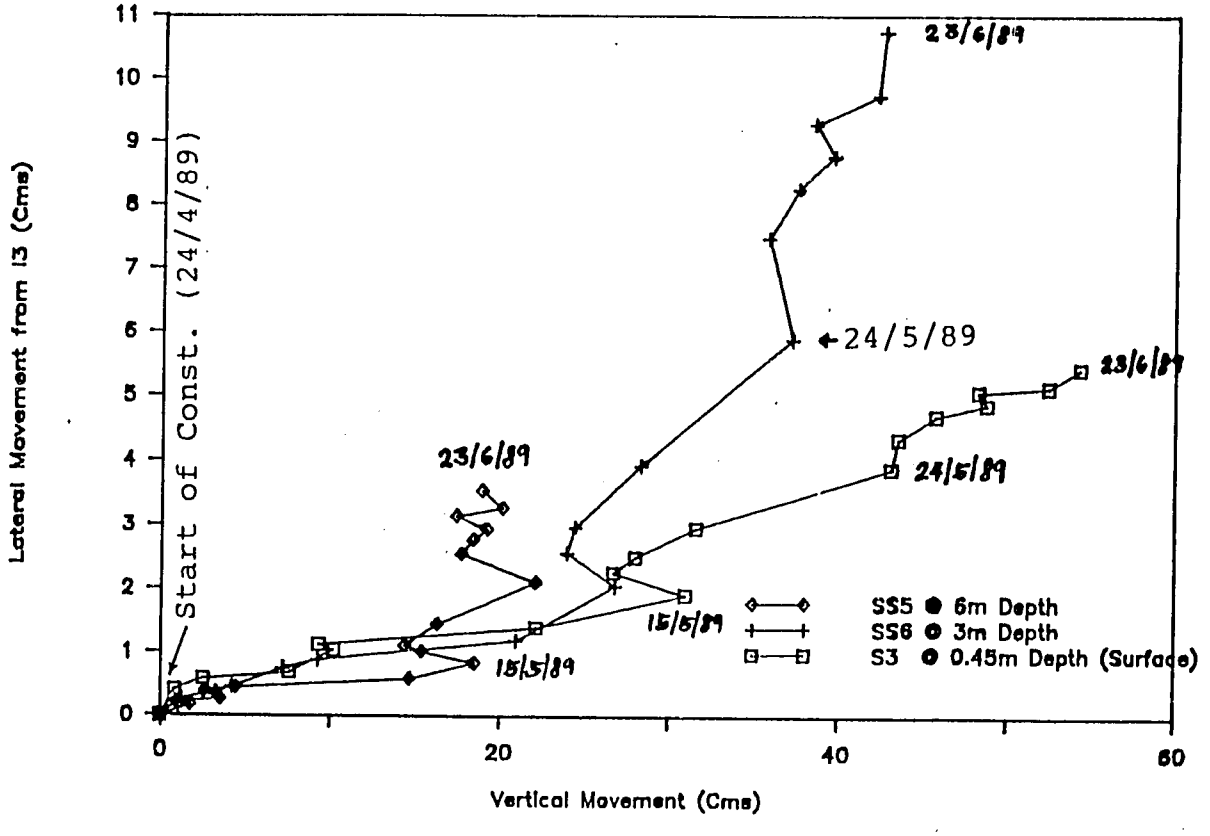

Fig. 85 Lateral Movement Plotted Against the Vertical Movement of Wall (Inclinometer No. 3)

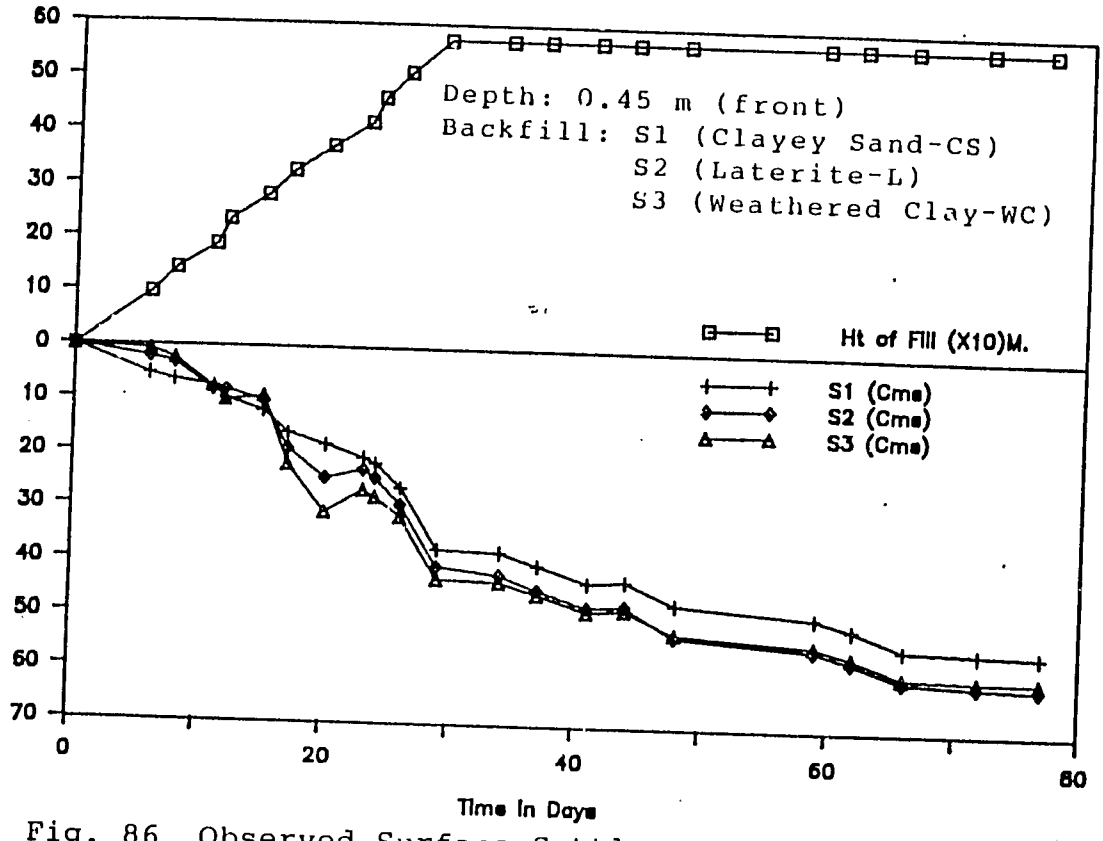

Fig. 86 Observed Surface Settlements from the Front Settlement Plates Near the Face of the Wall (S1 to S3)

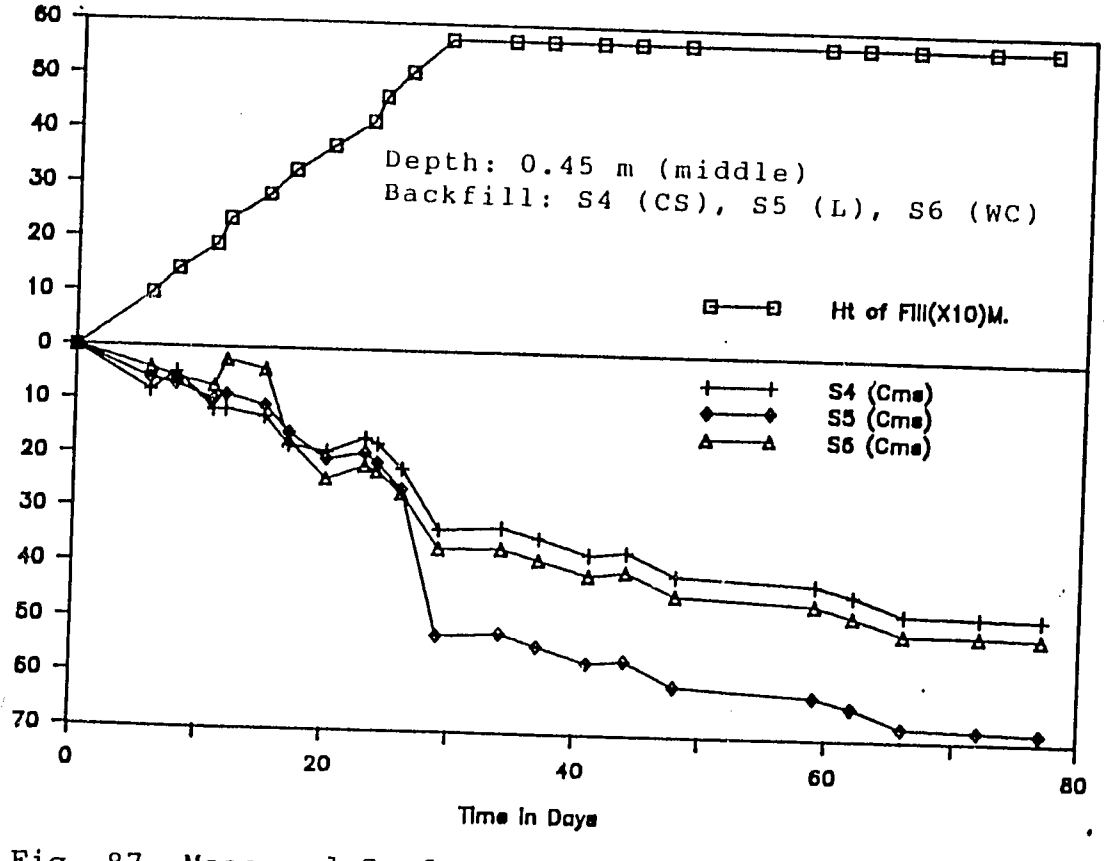

Fig. 87 Measured Surface Settlements at the Center of Each Section of the Wall (S4 to S6)

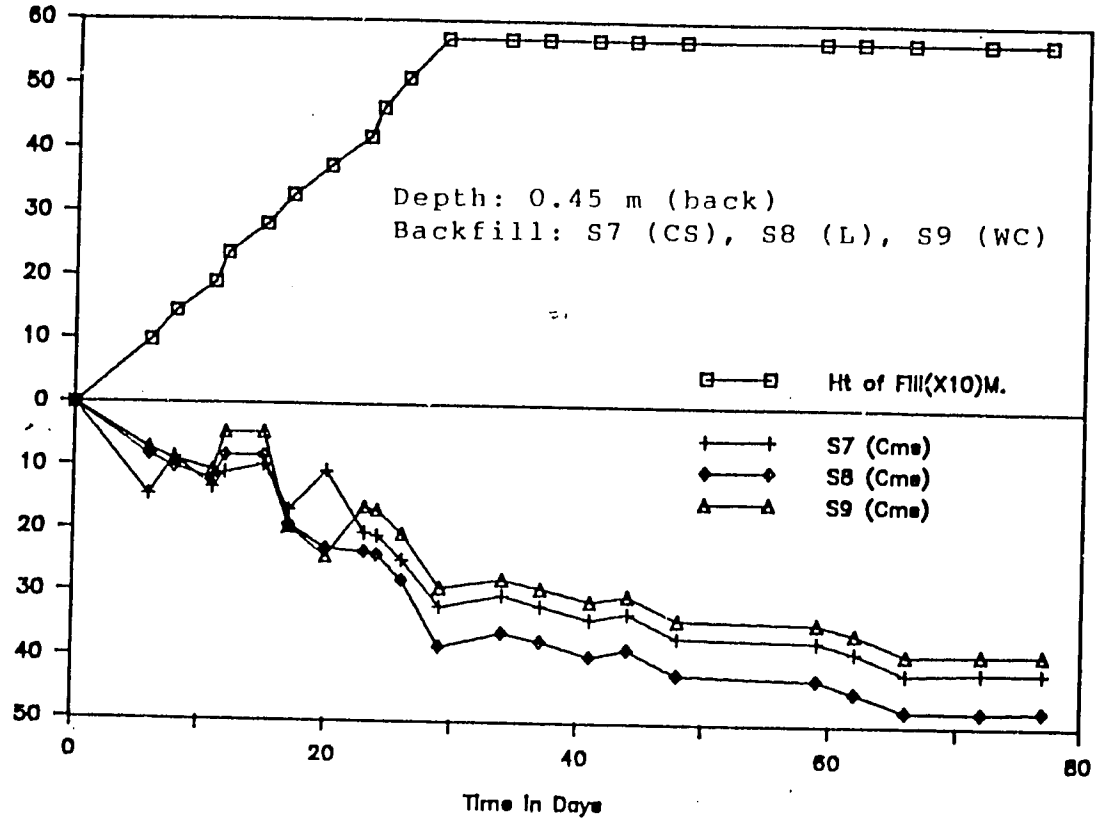

Fig. 88 Observed Surface Settlements at the Back Sections of the Wall (S7 to S9)

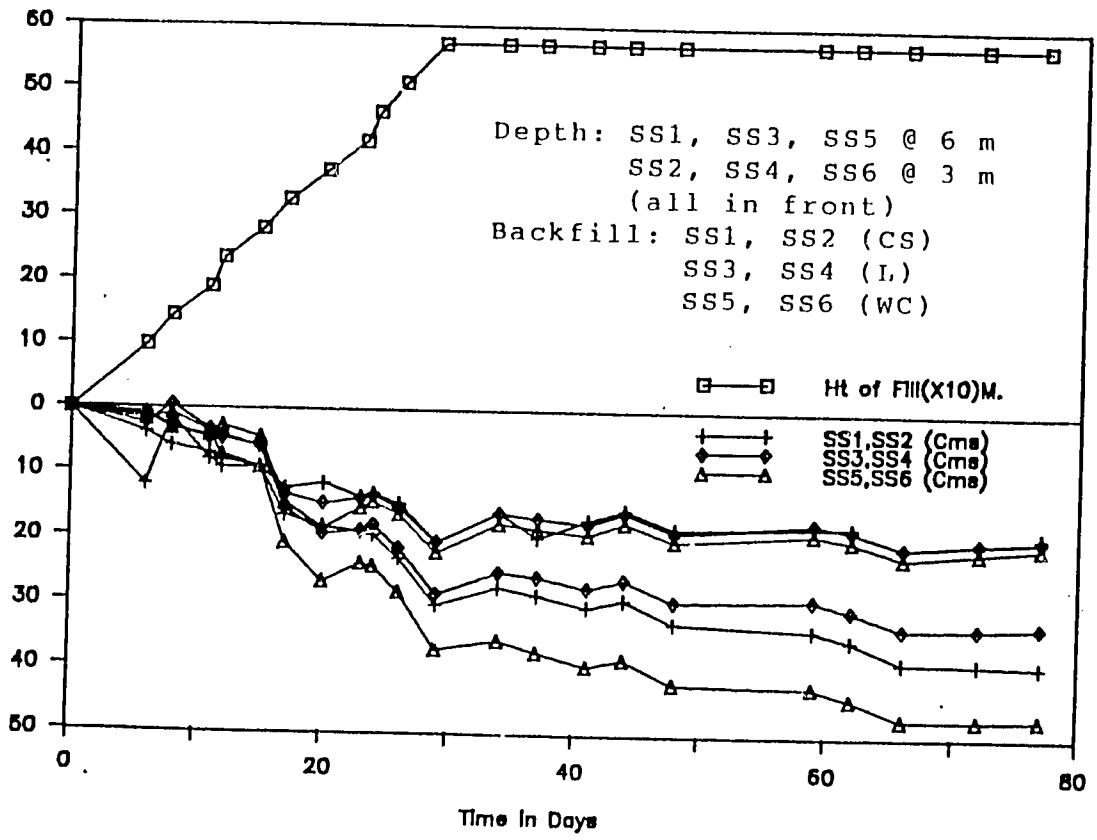

Fig. 89 Observed Subsurface Settlements of the Soft Clay Foundation (SS1 to SS6)

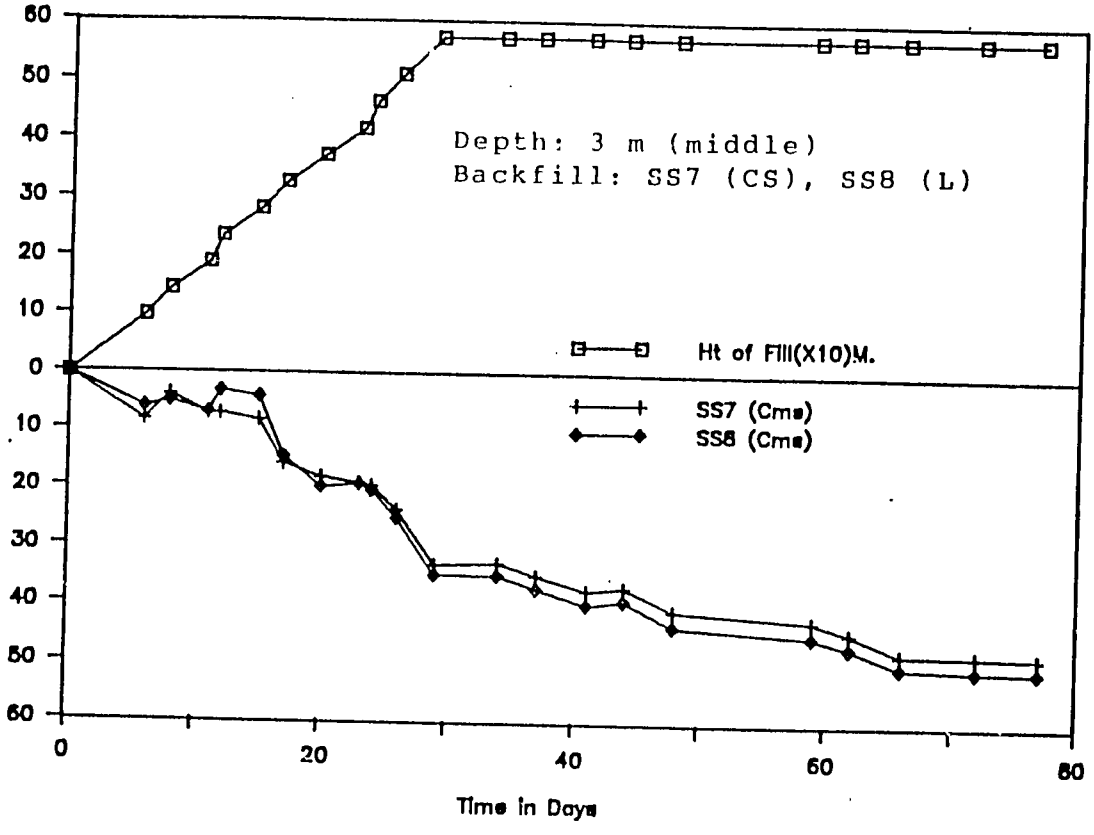

Fig. 90 Observed Subsurface Settlements (SS7 and SS8)

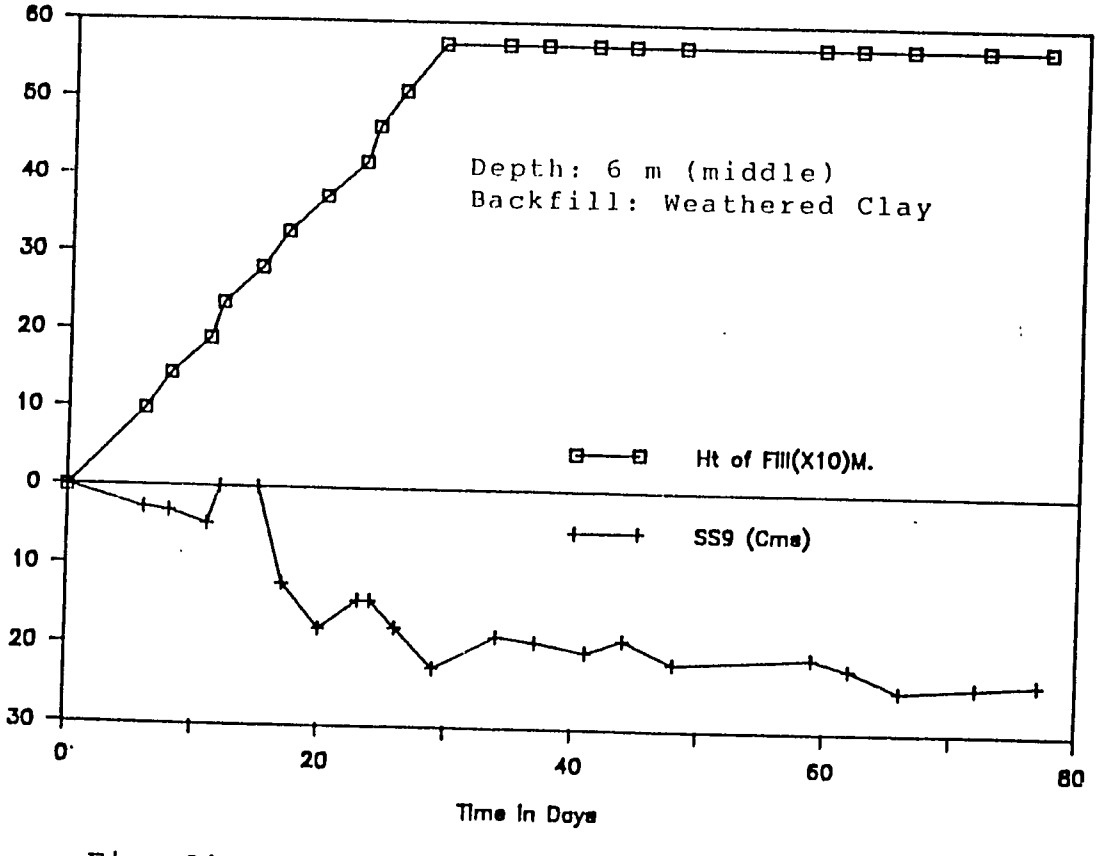

Fig. 91 Observed Subsurface Settlements (SS9)

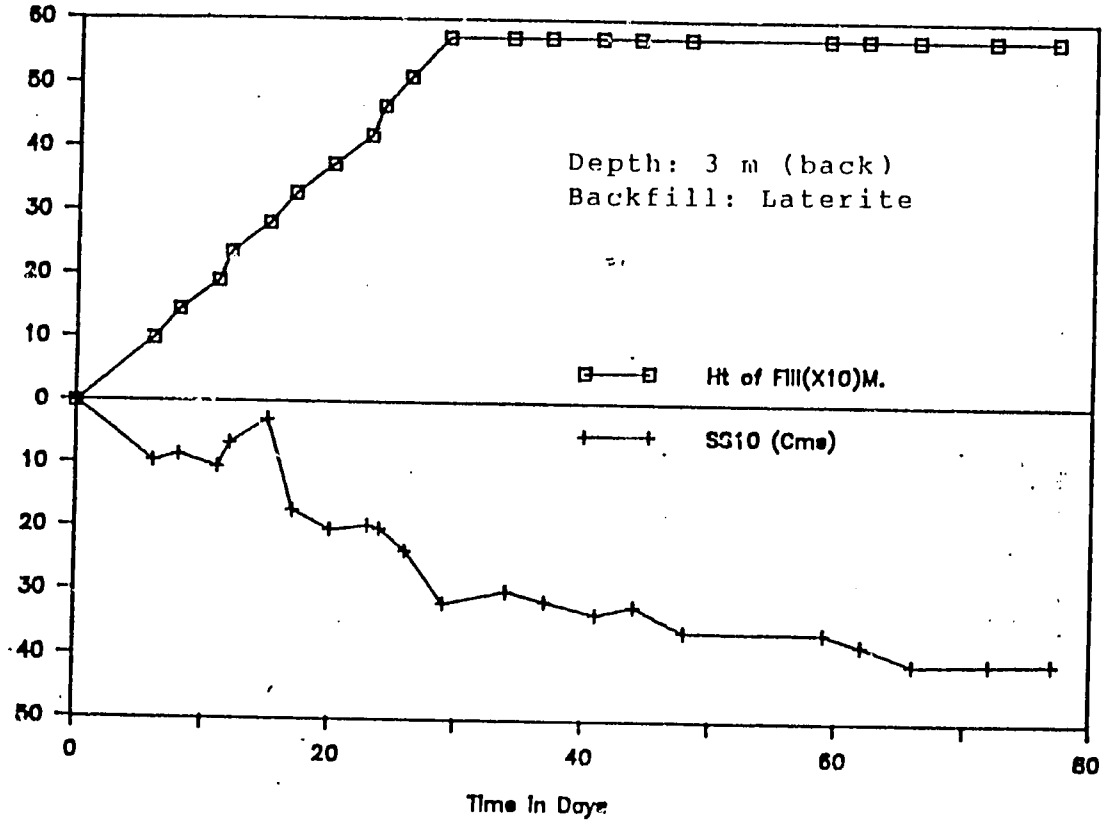

Fig. 92 Observed Subsurface Settlements (SS10)

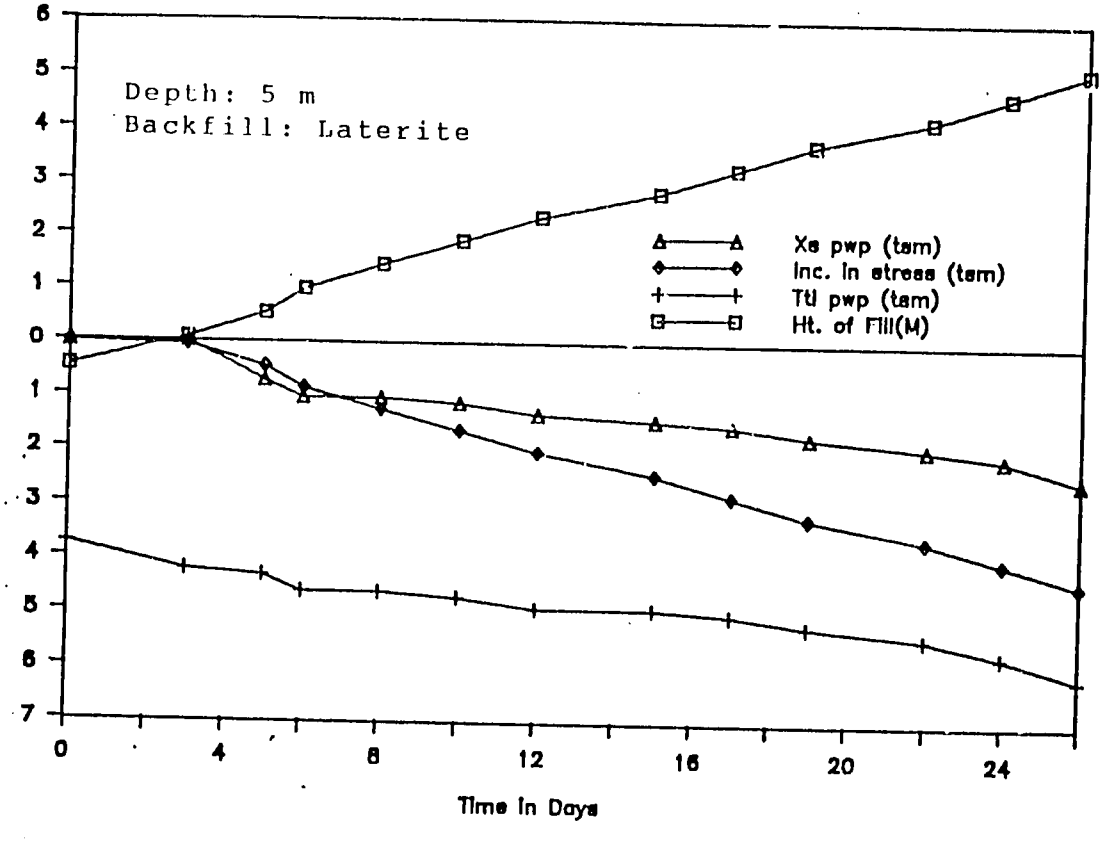

Fig. 93 Measured Excess Porewater Pressure Developed in the Soft Clay Foundation (Pneumatic Piezometer No. 1)

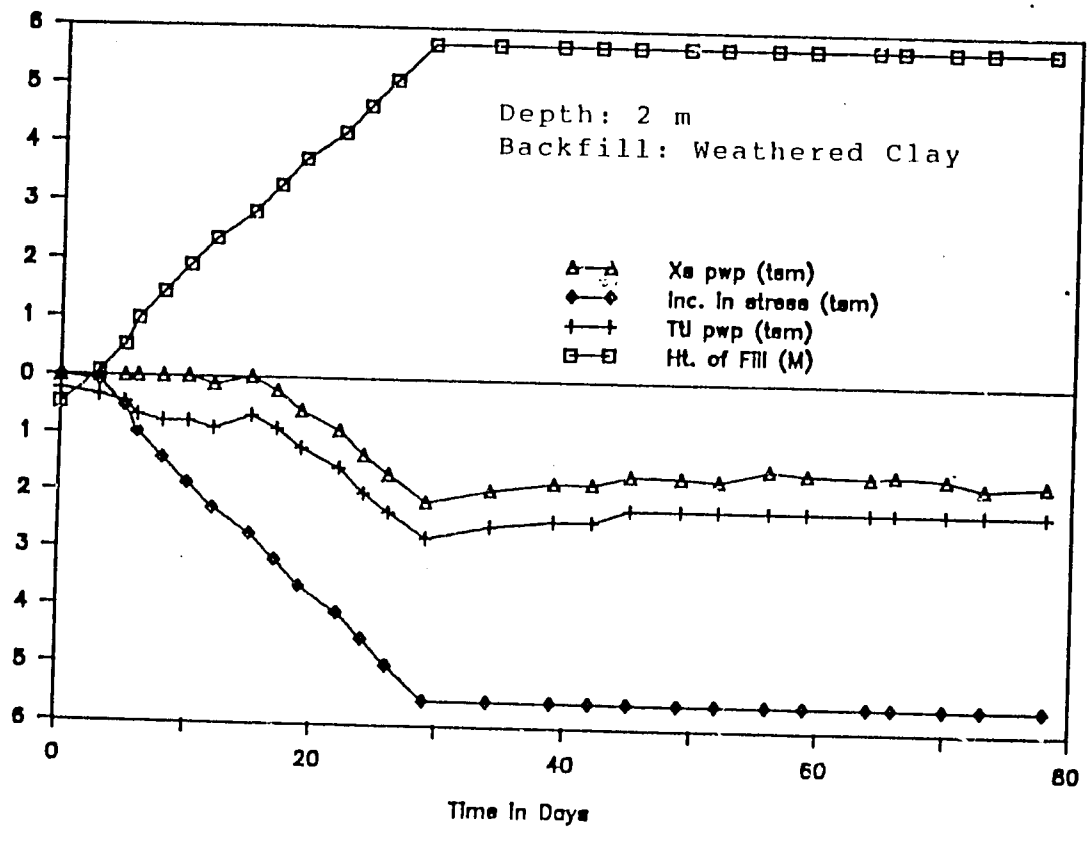

Fig. 94 Measured Excess Porewater Pressure Developed in the Soft Clay Foundation (Pneumatic Piezometer No. 2)

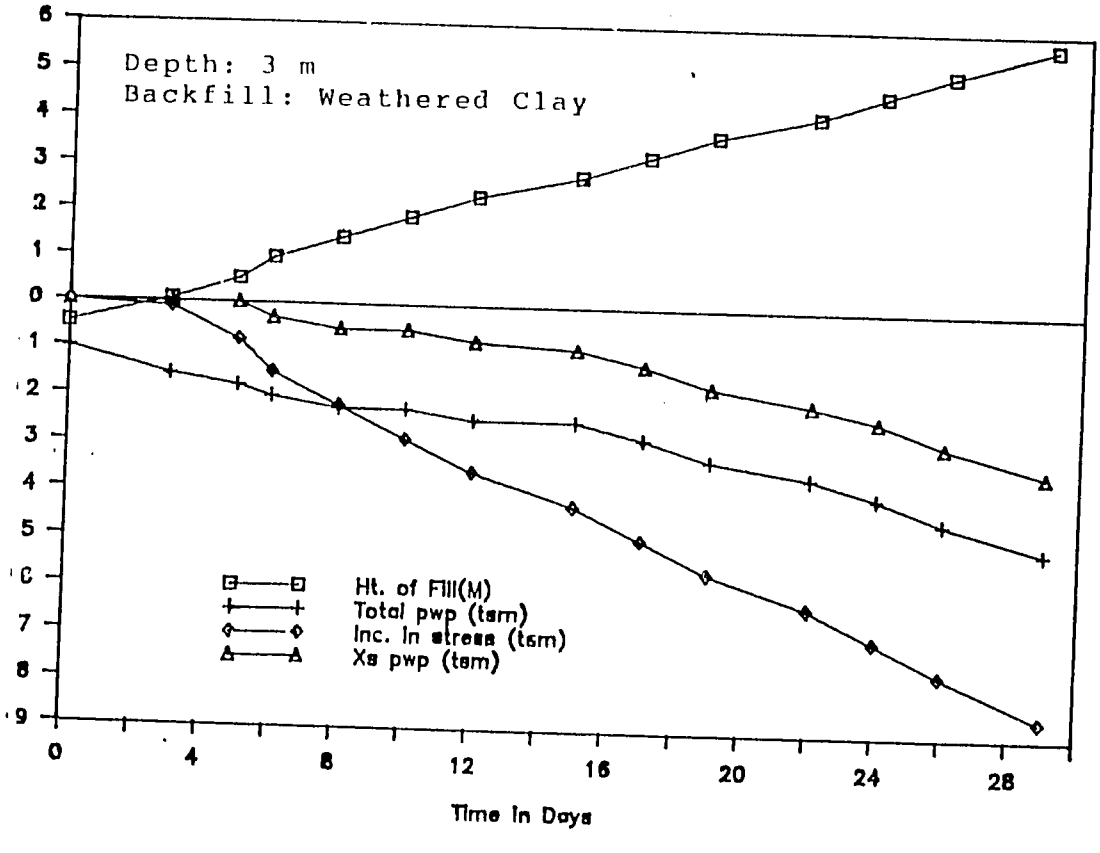

Fig. 95 Measured Excess Porewater Pressure Developed in the Soft Clay Foundation (Pneumatic Piezometer No. 3)

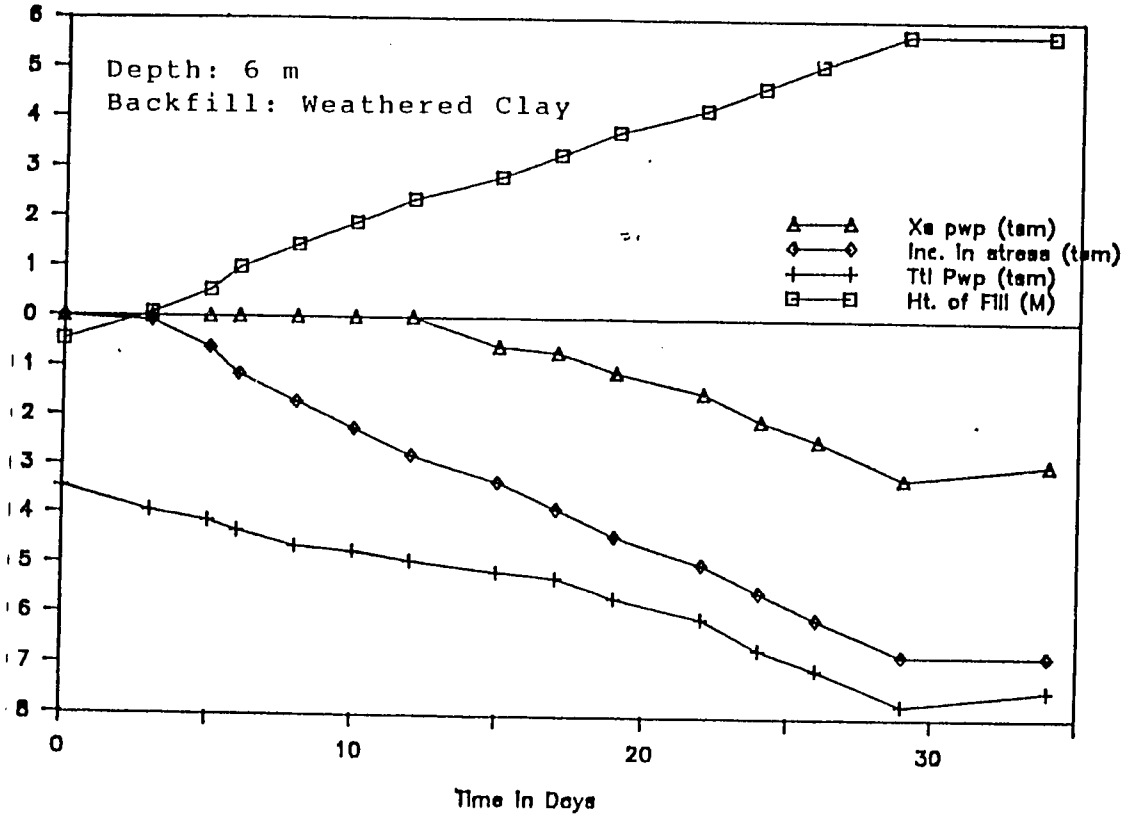

Fig. 96 Measured Excess Porewater Pressure Developed in the Soft Clay Foundation (Pneumatic Piezometer No. 4)

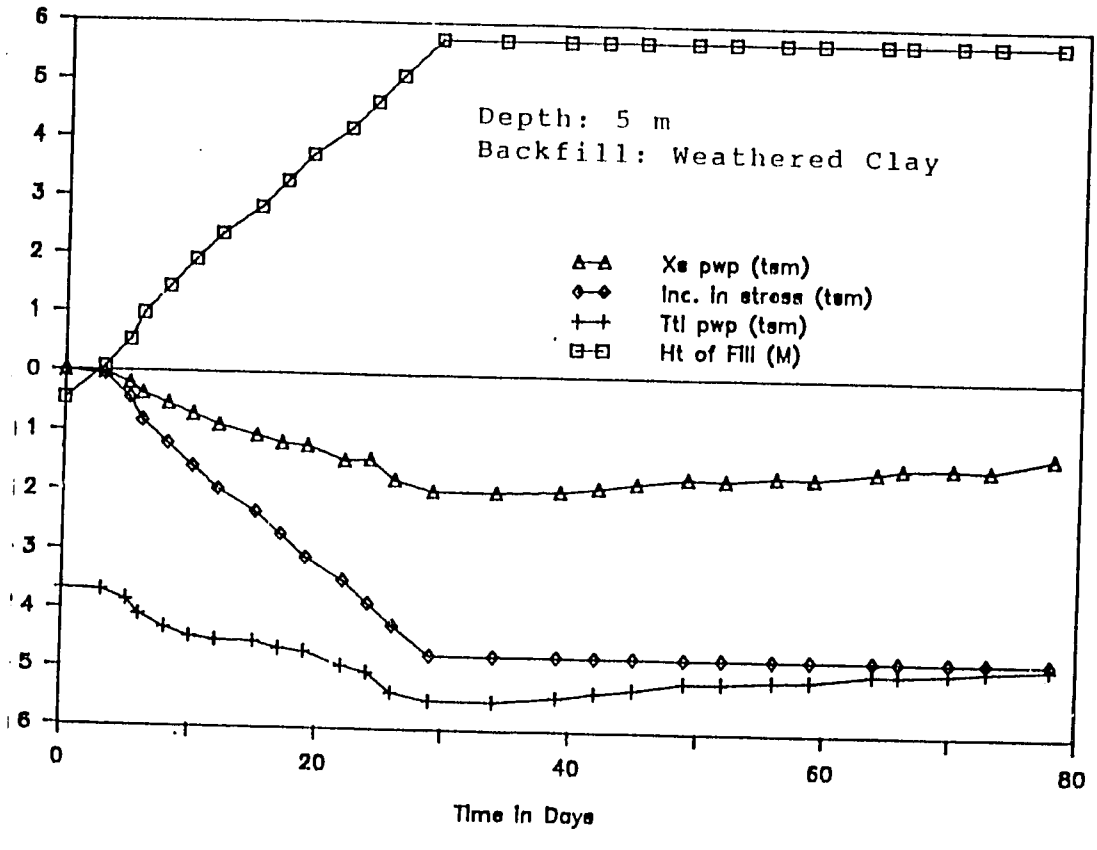

Fig. 97 Measured Excess Porewater Pressure Developed in the Soft Clay Foundation (Hydraulic Piezometer No. 2)

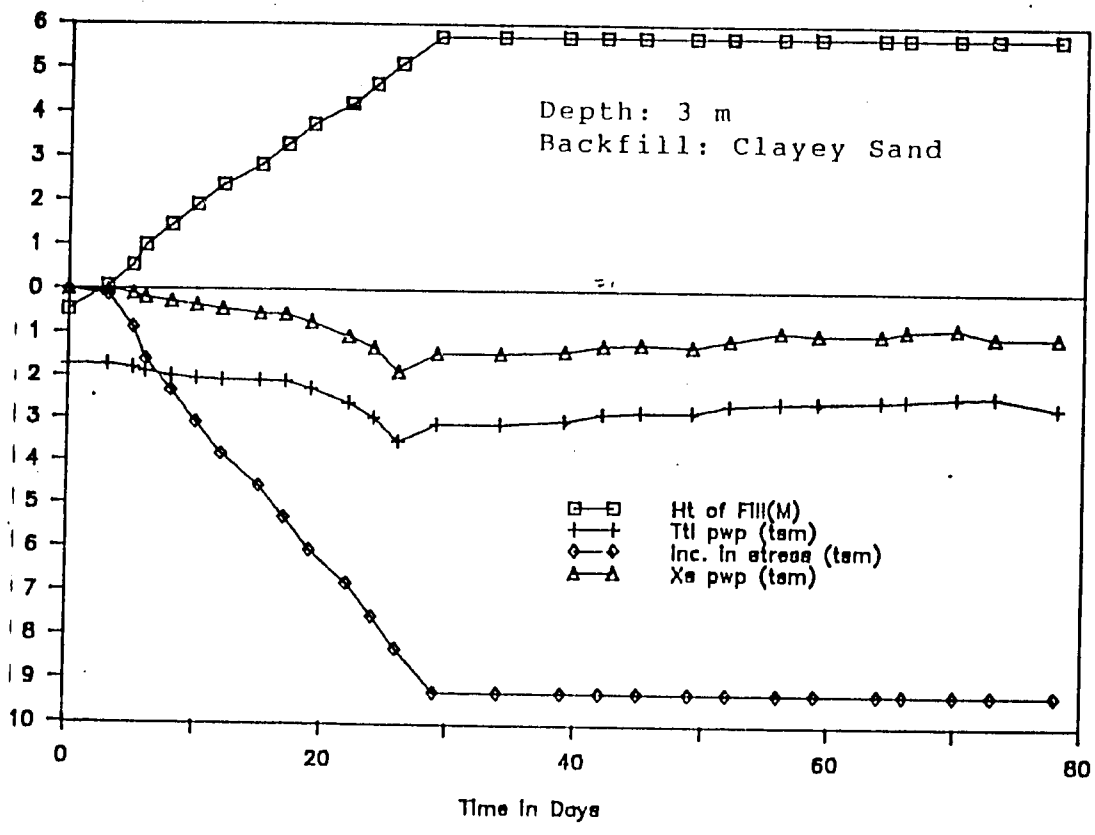

Fig. 98 Measured Excess Porewater Pressure Developed in the Soft Clay Foundation (Hydraulic Piezometer No. 3)

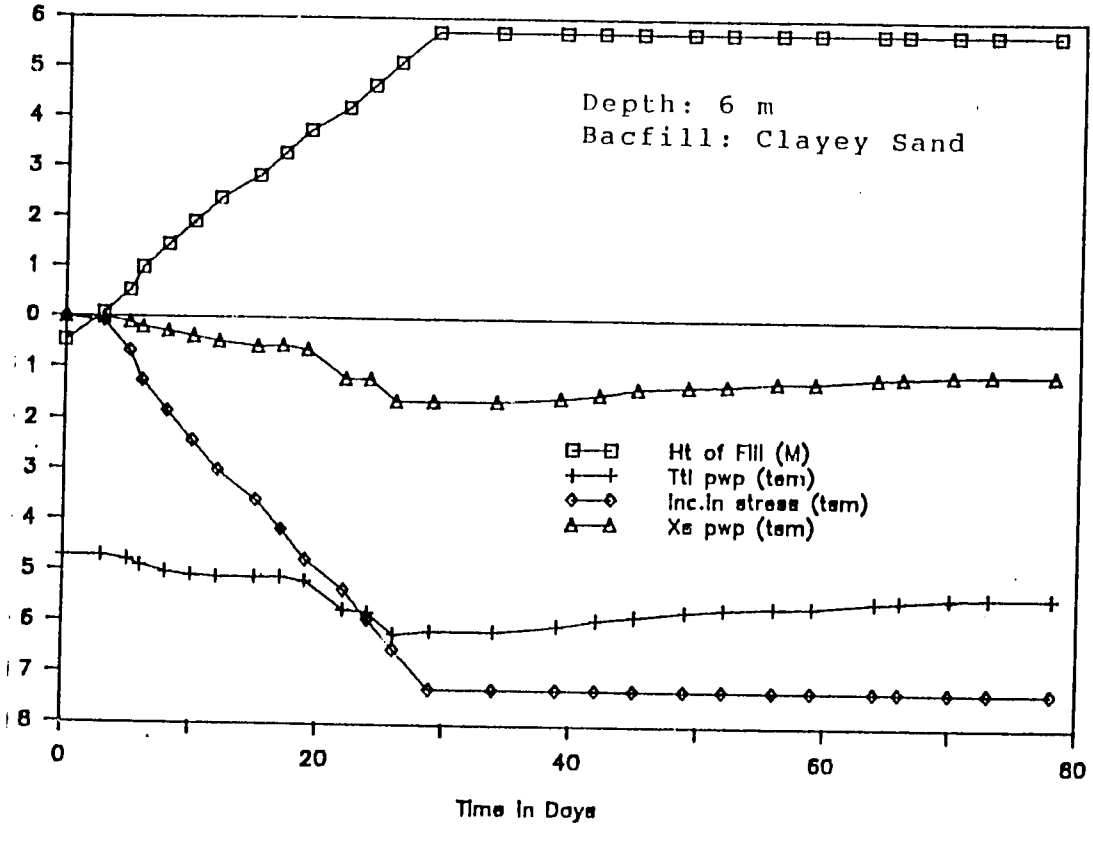

Fig. 99 Measured Excess Porewater Pressure Developed in the Soft Clay Foundation (Hydraulic Piezometer No. 4)

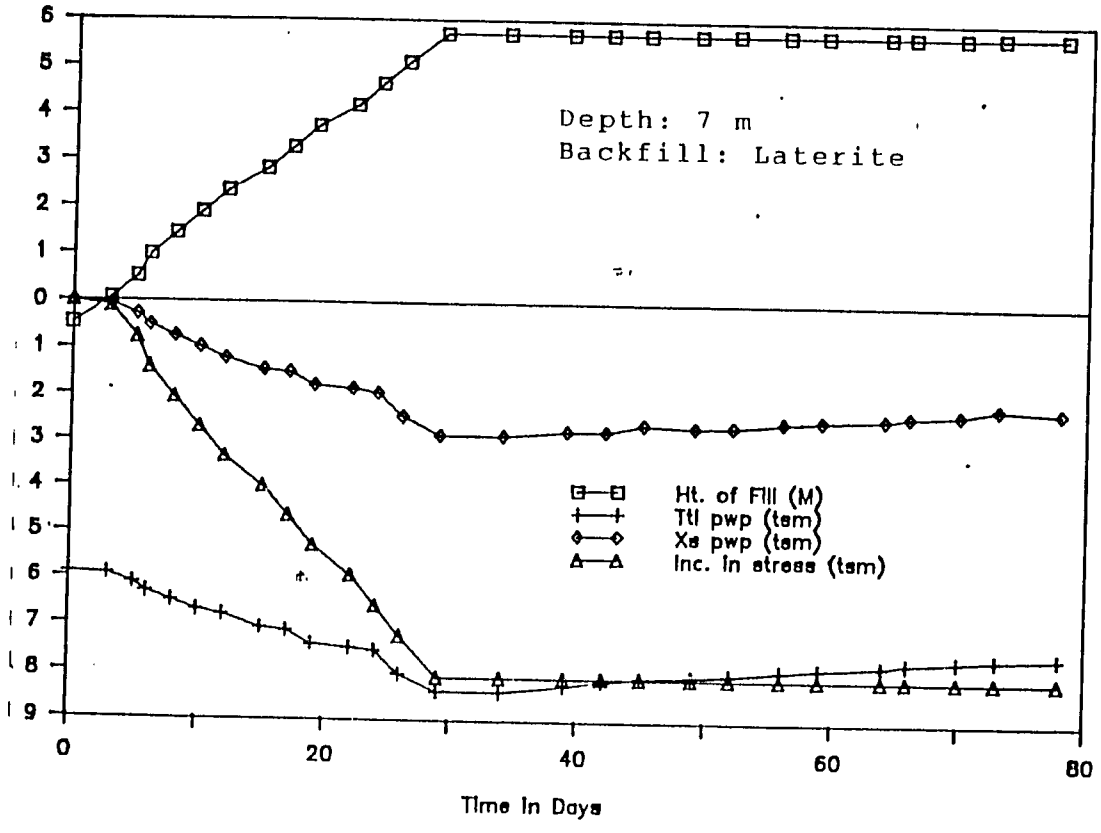

Fig. 100 Measured Excess Porewater Pressure Developed in the Soft Clay Foundation (Hydraulic Piezometer No. 5)

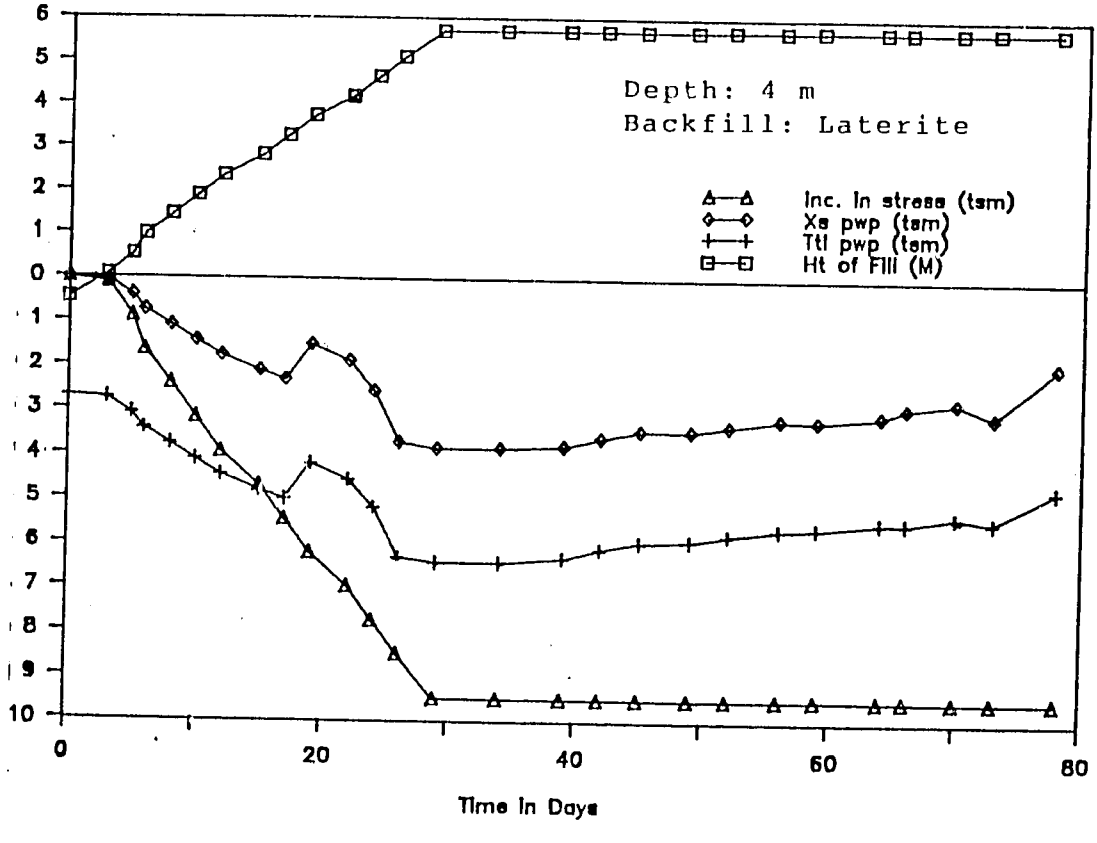

Fig. 101 Measured Excess Porewater Pressure Developed in the Soft Clay Foundation (Hydraulic Piezometer No. 6)

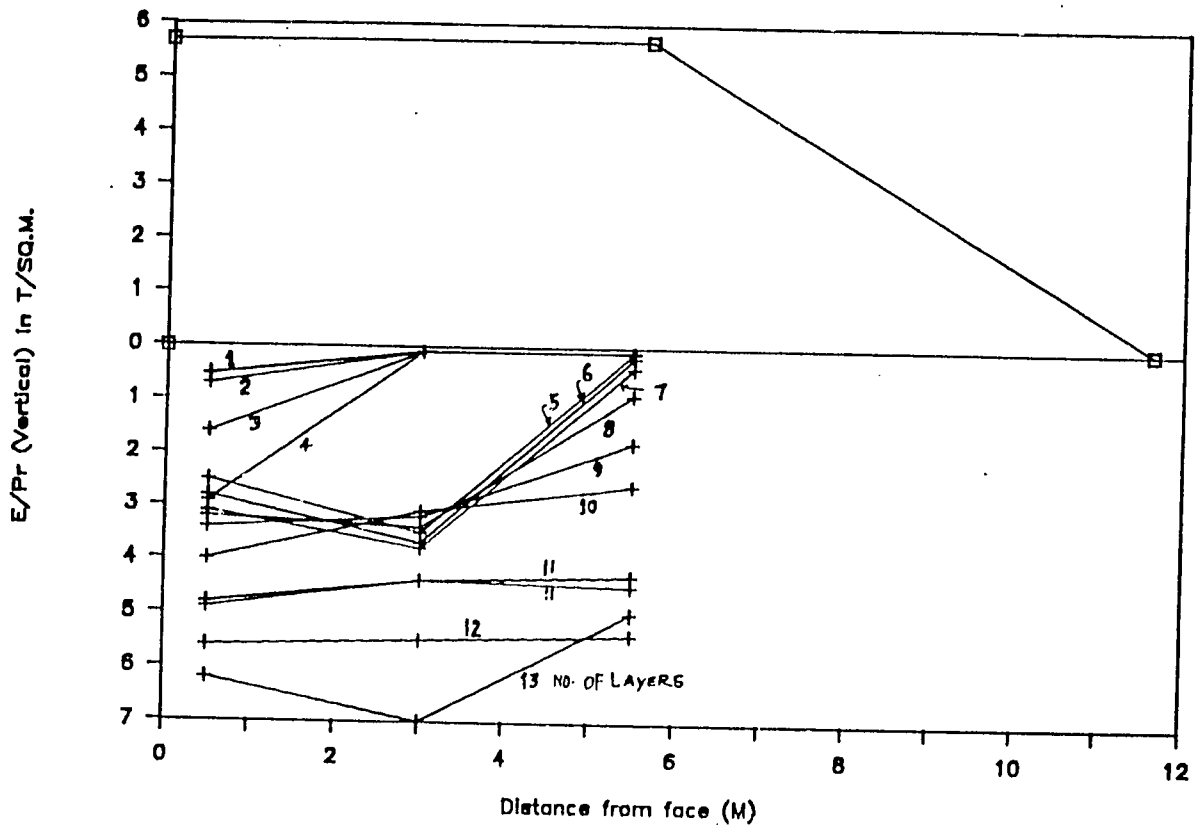

Fig. 102 Observed Pressure at the Base of the Wall During Construction Plotted with Distance from the Face of the Wall

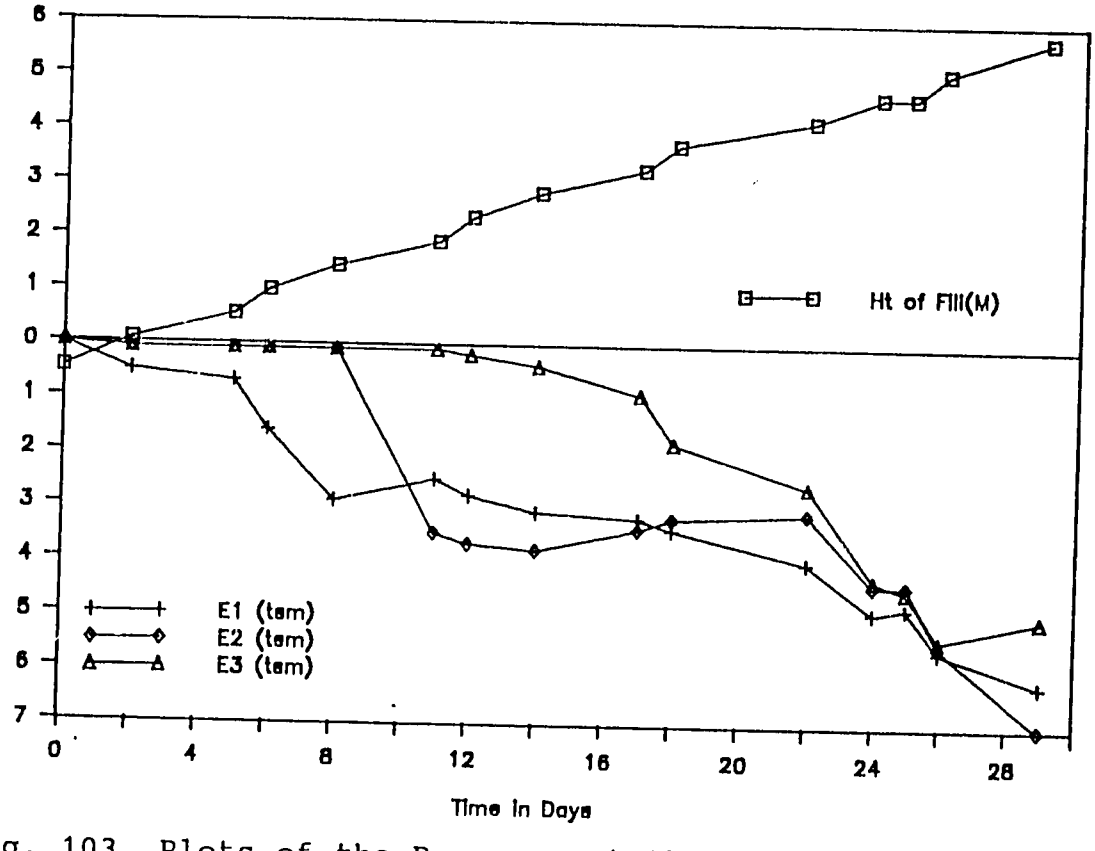

Fig. 103 Plots of the Pressure at the Base of the Wall Against Time